Cooling history of the Biella pluton and implication for Oligocene to Miocene tectonics of the Sesia-Lanzo Zone, Austroalpine, Western Alps

Davide Zanoni[a]*, Luca Corti[a^], Manuel Roda[a]

[a] *Dipartimento di Scienze della Terra 'A. Desio', Università degli Studi di Milano, Milano, Italy*

[^] *Present address: Istituto di Geologia Ambientale e Geoingegneria, Sezione di Milano, Consiglio Nazionale delle Ricerche, Milano, Italy*

*Corresponding author: Dipartimento di Scienze della Terra 'A. Desio', Università degli Studi di Milano, via Mangiagalli, 34, 20133 Milano, Italy.
davide.zanoni@unimi.it

Orcid ID:

Davide Zanoni: 0000-0003-1404-4824

Luca Corti: 0000-0003-0523-6891

Manuel Roda: 0000-0002-5446-6434

Cooling history of the Biella pluton and implication for Oligocene to Miocene tectonics of the Sesia-Lanzo Zone, Austroalpine, Western Alps

We present new emplacement constrains for the Biella pluton within the eclogitic Sesia-Lanzo Zone, western Austroalpine domain. This zone, with the autochthon andesitic cover, is separated from the Southalpine Ivrea Zone by the western Periadriatic Line. Thermobarometry indicates 710 and 750°C, and 0.9 and 2.3 kbar for the final pluton emplacement that accomplished at depths between 3 and 8.5 km. Soon after the emplacement, the pluton was affected by hydrothermal circulations at progressively lower temperature. By 3D modelling, surface and volume distribution of emplacement pressure and temperature are retrieved, and isobaric surfaces are interpolated. The orientation of isobaric surfaces indicates a post-intrusive southeastward rotation of 69±5° about an N 35° trending axis. These results match palaeomagnetic studies on andesites and are consistent with the pluton feeding part of the andesite lava flows. According to the updated pluton emplacement conditions and recent fission track data, we suggest that: (i) the crustal section above the pluton consisted mostly of the andesites; (ii) before 26 Ma the andesites experienced first a depositional and then a tectonic burial during rotation; (iii) between 24 and 19 Ma uplift by back-thrusting with on-going rotation started; (iv) the rotation lasted at least until 16 to 12 Ma.

Keywords: pluton emplacement; pluton 3D modelling; rigid block vertical rotation; crystallization isobaric surfaces; Periadriatic magmatism; late-collisional magmatism

1. Introduction

The Palaeogene plutons of the European Alps represent an important marker in the study of the Alpine collision due to their precise ages (from 43 to 30 Ma) and position along the Periadriatic Line. This line breaks through the whole crust of the Alps and accommodates a dextral transpression (Rosenberg 2004). The Biella pluton, also known as Valle del Cervo pluton, belongs to the Palaeogene igneous bodies emplaced along the westernmost segment of the Periadriatic Line, and is associated with andesite lava flows and dykes. In most cases, structural and tectonic studies are focused on reconstructing the syn-intrusive deformation of the Periadriatic plutons (e.g. Rosenberg

2004; Stipp *et al.* 2004 and refs. therein). Here, we target the emplacement conditions and cooling history of the Biella pluton and subsequent evolution during post-intrusive tectonics.

Constraining the pressure and temperature conditions of emplacement of plutons and their variations throughout intrusive bodies has been proven as an effective way to reconstruct the post-emplacement tilting of magmatic complexes of North America Cordillera (e.g. Ague and Brandon 1992, 1996; Bachl *et al.* 2001; Needy *et al.* 2009). In this contribution we reconstruct the cooling history of the outer portion of the Biella pluton and refine pressure and temperature conditions of pluton emplacement in the internal Sesia-Lanzo Zone. We implement microstructural and mineral chemical analyses on more samples and update thermobarometry with the most recent well-calibrated methods for granitoid rocks, with respect to the data already published (Zanoni *et al.* 2008, 2010; Zanoni 2016). We define the spatial distribution of pressure and temperature estimates for the final emplacement of the outer part of the pluton. The variation in the emplacement pressure is tested with the pressure estimated from mineral assemblages of contact metamorphism in country rocks. To better define the surface and volume variation of emplacement pressures and temperatures, we combine 3D geological models with the inverse distance interpolation method between the pressure and temperature punctual estimates. We also reconstruct isobaric surfaces through potential-field based algorithms within the GeoModeller software (Calcagno *et al.* 2008; Lu and Wong 2008). The results are used to give new insights into the late to post-intrusive tectonics of the Biella pluton and its country rocks, also re-interpreting recent data on the volcaniclastic sequence unconformably overlying the Sesia-Lanzo Zone (Berger *et al.* 2012a, 2012b; Kapferer *et al.* 2011, 2012).

2. Geological Setting

The Periadriatic Line separates the Southalpine domain from the Austroalpine and Penninic domains (Figure 1a) and is considered a pathway for melts that gave rise to the Periadriatic magmatism. Late collisional Periadriatic magmatic rocks mostly are calc-alkaline in composition and form plutons and dykes distributed close and more distant from the Periadriatic Line, respectively (Von Blanckenburg *et al.* 1992, 1998; Pamić and Palinkaš 2000; Rosenberg 2004; Peccerillo and Martinotti 2006; Alagna *et al.* 2010; Lustrino *et al.* 2011 and reference therein). The radiometric ages of the rocks

are comprised between about 43 and 28 Ma, but concentrate in the range of 34 and 28 Ma (Oberli *et al.* 2004; Berger *et al.* 2012a; Bergomi *et al.* 2015; Neubauer *et al.* 2018; Ji *et al.* 2019; Schaltegger *et al.* 2019 and references therein). Only in the easternmost part of the Periadriatic Line, the Pohorje pluton shows Miocene age, but its emplacement is related to the extension of the Pannonic basin (Fodor *et al.* 2008; Trajanova *et al.* 2008).

In the Western Alps, the Periadriatic magmatism is represented by the Biella and Traversella plutons, emplaced in the internal Sesia-Lanzo Zone of the Austroalpine domains, and by the Miagliano pluton, emplaced in the Ivrea-Verbano Zone of the Southalpine domain. Andesitic dykes emplaced on both sides of the Periadriatic line. High-K calc-alkaline and shoshonitic andesite volcanoclasitc deposits uncomfortably overly the Sesia-Lanzo rocks (Carraro and Ferrara 1968; De Capitani *et al.* 1979; Beccaluva *et al.* 1983; Bigioggero *et al.* 1994; Callegari *et al.* 2004; Zanoni *et al.* 2008, 2010; Zanoni 2010; Kapferer *et al.* 2011, 2012; Berger *et al.* 2012a, 2012b; Zanoni 2016).

The Biella pluton displays a concentric zonation consisting of monzonite, syenite, pink porphyric granite, and white granite (Figure 2) and is divided in monzonitic complex and syenitic-granitic complex (Fiorentini Potenza 1959; Pagliani Peyronel 1959; Bigioggero *et al.* 1994). Field observations suggest that the monzonitic complex is older than the syenitic-granitic complex (Bigioggero *et al.* 1994), and this is consistent with zircon U/Pb ages between 30.1 ± 0.20 Ma and 30.9 ± 0.20 Ma, with younger and older ages for the syenitic-granitic and monzonite complexes, respectively (Romer *et al.* 1996; Berger *et al.* 2012a; Ji *et al.* 2019). Rocks of the Biella pluton are shoshonitic in composition with a primary mantle source contaminated by crustal material (Bigioggero *et al.* 1994; Ji *et al.* 2019). Nevertheless, $^{87}Sr/^{86}Sr$ ratio suggests two separate parental magma batches for the monzonitic and syenitic-granitic complexes (Bigioggero *et al.* 1994). Moreover, monzonite is geochemically related to shoshonitic lavas and the two rock types are interpreted as forming a single volcano-plutonic complex (Callegari *et al.* 2004).

The country rocks consist of metapelites and various types of metagranitoids and minor metabasite belonging to the Eclogitic Micaschists Complex of the Sesia-Lanzo Zone (Figure 1b, Zanoni *et al.* 2008; Zanoni 2016). Except for minor parts of this

complex, which preserve a dominant fabric marked by blueschist-facies mineral assemblages (Regis *et al.* 2014; Giuntoli and Engi 2016; Corti *et al.* 2017, 2018), most of the country rocks retain a regional foliation marked by eclogite-facies mineral assemblages (Compagnoni *et al.* 1977; Spalla *et al.* 1996; Gosso *et al.* 2010; Delleani *et al.* 2013; Roda *et al.* 2018, 2020; Zucali *et al.* 2020 and references therein). The Alpine subduction-related metamorphic peak was accomplished at 13-20 kbar and 500–600 °C (Compagnoni *et al.* 1977; Lardeaux and Spalla 1991; Pognante *et al.* 1987; Zucali *et al.* 2002; Roda *et al.* 2012) and is dated between 85 and 65 Ma (Cenki-Tok *et al.* 2011; Rubatto *et al.* 2011; Regis *et al.* 2014 and references therein). The subsequent exhumation-related greenschist-facies metamorphism occurred at 45–37 Ma (Babist *et al.* 2006; Inger *et al.* 1996; Cortiana *et al.* 1998; Lardeaux 2014).

The Biella pluton postdates the regional greenschist-facies metamorphism and records a magmatic foliation. The intrusion produced a contact metamorphic aureole that affects the eclogite and greenschist facies mineral assemblages. Brittle structures and hydrothermal veins and fractures intersect the pluton and country rocks (Bernardelli *et al.* 2000; Rossetti *et al.* 2007; Zanoni *et al.* 2008, 2010; Zanoni 2016). The pluton emplaced at shallow crustal levels when the hosting Sesia-Lanzo Zone rocks were already exposed to erosion (Zanoni *et al.* 2010). Palaeomagnetic data on andesite lava flows and dykes indicate post-intrusive rotation of the inner part of the Sesia-Lanzo Zone toward the Periadriatic Line (Lanza 1977, 1978; Schmid *et al.* 1989). Recently this interpretation has been updated on the basis of zircon and apatite fission tracks that suggest this rotation predates the intrusion of the Biella pluton and accomplished in couple of million years (Berger *et al.* 2012b).

3. Structural relationships of igneous and country rocks

Structural mapping and analysis along the western and eastern margins are shown in two maps that encompass part of the monzonitic complex and the country rocks variably affected by contact metamorphism (Zanoni *et al.* 2008; Zanoni 2016). Since structures are extensively explained in the previous works, in this section we only briefly summarize the structural data and discuss in details the data relevant for this work. The country rocks record multiple tectono-metamorphic stages and the intrusive contacts intersect all ductile structures of the country rocks, although locally the regional foliation is sub-parallel to the pluton margin (Figure 3 and Zanoni *et al.* 2010).

Brittle structures such as faults (Figure 4a), fractures, and hydrothermal veins mostly developed from late to post-intrusion stages and some of them intersect plutonic and country rocks and locally are associated with metre-thick cataclastic bands (Figure 4b and Bernardelli *et al.* 2000; Rossetti *et al.* 2007; Zanoni *et al.* 2008; Zanoni 2016). The orientation of the magmatic foliation varies in the different sectors of the pluton, as the orientation of the magnetic fabric (Hrouda and Lanza 1989). The northwestern sector retains a generally northwestward steeply dipping magmatic foliation (Figure 3). This orientation dominates in Valle della Pragnetta, just west of Rosazza (Figures 2, 3). To the north and northwest of M. Tovo (Figure 2), three orientation groups of magmatic foliation are steeply dipping toward north-northeast, north-northwest, and west-northwest. However, in this area magmatic foliation is also shallow dipping. In the southwestern sector, magmatic foliation is generally steep and to the north and west of M. Becco mainly strikes NW-SE, whereas to the north and northwest of Oropa is steeply dipping toward north-northwest and moderately dipping toward northeast (Figures 2, 3). In the southeastern sector, the magmatic foliation shows different orientation from steeply to moderately dipping (Figure 3). In the northeastern sector, magmatic foliation is mainly moderately dipping westward with scattered orientations and shallow dipping to the northwest and to the north of Cima delle Guardie, respectively (Figure 2). The orientation of the contact surface of pluton and country rocks is steeply dipping north-northwestward and westward in the northwestern sector, and moderately to shallow dipping westward to northeastward in the southwestern sector of the pluton (Figure 3). Country rock xenoliths, usually up to decimetres in size, are particularly diffused in the areas between Oropa and Riabella (Figure 4c), and between Monticchio and Val Sessera. At hundred metres to the east of Riabella, even up to 10 metre-sized xenoliths occur.

4. Contact metamorphic effect

The country rocks of Biella pluton mainly consist of metapelites with metagranitoids and minor metabasites. With the exception of metagranitoids in the northwestern margin of the pluton, which preserves a pervasive fabric marked by high temperature and low pressure mineral assemblages (Zanoni 2016), the rest of country rocks preserve a dominant eclogitic fabric typical of the Eclogitic Micaschists Complex (e.g. Compagnoni *et al.* 1977; Zucali *et al.* 2002). The contact metamorphism is responsible for fine-grained coronitic mineral assemblages that grew extensively at the

expenses of the eclogitic mineral assemblages of country rocks and scarcely in the high temperature metagranitoids. The amount of contact metamorphic minerals decreases with the distance from the pluton. The types of contact mineral assemblages and metamorphic reactions in different country rock types and their variation within the aureole are already described (Zanoni *et al.* 2008, 2010; Zanoni 2016). Very close to the pluton margin, contact metamorphism produced mineral assemblages suitable for barometrical estimates, which consist of garnet, biotite, plagioclase, cordierite, spinel, orthopyroxene, K-feldspar, and quartz. Barometry in the thermal aureole is here used to validate the barometrical estimates on magmatic rocks for pluton emplacement.

5. Microstructure of monzonite

In this section, microstructural and textural relationships of mineral grains, along with petrography, are described to interpret the crystallization sequence from the magma and post-magmatic mineral growth (Table 1). The studied rocks are from the monzonitic complex and consist of monzonite and mafic monzonite, which forms enclaves. Mafic monzonite plots in the field of monzonite, syenite and granite and this is due to local enrichment of K-feldspar or quartz (Figure 5).

Coarse-grained monzonite contains K-feldspar (Kfs), plagioclase (Pl), amphibole (Amp), biotite (Bt), clinopyroxene (Cpx), quartz (Qz), magnetite (Mag), titanite (Ttn), apatite (Ap), and zircon (Zrn). Monzonite retains a magmatic foliation that is mainly marked by shape-preferred orientation of millimetre-sized euhedral Kfs and Pl crystals (Figure 6a). Kfs encloses Pl crystals with same (Pl_1) or different orientation ($Pl_{pre\text{-}1}$). $Pl_{pre\text{-}1}$ shows irregular and smoothed boundaries rimmed by Na-richer Pl_{1a} (Figure 6b). Pl_1 crystals locally show concentric growth zoning and consists of inner Pl_{1a} and rims of Pl_{1b}. Rarely Pl_{1a} shows fractured filled by mono-crystals of Pl_{1b} that grew in continuity with Pl_{1a}, as testified by twinning intersecting both Pl types. Pl_1 shows same orientation of Kfs crystals and sharp contact boundaries with Kfs. Kfs shows Carlsbad twinning and locally is rimmed by myrmekite intergrowths of quartz and Pl_{2a} and contains patchy or flame perthites (Pl_{2b}) (Figure 6c). Finally rare Pl_{2c} forms rim of Pl_1 or fills very local micro-veins and interstitial spaces. Euhedral to subhedral Amp_{1a} coarse-grained crystals show shape preferred orientation parallel to the magmatic foliation, with sharp grain boundaries against Pl_{1b} and Kfs (Amp_{1b}) (Figure 6d). Cpx mostly forms euhedral crystals often overgrown by Amp_{1a} at its rims or along cleavages

(Figure 6e) and locally Amp_{1a} pseudomorphs Cpx. Amp_{1a} forms also poikilitic crystals enclosing euhedral Ttn_{1a}, Ap, and Mag. Amp_{1b} mono-crystals are interstitial, mostly between Kfs and Pl_{1b} (Figure 6d), but locally also with respect to Bt and more rarely to rounded Qz crystals (Figure 6f). Bt forms coarse-grained euhedral (Figure 6f) to anhedral crystals that often enclose abundant euhedral Ap and minor Zrn and rarely shows gentle undulose extinction and kink-bands. Ttn_{1b} and Qz form interstitial mono-crystals also. Qz also fills late-magmatic fractures in Kfs and shows gentle undoluse extinction. Sample R1 is a finer-grained monzonite richer in biotite and plagioclase, and poorer in amphibole with respect to the other samples. In this monzonite type the magmatic foliation is very local and millimetre-sized aggregates of clinopyroxene, biotite, and magnetite occur. This monzonite type outcrops at Riabella over a surface of 1.1 x 10^4 m^2 and its volume is possibly around 4 x 10^5 m^3.

Mafic mozonite consists of Kfs, Pl, Bt, Amp, Cpx, Qz, Ap, Ttn, and Mag and constitutes up to metre-sized enclaves in monzonite (Zanoni 2016). The magmatic foliation is marked by shape preferred orientation of euhedral Bt (Figure 6g), locally associated with imbricated Pl_1 and Cpx. Ap and Mag form euhedral and minor subhedral crystals enclosed in Bt, Kfs, and Pl. Amp_{1a} replaces Cpx at the rim and cleavages. Amp_{1b} is subhedral to anhedral and is interstitial with respect to most of the other mineral phases. Kfs_{1b} forms up to millimetre-sized poikilitic crystals with rare faint flame perthites and gentle undulose extinction and enclose all the mineral phases with sharp grain boundaries, and which locally show shape preferred orientation. Kfs_{1b} contains also $Pl_{pre\text{-}1}$ in crystals with growth zoning and irregular grain boundaries rimmed by Pl_1 (Figure 6h), which grew by reaction with residual melt before the growth of Kfs. On the other hand, Kfs_{1a} forms rare graphic structure at the core of Pl_1. Ttn_{1a} forms rare euhedral to subhedral crystals, whereas Ttn_{1b} is interstitial.

Post-magmatic mineral growth is very localized but affects all monzonite types. Besides Pl_2, post-magmatic Amp_2 grew at the rims or in scattered patches nucleating from Amp_1 cleavages or fractures (Figure 7a). Allotriomorph Ttn_{2a} forms intergranular films and because of this feature is interpreted as hydrothermal (e.g. Erdmann *et al.* 2019). Chlorite, epidote, and locally Ttn_{2b} grew at the expenses of Bt, and fine-grained epidote and white mica partly replaced Pl (Figure 7b). Chlorite replaced also Amp_1 and locally grew in association with epidote at the expenses of plagioclase. Finally, chlorite also fills interstitial spaces.

6. Mineral chemistry of igneous rocks

6.1. Methodological approach

Mineral chemical WDS and EDS analyses were obtained with a JEOL JXA-8200 microprobe and a Cambridge Instruments Stereoscan 360 scansion electron microscope, respectively and both operating at Dipartimento di Scienze della Terra "A. Desio" of Milano University. Electron microprobe worked with a beam current of 5 nA, potential difference of 15 kV, and working distance of 11 mm. Scansion electron microscope worked with a bean current of 190 pA, potential difference of 20 kV, and working distance of 25 mm. Natural silicates, metals, oxides, and chlorides were used as calibration standards and a ZAF procedure was the matrix correction. Stoichiometric formulae were calculated on the basis of the following oxygen atoms: 4 for magnetite, 5 for titanite, 6 for clinopyroxene, 8 for feldspar, 12.5 for epidote, 14 for chlorite, 22 for biotite, and 23 for amphibole. Fe^{3+} was estimated for magnetite (Ferracutti *et al.* 2015), clinopyroxene (Morimoto 1988), epidote (Yavuz and Yıldırım 2018), and amphibole (Locock 2014). Chemical variations of main mineral phases are represented in diagrams (Figures 8, 9, and 10) and in two supplementary files, which both consists of multiple sheets and report average and standard deviation (1σ) of selected compositional parameters (Supplemental File 1) and complete stoichiometric formula of selected mineral analyses (Supplemental File 2). We acquired more than 840 mineral composition analyses. In diagrams, analyses are separated by sample (different colours) and by growth generation (different symbols) to show mineral chemistry variations over space and growth timing. Colours for discriminating the samples were chosen to facilitate colour-blind people (Levine 2009).

6.2. Results

The magmatic amphibole (Amp_{1a} and Amp_{1b}) of the Biella pluton consists of Mg-hornblende and minor actinolite and very scarce edenite, whereas the post-magmatic amphibole (Amp_2) is actinolite. Only an amphibole grain enclosed in Cpx is pargasite in mafic monzonite (sample BPA4; not in the diagram) and it is interpreted as $Amp_{pre\text{-}1}$. The composition of Amp_{1a} and Amp_{1b} is overlapped in each sample (Figure 8a) but generally average compositions (Supplemental File 1) highlight an Al and Ti decrement of 0.01 to 0.28 apfu and up to 0.07 apfu, respectively. Conversely Ca shows an increment from Amp_{1a} to Amp_{2b} up to 0.04 apfu in many samples. Amp_{1a} and Amp_{1b}

show a similar X_{Mg} that seems to be controlled by local variation in bulk composition, as it is evident for sample 59A (Figure 8a). However, Amp_{1a} at clinopyroxene reaction rim shows in some samples higher X_{Mg} and Ca, possibly due pyroxene composition. The most marked variation in each sample concerns the composition of Amp_2 compared with that of Amp_1. Amp_2 shows minor amount of Al and Ti and generally higher Ca and X_{Mg}. Amphibole also shows compositional variation throughout the pluton (Figure 8a; Supplemental File 1). In rocks from the northwestern part of the pluton, Amp_{1a} and Amp_{1b} show markedly higher amount in Al then rocks from the southwestern and southeastern part. Ti shows a similar trend but with less marked differences. Only Amp_{1a} and Amp_{1b} in sample R1 deviate from this trend and show higher Al and Ti compared to the nearby samples.

Plagioclase of the Biella pluton mainly consists of andesine, oligoclase, and albite (Figure 8b). Only in mafic monzonite (sample BPA4) Pl_{pre-1} shows a composition across bytownite and labradorite. The general trend of chemical variation of magmatic plagioclase shows an increase of albite molecule from Pl_{pre-1} to Pl_{1b}. From Pl_{pre-1} to Pl_{1a} albite increases from 5 to 34%, with the most marked increment in mafic monzonite (BPA4). Only in sample 3031105, from the northwestern part of the pluton, Pl_{pre-1} shows higher content in albite than Pl_{1a} (Supplemental File 1). Albite variation from Pl_{1a} to Pl_{1b} is comprised between 1 to 12%. The exception to this trend is represented by Pl_{1a} developed as reaction rim on Pl_{pre-1} that shows a variable composition across albite and oligoclase. Pl_{2a} myrmekite consists of a Ca-rich oligoclase, whereas Pl_{2b} perthitic exsolution is mostly albite. Pl_{2c} shows a general albite composition but in some veins has a Na-rich oligocalse composition (Figure 8b; Supplemental File 1).

Kfs_{1a} in mafic monzonite shows 7% less of orthoclase (K/(K+Na+Ca)) component with respect to Kfs_{1b} (Figure 8b; Supplemental File 1). Generally, in monzonite, the highest orthoclase content in Kfs is in rocks with more developed exsolutions.

Pyroxene in Biella pluton is a diopside and rarely augite (Figure 9) with X_{Mg} decreasing from core to rim. The lowest X_{Mg} is in a sample from the northeastern margin of the pluton (59A) and in mafic monzonite (BPA4). In the other samples this ratio is quite similar and in average does not exceed 0.86. Pyroxene from shoshonite

lavas mostly plots in the augite field, but very close to the diopside field where pyroxene from Biella monzonite plots (Figure 9).

Biotite in the Biella pluton shows X_{Mg} comprised between 0.40 and 0.60, with the lowest values in sample 59A. Ti is generally comprised between 0.35 and 0.50 apfu, but locally crystals contain less than 0.30 apfu of Ti. The biotite crystals with Ti minor than 0.30 apfu does not show variation in X_{Mg}, suggesting that low-Ti biotite recorded hydrothermal alteration (e.g. Nachit *et al.* 2005).

Magnetite is almost pure $FeFe_2O_4$ with less than 0.7±0.3% of the solid solution that consists of $FeAl_2O4$, $MgFe_2O_4$, $FeFe_2O_4$, $MnFe_2O_4$, $ZnFe_2O_4$, $FeCr_2O4$, Fe_2TiO_4; among those, the most frequent and abundant end-members are chromite and hercynite.

Titanite plots in the magmatic field (Figure 10a), with the exception of Ttn_{2b} that shows much higher Al content. Within the magmatic field, Ttn_{2a} shows generally the higher amount of Al. Ttn_{1a} and Ttn_{1b} show little difference in Al and higher difference in Fe, but Al is slightly higher in Ttn_{1a} (Figure 10a and Supplemental Files 1, 2).

Generally, epidote in the Biella pluton grew during post-magmatic evolution. Only in the sample from the northeastern margin of the pluton (59A) rare magmatic allanite occurs. Epidote replacing plagioclase shows lower Fe amount than epidote overgrowing biotite. In place this epidote is pure clinozoisite (BPA4), which in turn is overgrown by Fe-rich epidote (Supplemental Files 1, 2).

Chlorite shows Al^{IV} comprised between 0.54±0.01 and 1.16±0.10 apfu, and X_{Mg} between 0.48±0.01 and 0.60±0.05 (Supplemental Files 1, 2). The highest X_{Mg} values are from chlorite replacing biotite, whereas the lowest values are from interstitial chlorite.

7. Temperature and pressure estimates

7.1 Methodological approach for igneous rocks

For igneous rocks the PT estimates were mainly focused on amphibole barometry and thermometry to get the conditions for the final magmatic emplacement. Amphibole barometry was estimated by the application of the most recent calibrations (Schmidt 1992; Anderson and Smith 1995; Molina *et al.* 2015; Mutch *et al.* 2016). The analyzed samples contain the proper buffer mineral assemblages recommended for

these barometers that were applied considering the compositional limits of amphibole and plagioclase facing amphibole. The temperature was estimated applying the calibration of Holland and Blundy (1994) and Putirka (2016). Since Holland and Blundy (1994) calibration is sensitive to pressure and Anderson and Smith (1995) calibration is sensitive to temperature, the results of these two calibrations were iterated until convergence (Anderson *et al.* 2008). Molina *et al.* (2015) barometer was applicable only in samples 3130105 and BPA4 because in the other samples Al content in amphibole is not sufficient for this barometer. As a consequence, estimates obtained with this barometer were not considered for averaging pressures. Putirka (2016) finalized two thermometers, independent and dependent on pressure. The pressure-dependent thermometer was applied with pressure estimated by the method of Mutch *et al.* (2016) as input parameter. Our results point out that the pressure-depended temperature estimates are up to 10°C higher than values retrieved by the pressure-independent thermometer. Since pressure independently estimated is available, we chose results from the pressure-dependent thermometer, which has a calibration error slightly lower than that of pressure-independent thermometer (Putirka 2016). Crystallization pressure was also tested by means of Al_2O_3 content in magmatic titanite (Erdmann *et al.* 2019). We applied the two-feldspar thermometry based on the ternary mixing of feldspar (Benisek *et al.* 2004), implemented with new feldspar-mixing models (Benisek *et al.* 2010), by means of the iterative calculation for minimizing the variance of the three end-member temperature (Kroll *et al.* 1993). Finally, we estimated the last increment of sub-solidus cooling by using a recent thermometer based on chlorite composition, which does not require knowing Fe^{3+} content (Bourdelle *et al.* 2013). We considered only a few temperature estimates from interstitial chlorite and chlorite replacing plagioclase. Indeed, with respect to the chlorite that replaced biotite, the composition of this chlorite should not be influenced by the local composition of the replaced mineral.

7.2. Results from igneous rocks

The methods for amphibole thermobarometry were applied separately for Amp_{1a}, Amp_{1b}, and Amp_2. According to microstructural analysis, amphibole is among last magmatic phases to crystallize from the magma, and in particular Amp_{1b}, which is the crystal rims and the interstitial crystals, represent the very last increment of amphibole crystallization. Thus, in general, conditions estimated from Amp_{1b} are the

more representative for the very final pluton emplacement conditions. Generally, in any samples temperature and pressure estimated values decrease from Amp_{1a}, to Amp_{1b}, to Amp_2, for each thermobarometrical method applied (Supplemental File 3). The largest difference is between Amp_{1a} and Amp_{1b} vs. Amp_2, whereas between Amp_{1a} and Amp_{1b} the differences in some samples are not marked at all. The values of pressures in different samples show a decreasing trend from NW to SE (Figure 11b). These variations in general are not prominent but are quite regular, along both pluton margins. Considering the weighted averages of all estimates for Amp_{1a} and Amp_{1b} in each sample, the most marked variations are recorded along the western margin where the highest temperature and pressure values are estimated west of Rosazza village at 756±22 °C and 2.34±0.42 kbar, whereas the lowest are recorded at Riabella at 723±32 °C and 0.87±0.15 kbar (Figure 11b). Along the eastern margin of the pluton the variation are not very marked and the northernmost sample, ENE of Cima delle Guardie, record slightly lower values, of 724±32 °C and 1.41±0.43 kbar, than the two samples collected along the ridge connecting Cima del Bonom and Monticchio (757±33 °C - 1.46±0.54 kbar; 739±41 °C - 1.43±0.55 kbar). Along this ridge the more marked drop in pressure and temperature is indicated by the PT conditions estimated more than 1 km east of Monticchio at 709±18 °C and 0.93±031 kbar. Thus, west of Rosazza and at Riabella the highest and lowest pressures and temperatures for the final pluton emplacement are recorded. Only the sample from ENE of Cima delle Guardie deviates from the general decreasing trend of values but the differences with respect to the samples from the ridge between Cima del Bonom and Monticchio are negligible. Besides that, there is another anomaly with respect the variation trends; in a sample at Riabella (R1), crystallization conditions are constrained at 753±33 °C and 1.68±0.65 kbar (Figure 11b). Pressures based on Al_2O_3 in titanite are consistent with the variation trend disclosed by amphibole barometry (Supplemental File 3). Since authors state that this method still needs to be better tested, we consider the results only in terms of relative pressure variation. Feldspar thermometry indicates temperatures between 659±11 and 745±33 °C for crystallization from the magma. In some samples, these temperatures are lower than those estimated by amphibole thermometry and this result may be due to incipient unmixing affecting K-feldspar after the magmatic crystallization. In sample with K-feldspar-free perthite temperatures better match those estimated by amphibole thermometry (Supplemental File 3).

Amp_2 crystallized at temperatures between 669±15 and 697±9 °C and pressures between 0.62±0.07 and 0.83±0.18 kbar (Supplemental File 3). These conditions plot on the low temperature side of the wet granite solidus, which marks the boundary with the PT conditions of Amp_{1a} - Amp_{1b} crystallization (Figure 11a). This evidence indicates that Amp_2 crystallized during the very first increments of subsolidus cooling, after the complete magma crystallization, in agreement with the textural evidence. At lower temperature of 615±2 °C myrmekite formed and with the progression of cooling, perthites indicate unmixing in K-feldspar between 440±74 and 453±99 °C (Supplemental File 3). Chlorite formed at the lowest temperatures that are around 328±12 °C, based on composition of three grains.

7.3. Methodological approach for country rock barometry

In order to test and validate the pressures obtained for the final emplacement of the pluton, we performed barometric estimates for the crystallization of contact metamorphic assemblages in the country rocks. We applied this method in rocks with contact mineral assemblages with minerals useful for barometric estimates in metapelitic rocks. We selected minerals from single microsites and applied barometers based on net transfer reactions between garnet, biotite, plagioclase, quartz (Hoish 1990; Wu *et al.* 2004), barometer based on net transfer of Fe and Ca in garnet (Wu 2019), and the Mg end-member reaction between spinel, cordierite, and quartz (Vielzeuf 1983). Since the Hoish (1990), Wu et al. (2004), and Wu (2019) barometers are not independent from temperature, we entered temperature estimated with Fe and Mg exchange reaction of garnet and biotite (Perchuk *et al.* 1985; Williams and Grambling 1990; Holdaway 2000; Kaneko and Myano 2004) until convergence of pressures and temperatures. We also applied the Average PT calculation method with THERMOCALC (Powell and Holland 1994; Holland and Powell 1998) relying upon different calculation runs and selecting results with the best fitting index. Average PT results were weight averaged on the basis of fitting index.

7.4. Results from country rock barometry

The estimated pressures for contact metamorphism in country rocks (Supplemental File 4) decrease from NW to SE along the southwestern margin of the pluton. Figure 11b shows weighted averaged pressures estimated in country rocks on the basis of number of estimates and standard deviation (1σ). From a maximum value of

3.49±0.49 kbar, to the west of Rosazza, pressure decreases to 2.12±0.47 kbar between Oropa and Riabella (Figure 11b). Close to M. Tovo, the estimated pressures from two samples are 2.25±0.43 kbar and 2.23±0.76 kbar, whereas southward pressures are 2.24±0.23 and 2.15±0.96 kbar (Figure 11b). This variation trend well matches the variation trend revealed from igneous rocks, even if pressures estimated for country rocks are about 1 kbar higher than pressures estimated in igneous rocks. Since this pressure difference, we rely on pressure estimated from igneous rocks for assessing the intrusion depth of final pluton emplacement. This is because the intrinsic error of the used Al-in-hornblende barometers is between 0.5 and 0.6 kbar and lower than the intrinsic error of barometer used for country rocks, which are between 1.2 - 1.3 kbar. Also, the obtained standard deviation for Al-in-hornblende barometers is lower than the obtained standard deviation for barometer used in country rocks (cfr. Supplemental Files 3, 4).

8. Surface and volume distribution of emplacement temperature and pressure in the pluton

8.1. Methodological approach

In order to quantify the spatial distribution of temperatures and pressures for the emplacement of the pluton, we performed a geological 3D model of the pluton. This model relied on orientation data of the contact surface of the pluton and country rocks and magmatic foliation (Zanoni *et al.* 2008; Zanoni 2016), and on 33 geological cross sections across pluton – country rock contact surface (examples in Figure 3). The geological surfaces were modelled using the software GeoModeller® (https://www.intrepid-geophysics.com/product/geomodeller/) that performs a potential-field interpolation based on the co-kriging spatial analysis to produce a 3D scalar field (McInerney and Guillen 2005; Calcagno *et al.* 2008). Each equipotential iso-surface represents the spatial distribution of a single formation interface, while the gradients of the scalar function correspond to the anisotropy shape parameters and represent the structural orientations. The Periadriatic Line is considered as a discontinuity into the potential field (Lajaunie *et al.* 1997; Guillen *et al.* 2008; Thornton *et al.* 2018). Several potential fields are combined to reconstruct a 3D geological model that relies on the integration between observed data with geological interpretation (Caumon *et al.* 2009; Maxelon *et al.* 2009). Indeed, the geological consistency of the 3D model is verified

through the comparison of the modelled interfaces with the input data, which are both plotted on the topographic surface and cross sections (Zucali *et al.* 2020; Zuffetti *et al.* 2020). 3D formation volumes and shapes are exported as polygonal meshes in ParaView (Ahrens *et al.* 2005; Ayachit 2015) for a better 3D visualization.

Once the 3D geological model is performed and the formation surfaces are modelled, the 3D estimate of temperature and pressure variation within the pluton can be done through the Inverse Distance Weighting (IDW) spatial interpolation method (Burrough and McDonnell 1998; Longley *et al.* 2001). IDW method is useful to generate iso-surfaces (i.e., unknown value) starting from an array of known attribute values available as punctual locations (Lu and Wong 2008). During the interpolation, it is fundamental considering the spatial density of the input data point through the distance-decay parameter that it is a function of the neighbourhood point pattern. GeoModeller algorithm uses an adaptive distance-decay parameter that is assigned according to the spatial pattern of neighbourhood points to reflect the spatial variability of input point distribution (Fotheringham 1997). For instance, when the input point pattern is dispersed the reliable source for the estimate will come from the closest data input locations and consequently a higher number of neighbourhood points is necessary (Getis and Ord 1992; Lu and Wong 2008). In that case, as temperature and pressure are punctual input values, we considered the weighted averages of thermobarometrical results by taking into account the standard deviation and number of estimates for each method and sample.

8.2. 3D modeling results

The modelled volume of 110 km^3 was voxelized into a regular and orthogonal 3D triangular mesh and geological properties were attributed to each voxel. In the x-y-z directions the voxel dimension was 50-50-15 m and the entire volume was discretized in 2.289 x 10^6 voxels. Figure 12 shows the 3D geological model of the pluton (syenitic-granitic and monzonitic complexes), emplaced in the basement rocks of Eclogitic Micaschists Complex. The basement is in tectonic contact with the Southern Alps through the Periadriatic Line steeply dipping towards NW (e.g. Schmid *et al.* 1989; Handy *et al.* 2005).

We used all PT estimates for the crystallization of the pluton (Supplemental File 3) except those from sample R1, in the southwestern margin (Riabella), which represents an anomaly as crystallized at higher temperatures and pressures than rocks in the immediate surrounding areas (Figure 11b). This sample can be interpreted as deriving from a magma batch that crystallized at deeper level, or the higher content in biotite may correspond to a higher Al content in bulk rock composition and responsible for a relatively higher content in Al in hornblende, which would make the PT estimates retrieved not directly comparable with those from other samples. However, since the buffer mineral assemblage for the application of Al-in hornblende barometer occurs in this sample (e.g. Schmidt 1993; Mutch *et al.* 2016), we conclude that R1 represents a batch of magma that crystallized deeper than the surrounding monzonite.

Data points with attributed temperature and pressures for the crystallization of Amp_{1a} and Amp_{1b} were used as physical property into drill-holes located with the x-y coordinates of the samples and z-dimension of 0.10 m. Once the drill-holes mesh grid was computed, the IDW interpolation, with maximum radius of neighbourhood parameters settled at 4100 voxels, created the pressure and temperature grid with x-y-z cell dimension of 80-90-15 m along the entire modelled volume. Merging the geological modelling, the pressure and temperature interpolations were visualized only within the monzonitic complex (Figure 13). In order to compare the interpolation for Amp_{1a} and Amp_{1b}, we managed the color-coding histogram considering the minimum and maximum interpolated value and dividing the interpolation result into regular intervals ($\Delta P = 0.17$ kbar and $\Delta T = 10°C$). The range of statistically interpolated pressure lies from 0.84 to 2.55 kbar, whereas the interpolated temperature lies from 711 to 787 °C. Although corresponding voxel shows higher pressure values for Amp_{1a} than for Amp_{1b}, both Amp_{1a} and Amp_{1b} interpolations are characterized by a higher values at the northwestern corner of pluton and an appreciable gradient toward the Periadriatic Line (Figure 13a, b). The temperature interpolation displays a well-defined cooling from Amp_{1a} to Amp_{1b} showing an irregular variation within the pluton (Figure 13c, d).

The boundary between the chosen pressure steps for Amp_{1b} were handled as isobaric surfaces, which were modelled as geological interfaces within the monzonitic complex. The intersections between the modelled isobaric surfaces and the drill-holes were considered as new punctual pressure values. These new punctual pressures were used to refine the IDW interpolation and constrain the isobaric surfaces until the best

convergence between natural and modelled data. Figure 14 shows eight isobaric surfaces modelled for Amp_{1b} within the pluton in 2-dimensions (Figure 14a) and in 3-dimensions (Figure 14b). The isobaric surface orientations are summarized in a stereonet (Figure 14c) showing a mean orientation with a dip azimuth of 122±14° and a dip of 71±3°. The dip value can be considered as the value of the post-intrusive rotation. Using the Bingham Axial Distribution analysis (Fischer *et al.* 1987), we inferred the third eigenvector as the rotation axis, which trends N 35±2° and plunges 12±2°.

9. Discussions

9.1. Cooling history of the Biella monzonite and magma chamber dynamics

The microstructural analysis reveals that the first mineral phases that crystallized from the magma are clinopyroxene and plagioclase ($Pl_{pre\text{-}1}$). These minerals show evidence of reaction with residual melt. This is consistent with irregular boundaries of Pl_{pre1} grains (e.g. Vernon 2004) that likely reacted and were consumed before being included in K-feldspar and with Amp_{1a} (hornblende) that developed at the rim and along cleavages of clinopyroxene (e.g. Smith 2014; Nandedkar *et al.* 2016). The general decrease of anorthite content in plagioclase, from $Pl_{pre\text{-}1}$ to Pl_{1b} also testifies the change of residual melt composition. In monzonite, K-feldspar and plagioclase (inner Pl_{1a} and outer Pl_{1b}) are the main phases that mark the almost ubiquitous magmatic foliation. The magmatic foliation is preserved only if the viscosity of the magma is high enough to prevent a further dispersion of crystals by continuous magma flow. Therefore, the magmatic foliation records the last increment of deformation (i.e. magma flow) in the magma chamber during last cooling stages (e.g. Paterson *et al.* 1998; Petford 2003). The increase in magma viscosity is also due to the increase in the amount of crystals as the cooling progress (e.g. Cruden 1990; Rosenberg and Handy 2005). The progressive increase of solid particles facilitates the mechanical interaction between crystals when melt is still present, as it is testified by fractures in K-feldspar crystals, which mark the foliation, filled by quartz mono-crystals (e.g. Vernon 2000). Amphibole marks the magmatic foliation (Amp_{1a}) and forms also anhedral interstitial crystals (Amp_{1b}). These microtextures suggest that amphibole (inner Amp_{1a} and outer Amp_{1b}) started crystallizing with K-feldspar and plagioclase (Pl_{1a} and Pl_{1b}) but ended its crystallization after (interstitial Amp_{1b}). This interpretation is also consistent with decreasing of Al and Ti from Amp_{1a} to Amp_{1b} (Figure 6d, 7a). Titanite crystallized in two separate stages;

Ttn_{1a} crystallized earlier and formed euhedral to subhedral crystals and rare Ttn_{1b} crystallized later as interstitial crystals. Since Ttn_{1a} is enclosed in amphibole could have finished its crystallization before amphibole, whereas Ttn_{1b} could have finished to crystallize with Amp_{1b}.

Temperature and pressure estimates on amphibole crystallization indicate that Amp_{1a} formed at P and T slightly higher than Amp_{1b} (Supplemental File 3). In general, temperature and pressure for amphibole crystallization decrease from north to south (Figure 11b, Figure 13) and the same variation trend is also estimated for the pressure of development of contact metamorphism in country rocks. The surface distribution of temperature (i) mimics the pressure variation with less clear trend, (ii) the temperature variation throughout the pluton is smaller relatively than pressure variation, and (iii) the temperature distribution for Amp_{1a} shows a less clear variation trend with respect to the temperature distribution for Amp_{1b}. These observations suggest a weak influence of depth on crystallization temperature, according to a near-vertical Amp-in curve for a tonalitic system (Schmidt 1993).

The finer-grained texture and the scarce magmatic foliation of sample R1 may suggest that this is a portion of monzonite that undercooled and dropped as solid block in the magma, and then was carried upward during final emplacement. This is consistent with the capability of magma flow to carry upward xenoliths (e.g. Ferreira *et al.* 2015; Burchard *et al.* 2016; Lesher 2017; Kokandakar 2018; Sun *et al.* 2018).

Textural relationships suggest that Amp_{1b} is the most suitable phase for constraining the final emplacement conditions. The higher pressure for Amp_{1b} crystallization is constrained at 2.27±0.46 kbar, under temperature of 750±23 °C, just west of Rosazza, whereas the lowest pressure is constrained at Riabella at 0.87±0.17 kbar and close to Monticchio at 0.91±0.29 kbar, under temperature of 721±34 and 709±16 °C, respectively. The lowest values of the PT range well fit the wet granite and tonalite solidus (Figure 11b), and this is consistent with the textural interpretation of Amp_{1b} as one of the last phases that crystallized right at the complete solidification of the magma.

After the complete crystallization, sub-solidus crystallization of Amp_2 took place between 650 and 700°C and 0.6 and 1 kbar, just crossed the wet granite and

tonalite solidus (Figure 11a). The actinolitic composition of Amp_2 and its crystallization at margin and along fractures and cleavages of hornblende (Amp_{1a} and Amp_{1b}), may suggest that Amp_2 crystallization took place during the circulation of residual magmatic fluids, inducing hydrothermal alteration (e.g. Agemar *et al.* 1999). Crystallization temperatures of Amp_2 are slightly higher than those estimated for myrmekite formation at K-feldspar rims, which also require fluids (Garcia *et al.* 1996; Abart *et al.* 2014), and are thus ascribable to hydrothermal circulation as well. With decreasing temperature, K-feldspar unmixed and perthites developed between 440±74 and 453±99 °C. Moreover, Kfs contains flame perthites that along with myrmekites are consistent with sub-solidus intracrystalline deformation (e.g. Pryer and Robin 1995; Abart *et al.* 2014), as the undulose extinction in interstitial quartz crystals. Chlorite associated with epidote or rarely titanite (Ttn_{2b}), grew mostly at the expenses of biotite, but also in intergranular spaces. The chlorite composition matches that of hydrothermal chlorite replacing igneous biotite (e.g. Parry and Downey 1982). Thus, chlorite development conditions at temperature of 328±12 °C, are interpreted as those of the coolest hydrothermal fluid circulation. These conditions are similar to those estimated for tourmaline and carbonate ore-bearing vein systems in the country rocks and volcaniclastic cover at Passobreve (Bernardelli *et al.* 2000). Hydrothermal systems are also testified by veining and mineralized fault zones intersecting country rocks in Val Sessera and close to M. Tovo (Rossetti *et al.* 2007; Zanoni *et al.* 2008; Zanoni 2016). On the other hand, in monzonitic rocks, fractures mineralized with chlorite and epidote are consistent with fluid circulation during thermal contraction induced by cooling (Zanoni *et al.* 2008; Zanoni 2016). In conclusion, Amp_2, myrmekites, and chlorite and epidote, may evidence three hydrothermal temperature steps related to a continuous cooling in time.

9.2. Constraints on pluton emplacement, size, and timing

Considering the maximum and minimum pressure estimated for Amp_{1b} and taking into account densities of 2820 and 2750 kg/m^3 for average continental crust and granitic rocks respectively (Christensen and Mooney 1995; Vilà *et al.* 2010), the shallowest and deepest exposed part of the pluton emplaced at 2.99±0.77 km and 8.33±1.13 km, respectively. The shallow level of emplacement is consistent with pluton intersecting all ductile structures in the country rocks (Figure 3), with brittle structures syn-dating and postdating the pluton emplacement, with contact metamorphism postdating the regional greenschist-facies metamorphism, and with active erosion of the

Sesia-Lanzo Zone rocks few kilometres above the pluton roof, during magma emplacement (Zanoni *et al.* 2008, 2010; Zanoni 2016). Also, shallow level is consistent with local complex geometry of the contact of pluton and country rocks, such as in vicinity of Oropa and Bochetto Sessera (Figure 2, Figure 12).

The geometry of the pluton is consistent with stopping and caldera subsidence as suggested by fractures and abundance of xenoliths, particularly between Oropa and Riabella, and in Val Sessera (Bigioggero and Tunesi 1988; Zanoni *et al.* 2010; Zanoni 2016). These passive mechanisms are consistent with local dispersed orientation of magmatic foliation (Figure 2) and magnetic fabric, and orientation of the regional fabric of country rocks that in place controls the geometry of pluton margin (Hrouda and Lanza 1989; Zanoni *et al.* 2008, 2010; Zanoni 2016). Nevertheless, besides passive mechanisms, forceful mechanisms, which involve the ductile deformation of country rocks, are indicated by structural data from the area west of Rosazza (Valle della Pragnetta; Figure 3), where the deeper crystallization pressures of the pluton are estimated and the magmatic foliation shows a quite homogenous orientation (Figure 2) that progressively approaches that of pluton margin (Zanoni *et al.* 2010; Zanoni 2016).

The Biella monzonite is interpreted as the magmatic reservoir of the shoshonitic lavas within the andesitic cover (Callegari *et al.* 2004), which rests on top of the basal conglomerate. Thus, part of the andesitic cover was fed by shoshonitic dykes that connected the magma reservoir (i.e. the Biella monzonite) with lava fields at palaeosurface. Besides the detailed geochemical analysis by Callegari *et al.* (2004), this interpretation is also supported by the shoshonitic whole rock composition of Biella pluton rocks (Bigioggero *et al.* 1994; Ji *et al.* 2019) and the similar composition of clinopyroxene from monzonite and shoshonitic andesite (Figure 9), which supports the interpretation of Biella pluton as the magmatic reservoir of shoshonite lavas (see also Tornare *et al.* 2016). The pressures of phenocryst crystallization in shoshonitic lavas are between 2.0 and 2.6 kbar (Callegari *et al.* 2004) and match well the highest pressures estimated for crystallization of Amp_{1a} (Supplemental File 3). Taking into account the densities used above, the shoshonitic phenocrysts formed at a depth of 8.46±1.11 km, which is slightly higher than that estimated for the final emplacement of the deeper part of monzonite exposed today. This evidence corroborates the interpretation of shoshonite lavas as deriving from the monzonite reservoir. In this view, the phenocrysts of shoshonites might have crystallized in the deeper part of monzonite magmatic chamber

when monzonitic Amp_{1a} was crystallizing too, and before Amp_{1b} crystallization, so as to say, just before the pluton reached the crustal level of final emplacement. On the contrary, phenocrysts in high-K calc-alkaline andesites started crystallizing between 3.6 and 4.8 kbar (Callegari *et al.* 2004).

The arguments exposed above imply that at least part of the andesitic dykes and lavas should be coeval with the Biella pluton. Instead, the most recent U/Pb data on andesites show the majority concordant ages between 32.44 and 32.89 Ma (Kapferer *et al.* 2012). However, the same authors found U/Pb concordant ages between 31.62 and 32.64 Ma for an andesite clast within the cover, widening the time span for the emplacement of andesite lava flows from 0.45 Myr to 1.27 Myr. High-K calc-alkaline andesite lavas contain xenoliths of eclogitic micaschists and gneisses, and hornfelses with sillimanite, corundum, spinel, and biotite, possibly deriving from the contact aureole of Biella pluton (Callegari *et al.* 2004). This evidence points out that part of the lavas should be emplaced when the thermal aureole was already formed. Therefore, the age of andesite volcanism could be extended at least up to 30.9±0.2 Ma, which is the maximum U/Pb age of monzonite (Romer *et al.* 1996). On the other hand, K/Ar andesite ages are between 29 and 33 Ma (Scheuring *et al.* 1974).

Considering the final level of emplacement estimated above, the thickness of the Biella pluton is estimated at 5.34±0.95 km and from its areal extent, it could had been about 270 km^3 in volume. Comparing it with other igneous composite complexes with similar size, the emplacement times could had been between 50 and 150 kyr (Petford *et al.* 2000; Cruden and McCaffrey 2001; Michel *et al.* 2008; Caricchi *et al.* 2012). Such a short time is consistent with syenite emplacing when monzonite is still partially a crystal mush (Bigioggero *et al.* 1994). On the other hand, zircon U/Pb ages indicate an interval between 30.1±0.2 Ma and 30.9.0±0.2 Ma, with younger ages related to the syenite-granite complex and older ages to the outer part of monzonite complex (Romer *et al.* 1996; Berger *et al.* 2012a; Ji *et al.* 2019). These data and considerations indicate that the full crystallization below the solidus was accomplished in a time interval comprised between 100 kyr and 800 kyr. Since close time relationships have been proved between batholiths and rhyolitic volcanism (Glazner *et al.* 2004) and monzonite and syenite-granite complexes derive from two separate batch sources (Bigioggero *et al.* 1994), we tentatively propose that to complete the emplacement, from monzonite to central white granite, it could have taken a time span closer to 800 kyr than 100 kyr.

This time interval should be plausible speculating about monzonite being solid in the outer part and a crystal mush in the inner part when syenite intruded, and about the time for syenite to crystallize and differentiate in sequence the pink and white granite.

9.3. Implication for post-emplacement tectonics of the internal Sesia-Lanzo Zone

From palaeomagnetic analysis of andesitic dykes a minimum rotation of 40° was envisaged in the internal part of the Sesia-Lanzo Zone, and taking into account the present orientation of the andesitic cover and palaeomagnetic data from andesite dykes within the Periadriatic mylonites, a southeastward rotation of 60-70° about an axis N 18-20° is envisaged (Lanza 1977, 1978; Schmid *et al.* 1989). Recently, the interpretation on the rotation has been updated on the basis of zircon and apatite fission tracks from the basement of the Sesia-Lanzo Zone, andesitic cover, and Biella pluton rocks. After its emplacement, the andesitic cover experienced thermal conditions up to 250 °C, at ages between 18 and 24 Ma, according to zircon fission tracks (Scheuring *et al.* 1974; Zingg *et al.* 1976; Kapferer *et al.* 2011, 2012). These ages and temperatures are explained with a tectonic burial of the andesitic sequence that eventually passed through the apatite annealing zone between 15 and 20 Ma, during final exhumation (Kapferer *et al.* 2012). Since zircon and apatite fission track ages for the Biella pluton are younger than those for the andesites, it is interpreted that the rotation involved the Sesia-Lanzo Zone rocks and andesitic dykes and lavas, and predated the emplacement of the Biella pluton (Berger *et al.* 2012b). The available time for the internal part of Sesia-Lanzo Zone with the andesitic cover on top (Cervo block) to rotate is interpreted of about 2 Myr, considering the age of white central granite and an average of 32 Ma for the end of andesitic volcanic activity (Berger *et al.* 2012a; Kapferer *et al.* 2012). Nevertheless, U/Pb age of 31 Ma for the outer monzonite and 31.62 - 32.64 Ma for an andesite clast in the cover, shrink this time interval at less than 1 Myr (i.e. not shorter than 0.6 Myr).

The observations that support the pre-intrusive rotation of the Cervo block are (i) the present day shortest distance of 0.7 km between the pluton and the volcanic rocks that is much minor than 4 km estimated for the depth of the pluton roof (Zanoni *et al.* 2010), (ii) the lack of faults between the Biella pluton margin and the andesitic cover and (iii) mineralized veins in the andesitic cover (Bernardelli *et al.* 2000) that indicate

the proximity with the pluton, and (iv) the magnetic fabric pattern typical of the pluton roof (Hrouda and Lanza 1989), which is not affected by subsequent deformation (Kapferer *et al.* 2011; Berger *et al.* 2012b).

Alternatively, the present-day distance from the pluton margin and the andesitic cover possibly did not change much and the missing crustal section above the roof of Biella pluton can be explained by tectonic erosion operated by the Periadriatic Line activity. Indeed, after the emplacement of Rupelian igneous rocks, thrusting and a minor strike slip movement are responsible for the uplift and 60° rotation of the Cervo block, and the present-day pinching of the andesitic cover between Sesia-Lanzo Zone rocks and the Periadriatic Line (Schmid *et al.* 1989). Since the present-day shortest distance from the pluton margin and the Periadriatic Line is about 1 km, and the depth of the pluton roof was about 3 km, as it is refined in this work, about 2 km thick of the andesitic cover is missing. This is possible because the andesitic cover is considered as the remnants of stratovolcanos (Kapferer *et al.* 2012), which typically can be few kilometer-thick (i.e. present-day Mount Etna stratovolcano is about 3 km thick).

The interpretation of the magnetic fabric as resulting from magmatic flow at the roof, is actually due because samples for magnetic analysis were not collected west of Rosazza (Valle della Pragnetta), where structural relationships and orientation of the magmatic foliations are compatible with the deeper part of the pluton (Zanoni 2016 and refs. therein).

The largest tectonic feature intersecting the Biella pluton is the presumed fault that runs along the axis of Valle del Cervo, which from the map, it does not seem responsible for an important offset (Malaroda *et al.* 1966). Other minor faults intersect the Biella pluton and accommodated strike slip kinematics but with negligible offset (Zanoni *et al.* 2008). Only a meter-thick cataclastic band is interpreted as reverse fault (cross section C-C' in Figure 3) with a possible top-to-the-south kinematics, but also in this case without important offset (Zanoni 2016).

From the pressure distribution and the 3D geological model we reconstruct the rotation angle of the Biella pluton in two different ways. First, taking into account the mean dip azimuth and dip of the isobaric surfaces reconstructed with the 3D model, we envisage a rotation of about 71±3°. Bingham statistics of isobaric surface orientation

disclosed an N 35° trending and 12° plunging rotation axis. Second, we obtain the rotation angle as the complementary of the angle calculate from the inverse of cosine of the ratio between the depth difference calculated from the pressures of the two data points (Δh) and the shortest distance between the data points with highest and lowest pressure estimate for Amp_{1b}, measured orthogonally to the isobaric lines (Δx):

$$(\text{rot. angle} = 90 - \cos^{-1}\frac{\Delta h}{\Delta x})$$

We estimate a rotation angle between 63° and 69°. The two methods give similar rotation angles comprised between 63 and 74°. Therefore, we conclude that the Biella pluton experienced a post-emplacement rotation of ca. 69±5°, about a sub-horizontal axis sub-parallel to the Periadriatic Line, and towards southeast.

The most relevant observation supporting a post-intrusive rotation of the Cervo block is the pressure gradient that suggests an increase in the crystallization depth of the pluton from SE to NW (Figures 11 and 12), compatible with a rotation of the pluton too. Today, the Valle del Cervo slopes expose a portion of the pluton comprised between 700 and 2200 m a.s.l., thus over a thickness of 1.5 km. The pressure difference recorded by collected samples results in a thickness of at least 4.39 km, i.e. three times of the present-day thickness of plutonic rocks that Valle del Cervo slopes expose. Since faults involving kilometric vertical displacement have not been observed, this implies that the pluton can not be in its original position (i.e. emplacement position) at present, but it must have somehow rotated after the emplacement. In addition, the occurrence of 10 metre-sized country rock xenoliths at Riabella is consistent with this area being part of the pluton roof (e.g. Yoshinobu *et al.* 2003).

Our results fully confirm the rotation estimated with palaeomagnetic analysis (Lanza 1977, 1978; Schmid *et al.* 1989), and that the pluton rotated with its cover after the emplacement. This interpretation is also consistent with the shoshonitic andesitic lavas fed by monzonite reservoir and by the possible occurrence of xenoliths from the Biella contact aureole in high-K calc-alkaline lavas (Callegari *et al.* 2004).

9.4. Reconciling of fission track timing and Al-in-hornblende barometry

In this section, alternative interpretations to fission track data available for country rocks, pluton, and andesite cover are given (Berger *et al.* 2012b; Kapferer *et al.* 2012). These interpretations are based on the ages assessed by the authors, which in some cases can be difficult to interpret due to a long stay of rocks in the zircon annealing zone or to zircon grains without complete resetting of radiation damages (e.g. Rahn *et al.* 2019; Tagami and Matsu'ura, 2019). Zircon and apatite fission track ages in the basement of Sesia-Lanzo Zone are at 35 Ma and between 25.6 and 29.7 Ma, respectively, and are older than those from the pluton, which are between 20.5 and 17.9 Ma, and 11.9 and 16.1 Ma, respectively (Hurford and Hunziker 1985; Berger *et al.* 2012b). Fission tracks in the basement are explained with the exhumation after the burial of basement country rocks consequent to the rotation of the Cervo block, while those in the pluton would represent its continuous cooling (Berger *et al.* 2012b). Alternatively, the zircon fission tracks at 35 Ma in the country rocks (Monte Mucrone) can be interpreted as the result of a continuous uplift from greenschist-facies conditions to the zircon annealing temperature conditions. This is coherent with a necessary erosion of the Sesia-Lanzo Zone before the onset of the andesite volcanism at 32.89 Ma, because the Rupelian conglomerate at the bottom of the andesite volcaniclastic sequence contains exclusively clasts deriving from the Sesia-Lanzo Zone rocks (i.e. outcrops at Passobreve). Younger apatite fission tracks in the basement rocks are recorded in portions that were exhumed later than the onset of the erosion, which must be earlier than 32.89 Ma.

Zircon and apatite fission tracks in the andesitic cover indicate ages comprised between 24.2 and 19 Ma, and 15.5 and 20 Ma, respectively (Kapferer *et al.* 2012). Considering a thermal gradient of 50°C/km, the zircon ages have been interpreted as the result of a tectonic burial of andesites at a depth of 5 km (Kapferer *et al.* 2012). Assuming a total thickness of the andesitic cover of about 2.3 km, which would have grown over a time laps longer than 1 Myr, the pluton could have emplaced before the rotation of the Cervo block. The total burial of 5 km of the andesite cover can be related in part to the deposition and in part to tectonics. In order to reach 5 km depth for the andesite cover, we envisage a first southeastward rotation stage accompanied by burial that should have taken place before 26 Ma, which is the age for the onset of back-thrusting on the Periadriatic Line causing the uplift of the Cervo block (Schimd *et al.*

1989; Zingg and Hunziker 1990). After 26 Ma the back-thrusting started with on-going rotation and was responsible for the uplift of the Cervo block and for andesites to overtake the zircon annealing zone with new fission tracks recorded between 24 and 19 Ma, and eventually the apatite annealing zone between 20 and 15 Ma. This interpretation is reliable because today only the deepest part (the deepest 300 – 500 m) of the andesite cover is exposed, while the upper part has been removed during the rotation. The back-thrusting accommodated by the Periadriatic Line nearby the Biella pluton uplift the Cervo block up to 3 km (Handy *et al.* 2005). This vertical offset fits with the tectonic removal of 2 km-thick rock layer from the top of Biella pluton required to explain the present-day shortest distance of about 1 km (Valle del Cervo section) between the pluton margin and the Periadriatic Line. In this way, the first part that reached the apatite annealing zone would have been the bottom of the pluton, followed by the upper part (Figure 15).

Summarizing, we envisage the following tectonic evolution:

1 - between 35 and 33 Ma the Sesia-Lanzo Zone rocks were exhumed and the Rupelian basal conglomerate was deposited; at about 33 Ma the high-K calc-alkaline andesitic volcanism onset (Figure 15a).

2- soon after, shoshonitic volcanism was fed by the Biella monzonite and possibly lasted until 31 Ma, when the monzonitic complex emplaced. At the same time at least 2.3 km-thick volcaniclastic sequence developed (Figure 15b).

3 - at 30.5 Ma syenite complex emplaced with sequential differentiation of pink and white granites (Figure 15c).

4 - before 26 Ma the Cervo Block experienced a first southeastward rotation stage involving the burial of the bottom of andesite cover up to 5 km depth (Figure 15d).

5 - after 26 Ma the uplift of the Cervo block is associated with continuation of the southeastward rotation by back-thrusting along the Periadriatic Line. Zircon fission tracks formed between 24 and 19 Ma in the andesite cover and continuous rotation and uplift of the Cervo block resulted in the cooling of the pluton below the zircon annealing zone between 20.5 and 18 Ma (Figure 15e).

6 - the continuation of southeastward rotation was responsible for the andesite and pluton cooling below apatite annealing zone between 20 and 15 Ma, and 16 and 12 Ma, respectively (Figure 15f). The rotation could have continued also after 12 Ma.

The effect of two-stage rotation may have involved a contrasted path for pluton roof and bottom. The pluton roof would have experienced tectonic burial together with the bottom of andesite cover before 26 Ma, whereas the bottom would have experienced uplift during both rotation stages (Figure 16). Even though the fission track ages are all within error, in the pluton they generally decrease from northwest to southeast (Figure 7 in Kapferer *et al.* 2012 and Figures 3 and 4 in Berger *et al.* 2012), according to the same trend of decrease in the crystallization pressure. This evidence can be interpreted as a progressive exhumation of the pluton from northwest to southeast, and thus compatible with rotation of the pluton after emplacement. This is also consistent with the pluton bottom reaching shallower levels before the roof, sometime after 26 Ma (Figure 16).

Figure 15g shows the present-day situation by means of the interpreted section along the Valle del Cervo axis, and suggest that possibly half of the original volume of the pluton is lost and only a small part (the deepest) of the possible original volume of the andesite cover is left. Finally, from Passobreve to Rosazza deeper levels of the pluton are reached.

10. Conclusion

On the basis of multiscale structural analysis and thermobarometric estimates we reconstructed the cooling history and refined the emplacement conditions of the Biella pluton, within the internal part of the Sesia-Lanzo zone, during early Oligocene. Clinopyroxene and Ca-rich plagioclase were the first phases that crystallized from the monzonitic magma and reacted because of the changing in composition of the residual melt. A magmatic foliation formed and quenched when the crystallization was almost complete. The outer part of amphibole crystals and interstitial amphibole are among the last crystallized minerals. The pluton cooling was followed by hydrothermal circulation that started at temperature just below the solidus at pressure less than 1 kbar, and ended at temperature lower than 350 °C. Barometrical results point out depths of magmatic emplacement about between 8.5 and 3.0 km for the deeper and shallower part of the pluton, respectively. Pressures and temperatures are comprised between 0.9 and 2.3

kbar and 710 and 750 °C and decrease southeastward, suggesting a post-intrusive rotation of the pluton that involved the exhumation of the deepest parts in the areas more distant from the Periadriatic Line. Above the pluton roof at least 2.3 km of andesite volcanoclastite accumulated, starting before the pluton emplacement, at about 33 Ma, and lasting possibly until the emplacement of the monzonite complex at 31 Ma. By 3D statistical analysis of surface and volume distribution of crystallization pressure and temperature of the pluton, isobaric surfaces are interpolated. Considering that at the emplacement times isobaric surfaces were horizontal, we envisage a southeastward rotation of 69±5° about a sub-horizontal axis trending N 35°. The rotation was accompanied first by tectonic burial and afterwards by a vertical uplift, both assisted by sliding on the Periadriatic Line that caused erosion and/or tectonic removal of most part of the andesitic cover throughout late Oligocene and early Miocene and possibly also over more recent times.

Acknowledgments

We acknowledge supportive comments and suggestions by two anonymous reviewers and editor Robert J. Stern. Tessa Donigaglia set the GIS database and helped with part of the acquisition of microprobe data and mineral formula calculation. Agostino Rizzi and Andrea Risplendente assisted the work at the SEM and microprobe. This paper is framed within the MIUR project "Dipartimenti di Eccellenza 2017 - Le geoscienze per la società: risorse e loro evoluzione".

References

Abart, R., Heuser, D., and Habler, G., 2014, Mechanisms of myrmekite formation: case study from the Weinsberg granite, Moldanubian zone, Upper Austria: Contributions to Mineralogy and Petrology, v. 168, 1074. https://doi.org/10.1007/s00410-014-1074-7.

Agemar, T., Wörner, G., and Heumann, A. 1999, Stable isotopes and amphibole chemistry on hydrothermally altered granitoids in the North Chilean Precordillera: a limited role for meteoric water?: Contributions to Mineralogy and Petrology, v. 136, p. 331-344. https://doi.org/10.1007/s004100050542.

Ague, J.J., and Brandon, M.T., 1992, Tilt and northward offset of Cordilleran batholiths resolved using igneous barometry: Nature, v. 360, p. 146-149. https://doi.org/10.1038/360146a0.

Ague, J.J., and Brandon, M.T., 1996, Regional tilt of the Mount Stuart batholith, Washington, determined using aluminum-in hornblende barometry: Implications for northward translation of Baja British Columbia: GSA Bulletin, v. 108 (4), p. 471-488. https://doi.org/10.1130/0016-7606(1996)108<0471:RTOTMS>2.3.CO;2.

Alagna, K.E., Peccerillo, A., Martin, S., and Donati, C., 2010, Tertiary to Present evolution of orogenic magmatism in Italy: Journal of the Virtual Explorer, v. 36, 18. DOI: 10.3809/jvirtex.2010.00233.

Aleinikoff, J.N., Wintsch, R.P., Fanning, C.M., and Dorais, M.J., 2002, U-Pb geochronology of zircon and polygenetic titanite from the Glastonbury Complex, Connecticut, USA: an integrated SEM, EMPA, TIMS, and SHRIMP study: Chemical Geology, v. 188, p. 125-147. https://doi.org/10.1016/S0009-2541(02)00076-1.

Anderson, J.L., Barth, A.P., Wooden, J.L., and Mazdab, F., 2008, Thermometers and thermobarometers in granitic systems: Reviews in Mineralogy and Geochemistry, v. 69, p. 121-142. https://doi.org/10.2138/rmg.2008.69.4.

Anderson, J.L., and Smith, D.R., 1995, The effects of temperature and fO2 on the Al-in-hornblende barometer: American Mineralogist, v. 80, p. 549-559. https://doi.org/10.2138/am-1995-5-614.

Ahrens, J., Geveci, B., and Law, C. 2005, ParaView: An End-User Tool for Large Data Visualization, Visualization Handbook, Elsevier. DOI: 10.1016/B978-012387582-2/50038-1.

Ayachit, U., 2015, The ParaView Guide: A Parallel Visualization Application. Kitware Inc., USA.

Babist, J., Handy, M.R., Konrad-Schmolke, M., and Hammerschmidt, K, 2006, Precollisional multistage exhumation of subducted continental crust: The Sesia Zone, Western Alps: Tectonics, v. 25, TC6008. https://doi.org/10.1029/2005TC001927.

Bachl, C.A., Miller, C.F., Miller, J.S., and Faulds, J.E., 2001, Construction of a pluton: Evidence from an exposed cross section of the Searchlight pluton, Eldorado Mountains, Nevada: GSA Bulletin, v. 113 (9), p. 1213-1228. https://doi.org/10.1130/0016-7606(2001)113<1213:COAPEF>2.0.CO;2.

Beccaluva, L., Bigioggero, B., Chiesa, S., Colombo, A., Fanti, G., Gatto, G.O., Gregnanin, A., Montrasio, A., and Tunesi, A., 1983, Post-collisional orogenic dyke magmatism in the Alps: Memorie della Società Geologica Italiana, v. 26, p. 341-359.

Benisek, A., Dachs, E., and Kroll, H., 2010, A ternary feldspar-mixing model based on calorimetric data: development and application: Contributions to Mineralogy and Petrology, v. 160 p. 327-337. https://doi.org/10.1007/s00410-009-0480-8.

Benisek, A., Kroll, H., and Cemič, L., 2004, New developments in two-feldspar thermometry: American Mineralogist, v. 89, p. 1496-1504. https://doi.org/10.2138/am-2004-1018.

Berger, A., Thomsen, T.B., Ovtcharova, M., Kapferer, N., and Mercolli, I., 2012a, Dating emplacement and evolution of the orogenic magmatism in the internal Western Alps: 1. The Miagliano Pluton: Swiss Journal of Geosciences, v. 105, p. 49-65. https://doi.org/10.1007/s00015-012-0091-7.

Berger, A., Mercolli, I., Kapferer, N., and Fügenschuh, B., 2012b, Single and double exhumation of fault blocks in the internal Sesia-Lanzo Zone and the Ivrea-Verbano Zone (Biella, Italy): International Journal of Earth Sciences (Geologische Rundschau), v. 101, p. 1877-1894. https://doi.org/10.1007/s00531-012-0755-6.

Bergomi, M.A., Zanchetta, S., and Tunesi, A., 2015, The Tertiary dike magmatism in the Southern Alps: geochronological data and geodynamic significance: International Journal of Earth Sciences, v. 104 (2), p. 449-473. https://doi.org/10.1007/s00531-014-1087-5.

Bernardelli, P., Castelli, D., and Rossetti, P., 2000, Tourmaline-rich ore-bearing hydrothermal system of lower Valle del Cervo (Western Alps, Italy): Field relationships and petrology: Schweizerische Mineralogische und Petrographische Mitteilungen, v. 80, p. 257-277.

Bigioggero, B., Colombo, A., Del Moro, A., Gregnanin, A., Macera, P., and Tunesi, A., 1994, The Oligocene Valle del Cervo Pluton: An example of shoshonitic magmatism in the Western Italian Alps: Memorie di Scienze Geologiche, Padova, v. 46, p. 409-421.

Bigioggero, B., and Tunesi, A., 1988, The "Valle del Cervo" plutonic body. Notes to the field trip on 1st October 1987: Rendiconti della Società Italiana di Mineralogia e Petrologia, v. 43, p. 355-366.

Bourdelle, F., Parra, T., Chopin, C., and Beyssac, O., 2013, A new chlorite geothermometer for diagenetic to low-grade metamorphic conditions: Contributions to Mineralogy and Petrology, v. 165, p. 723-735. https://doi.org/10.1007/s00410-012-0832-7.

Burchardt, S., Troll, V.R., Schmeling, H., Koyi, H., and Blythe, L., 2016, Erupted frothy xenoliths may explain lack of country-rock fragments in plutons: Scientific Reports 6, 34566. https://doi.org/10.1038/srep34566.

Calcagno, P., Chilès, J.P., Courrioux, G., and Guillen, A., 2008, Geological modelling from field data and geological knowledge. Part I. Modelling method coupling 3D potential-field interpolation and geological rules: Physics of the Earth and Planetary Interiors, v. 171, p. 147-157. https://doi.org/10.1016/j.pepi.2008.06.013.

Callegari, E., Cigolini, C., Medeot, O., and D'Antonio, M., 2004, Petrogenesis of calcalkaline and shoshonitic post-collisional Oligocene volcanics of the Cover Series of the Sesia Zone, Western Italian Alps: Geodinamica Acta, v. 17, p. 1-29. https://doi.org/10.3166/ga.17.1-29.

Caricchi, L., Annen, C., Rust A., and Blundy J., 2012, Insights into the mechanisms and timescales of pluton assembly from deformation patterns of mafic enclaves: Journal of Geophysical Research: Solid Earth, v. 117, B11206. https://doi.org/10.1029/2012JB009325.

Carraro, F., and Ferrara, G., 1968, Alpine ‘tonalite’ at Miagliano, Biella (Zona Diorito-kinzigitica): Schweizerische Mineralogische und Petrographische Mitteilungen, v. 48, p. 75-80.

Caumon, G., Collon-Drouaillet, P., Le Carlier De Veslud, C., Viseur, S., and Sausse, J., 2009, Surface-based 3D modeling of geological structures: Mathematical Geosciences, v. 41, p. 927-945. https://doi.org/10.1007/s11004-009-9244-2.

Cenki-Tok, B., Oliot, E., Rubatto, D., Berger, A., Engi, M., and Janots, E., 2011, Preservation of Permian allanite within an Alpine eclogite facies shear zone at Mt Mucrone, Italy: Mechanical and chemical behavior of allanite during mylonitization: Lithos, v. 125, p. 40-50. https://doi.org/10.1016/j.lithos.2011.01.005.

Cesana, A., Demonte, L., and Venegoni, M., 1976, Origin of the Cervo pluton according to the U and Th content and distribution: Rendiconti della Società Italiana di Mineralogia e Petrologia, v. 32, p. 637-646.

Christensen, N.I., and Mooney, W.D., 1995, Seismic velocity structure and composition of the continental crust: A global view: Journal of Geophysical Research: Solid Earth, v. 100, p. 9761-9788. https://doi.org/10.1029/95JB00259.

Compagnoni, R., Dal Piaz, G.V., Hunziker, J.C., Gosso, G., Lombardo, B., and Williams, P.F., 1977, The Sesia-Lanzo Zone: A slice of continental crust, with alpine HP-LT assemblages in the Western Italian Alps: Rendiconti della Società Italiana di Mineralogia e Petrologia, v. 33, p. 281-334.

Corti, L., Alberelli, G., Zanoni, D., and Zucali, M., 2017, Analysis of fabric evolution and metamorphic reaction progress at Lago della Vecchia-Valle d'Irogna, Sesia-Lanzo Zone, Western Alps: Journal of Maps, v. 13, p. 521-533. https://doi.org/10.1080/17445647.2017.1331177.

Corti, L., Alberelli, G., Zanoni, D., and Zucali, M., 2018, Tectonometamorphic evolution of the Lago della Vecchia metaintrusive and its country rocks, Sesia-Lanzo Zone, Western Alps: Italian Journal of Geosciences, v. 137, p. 188-207. https://doi.org/10.3301/IJG.2018.08.

Cortiana, G., Dal Piaz, G.V., Del Moro, A., Hunziker, J.C., and Martin, S., 1998. ^{40}Ar-^{39}Ar and Rb-Sr dating of the Pillonet klippe and Sesia-Lanzo basal slice in the Ayas valley and evolution of the Austroalpine-Piedmont nappe stack: Memorie di Scienze Geologiche, Padova, v. 50, p. 177-194.

Cruden, A.R., 1990, Flow and fabric development during the diapiric rise of magma: Journal of Geology, v. 98, p. 681-698.

Cruden, A.R., and McCaffrey, K.J.W., 2001, Growth of Plutons by Floor Subsidence: Implications for Rates of Emplacement, Intrusion Spacing and Melt-Extraction Mechanisms: Physics and Chemistry of the Earth (A), v. 26 (4-5), p. 303-315. https://doi.org/10.1016/S1464-1895(01)00060-6.

De Capitani, L., Fiorentini Potenza, M., Marchi, A., and Sella, M., 1979, Chemical and tectonic contributions to the age and petrology of the Canavese and Sesia-Lanzo 'porphyrites': Atti della Società Italiana di Scienze Naturali, v. 120, p. 151-179.

Delleani, F., Spalla, M.I., Castelli, D., and Gosso, G., 2013, A new petro-structural map of the Monte Mucrone metagranitoids (Sesia-Lanzo Zone, Western Alps): Journal of Maps, v. 9 (3), p. 410-424. https://doi.org/10.1080/17445647.2013.800004.

Erdmann, S., Wang, R., Huang, F., Scaillet, B., Zhao, K., Liu, H., Chen, Y., and Faure, M., 2019, Titanite: A potential solidus barometer for granitic magma systems: Comptes Rendus Geoscience, v. 351, p. 551-561. 0.1016/j.crte.2019.09.002.

Ferracutti, G.R., Gargiulo, M.F., Ganuza, M.L., Bjerg, E.A., and Castro, S.M., 2015, Determination of the spinel group end-members based on electron microprobe analyses: Mineralogy and Petrology, v. 109, p. 153-160. https://doi.org/10.1007/s00710-014-0363-1.

Ferreira, V.P., Sial, A.N., Weinberg, R.F., and Pimentel, M.M., 2015, Deep-seated fragmentation, transport of breccia dikes and emplacement: An example from the Borborema province, northeastern Brazil: Journal of South American Earth Sciences, v. 58, p. 300–308. https://doi.org/10.1016/j.jsames.2014.10.006.

Fiorentini Potenza, M., 1959, Distribuzione delle principali facies petrografiche e della radioattività nel plutone "sienitico" di Biella (Valle del Cervo): Rendiconti della Società Mineralogica Italiana, v. 15, p. 89-131.

Fisher, N.I., Lewis, T.L., and Embleton, B.J., 1987, Statistical analysis of spherical data: Cambridge, Cambridge University Press, 329 p.

Fodor, L.I., Gerdes, A., Dunkl, I., Koroknai, B., Pécskay, Z., Trajanova, M., Horváth, P., Vrabec, M., Jelen, B., Balogh, K., and Frisch, W., 2008, Miocene

emplacement and rapid cooling of the Pohorje pluton at the Alpine-Pannonian-Dinaridic junction, Slovenia: Swiss Journal of Geosciences, v. 101 (Suppl. 1), p. S255-S271. https://doi.org/10.1007/s00015-008-1286-9.

Fotheringham, A.S., 1997, Trends in quantitative methods I: stressing the local: Progress in Human Geography, v. 21, p. 58-96. https://doi.org/10.1191/030913297676693207.

Garcia, D., Pascal, M.-L., and Roux, J., 1996, Hydrothermal replacement of feldspar in igneous enclaves of the Velay granite and the genesis of myrmekites: European Journal of Mineralogy, v. 8, p. 703-717. DOI: 10.1127/ejm/8/4/0703.

Getis, A., and Ord, J.K., 1992, The analysis of spatial association by use of distance statistics: Geographical Analysis, v. 24, p. 189-206. https://doi.org/10.1111/j.1538-4632.1992.tb00261.x.

Giuntoli, F., and Engi, M., 2016, Internal geometry of the central Sesia zone (Aosta Valley, Italy): HP tectonic assembly of continental slices: Swiss Journal of Geosciences, v. 109 (3), p. 445-471. https://doi.org/10.1007/s00015-016-0225-4.

Glazner, A.F., Bartley, J.M., Coleman, D.S., Gray, W., and Taylor, R.Z., 2004, Are pluton assembled over millions of years by amalgamation from small magma chambers?: GSA Today, v. 14 (4-5), p. 4-11. doi: 10.1130/1052-5173(2004)014<0004:APAOMO>2.0.CO;2.

Gosso, G., Messiga, B., Rebay, G., and Spalla, M.I., 2010, Interplay between deformation and metamorphism during eclogitization of amphibolites in the Sesia-Lanzo Zone of the Western Alps: International Geology Review, v. 52 (10), p. 1193-1219. https://doi.org/10.1080/00206810903529646.

Grohmann, C.H., Campanha, G.A.C., and Soares, A.V.J., 2011, Openstereo: Um programa livre e multiplataforma para análise de dados estruturais, in: 13° Simpósio Nacional de Estudios Tectônicos, Campinas, SP, 26-28.

Guillen, A., Calcagno, P., Courrioux, G., Joly, A., and Ledru, P., 2008, Geological modelling from field data and geological knowledge. Part II. Modelling validation using gravity and magnetic data inversion: Physics of the Earth and Planetary Interiors, v. 171, p. 158-169. https://doi.org/10.1016/j.pepi.2008.06.014.

Handy, M.R., Babist, J., Wagner, R., Rosenberg, C.L., and Konrad, M., 2005, Decoupling and its relation to strain partitioning in continental lithosphere: insight from the Periadriatic fault system (European Alps), *in* Gapais, D., Brun, J.P., and Cobbold, P.R., eds., Deformation Mechanisms, Rheology and Tectonics: from Minerals to Lithosphere: Geological Society London Special Publications, v. 243, p. 249-276. https://doi.org/10.1144/GSL.SP.2005.243.01.17.

Hoisch, T.D., 1990, Empirical calibration of six geobarometers for the mineral assemblage quartz+muscovite+biotite+plagioclase+garnet: Contributions to Mineralogy and Petrology, v. 104, p. 225-234. https://doi.org/10.1007/BF00306445.

Holdaway, M.J., 2000, Application of new experimental and garnet Margules data to the garnet-biotite geothermometer: American Mineralogist, v. 85, p. 881-892. https://doi.org/10.2138/am-2000-0701.

Holland, T.J.B., and Blundy, J., 1994, Non-ideal interactions in calcic amphiboles and their bearing on amphibole-plagioclase thermometry: Contributions to Mineralogy and Petrology, v. 116, p. 433-447. https://doi.org/10.1007/BF00310910.

Holland, T.J.B., and Powell, R., 1998, An internally consistent thermodynamic data set for phases of petrological interest: Journal of Metamorphic Geology, v. 16, p. 309-343. https://doi.org/10.1111/j.1525-1314.1998.00140.x.

Holland, T.J.B., and Powell R., 2001, Calculation of phase relations involving haplogranitic melts using an internally consistent thermodynamic dataset: Journal of Petrology, v. 42, (4) p. 673-683. https://doi.org/10.1093/petrology/42.4.673.

Hrouda, F., and Lanza, R., 1989, Magnetic fabric in the Biella and Traversella stocks (Periadriatic Line); implications for the mode of emplacement: Physics of the Earth and Planetary Interiors, v. 56, p. 337-348. https://doi.org/10.1016/0031-9201(89)90168-4.

Hurford, A.J., and Hunziker J.C., 1985, Alpine cooling history of the Monte Mucrone Eclogites (Sesia-Lanzo Zone): fission track evidence: Schweizerische Mineralogische und Petrographische Mitteilungen, v. 65 (2-3), p. 325-334.

Inger, S., Ramsbotham, W., Cliff, R.A., and Rex, D.C., 1996, Metamorphic evolution of the Sesia-Lanzo Zone, Western Alps: Time constraints from multi-system geochronology: Contributions to Mineralogy and Petrology, v. 126, p. 152-168. https://doi.org/10.1007/s004100050241.

Ji, W.Q., Malusà, M.G., Tiepolo, M., Langone, A., Zhao, L., and Wu, F.Y., 2019, Synchronous Periadriatic magmatism in the Western and Central Alps in the absence of slab breakoff: Terra Nova, v. 31 (2), p. 120-128. https://doi.org/10.1111/ter.12377.

Kaneko, Y., and Miyano, T., 2004, Recalibration of mutually consistent garnet–biotite and garnet–cordierite geothermometers: Lithos, v. 73, p. 255-269. https://doi.org/10.1016/j.lithos.2003.12.009.

Kapferer, N., Mercolli, I., and Berger, A., 2011, The composition and evolution of an Oligocene regolith on top of the Sesia-Lanzo Zone (Western Alps): International Journal of Earth Sciences (Geologische Rundschau), v. 100, p. 1115-1127. https://doi.org/10.1007/s00531-010-0637-8.

Kapferer, N., Mercolli, I., Berger, A., Ovtcharova, M., and Fügenschuh B., 2012, Dating emplacement and evolution of the orogenic magmatism in the internal Western Alps: 2. The Biella Volcanic Suite: Swiss Journal of Geosciences, v. 105, p. 67-84. https://doi.org/10.1007/s00015-012-0092-6.

Kokandakar, G.J., Ghodke, S.S., Rathna, K., More, L.B., Nagaraju, B., Bhosle, M.V., and Vijaya Kumar, K., 2018, Density, Viscosity and Velocity (Ascent Rate) of Alkaline Magmas: Journal of the Geological Society of India, v. 91, p. 135–146. https://doi.org/10.1007/s12594-018-0827-8.

Kroll, H., Evangelakakis, C., and Voll, G., 1993, Two-feldspar geothermometry: a review and revision for slowly cooled rocks: Contributions to Mineralogy and Petrology, v. 114, p. 510-518. https://doi.org/10.1007/BF00321755.

Lanza, R., 1977, Palaeomagnetic data from the andesitic and lamprophyric dykes of the Sesia-Lanzo Zone (Western Alps): Schweizerische Mineralogische und Petrographische Mitteilungen, v. 57, p. 281-290.

Lanza, R., 1978, Palaeomagnetic data on the andesitic cover of the Sesia-Lanzo Zone; Western Alps: Geologische Rundschau, v. 68 (1), p. 83-92. https://doi.org/10.1007/BF01821123.

Lardeaux, J.-M., 2014, Deciphering orogeny: A metamorphic perspective. Examples from European Alpine and Variscan belts part I: Alpine metamorphism in the Western Alps. A review: Bulletin de la Société Géologique de France, v. 185 (2), p. 93-114.

Lardeaux, J.-M., and Spalla, M.I., 1991, From granulites to eclogites in the Sesia zone (Italian Western Alps): A record of the opening and closure of the Piedmont ocean: Journal of Metamorphic Geology, v. 9, p. 35-59. https://doi.org/10.1111/j.1525-1314.1991.tb00503.x.

Lajaunie, C., Courrioux, G., and Manuel, L., 1997, Foliation fields and 3D cartography in geology: Principles of a method based on potential interpolation: Mathematical Geology, v. 29, p. 571-584. https://doi.org/10.1007/BF02775087.

Leake, B.E., Woolley, A.R., Arps, C.E.S., Birch, W.D., Gilbert, M.C., Grice, J.D., Hawthorne, F.C., Kato, A., Kisch, H.J., Krivovichev, V.G., Linthout, K., Laird, J., Mandarino, J.A., Maresch, W.V., Nickel, E.H., Rock, N.M.S., Schumacher, J.C., Smith, D.C., Stephenson, N.C.N., Ungaretti, L., Whittaker, E.J.W., and Guo, Y., 1997, Nomenclature of amphiboles, Report of the Subcommittee on Amphiboles of the International Mineralogical Association, Commission on New Minerals and Mineral Names: American Mineralogist, v. 82, p. 1019-1037.

Lesher, C.M., 2017, Roles of xenomelts, xenoliths, xenocrysts, xenovolatiles, residues, and skarns in the genesis, transport, and localization of magmatic Fe-Ni-Cu-PGE sulfides and chromite: Ore Geology Reviews, v. 90, p. 465-484. https://doi.org/10.1016/j.oregeorev.2017.08.008.

Levine, T., 2009, Using colour in figures: let's agree to differ: Traffic, v. 10, p. 344-347. doi: 10.1111/j.1600-0854.2008.00863.x.

Locock, A.J., 2014, An Excel spreadsheet to classify chemical analyses of amphiboles following the IMA 2012 recommendations: Computers & Geosciences, v. 62, p. 1-11. https://doi.org/10.1016/j.cageo.2013.09.011.

Lu, G.Y., and Wong, D.W., 2008, An adaptive inverse-distance weighting spatial interpolation technique: Computers & Geosciences, v. 34, p. 1044-1055. https://doi.org/10.1016/j.cageo.2007.07.010.

Lustrino, M., Duggen, S., and Rosenberg, C.L., 2011, The Central-Western Mediterranean: Anomalous igneous activity in an anomalous collisional tectonic setting: Earth-Science Reviews, v. 104 (1-3), p. 1-40. https://doi.org/10.1016/j.earscirev.2010.08.002.

Maxelon, M., Renard, P., Courrioux, G., Brändli, M., and Mancktelow, N., 2009, A workflow to facilitate three-dimensional geometrical modelling of complex poly-deformed geological units: Computers & Geosciences, v. 35, p. 644-658. https://doi.org/10.1016/j.cageo.2008.06.005.

McInerney, P., and Guillen, A., 2005, Building 3D geological models directly from the data? A new approach applied to Broken Hill, Australia: Digital Mapping Techniques, v. 05, p. 119-130.

Malaroda, R., Bortolami, G., Carraro, F., Friz, C., Govi, M., and Sacchi, R., 1966, Carta Geologica d'Italia, Foglio 43, ''Biella'' 1:100,000 (2nd ed.). Roma, Servizio Geologico d'Italia.

Michel, J., Baumgartner, L., Putliz, B., Schaltegger, U., and Ovtcharova, M., 2008, Incremental growth of the Patagonian Torres del Paine laccolith over 90 k.y.: Geology, v. 36 (6), p. 459-462. https://doi.org/10.1130/G24546A.1.

Molina, J.F., Moreno, J.A., Castro, A., Rodríguez, C., and Fershtater, G.B., 2015, Calcic amphibole thermobarometry in metamorphic and igneous rocks: New calibrations based on plagioclase/amphibole Al-Si partitioning and amphibole/liquid Mg partitioning: Lithos, v. 232, p. 286-305. https://doi.org/10.1016/j.lithos.2015.06.027.

Morimoto, N., 1988, Nomenclature of pyroxenes: American Mineralogist, v. 73, p. 1123-1133. https://doi.org/10.1007/BF01226262.

Mutch, E.J.F., Blundy, J.D., Tattitch, B.C., Cooper, F.J., and Brooker, R.A., 2016, An experimental study of amphibole stability in low-pressure granitic magmas and a revised Al-in-hornblende geobarometer: Contributions to Mineralogy and Petrology, v. 171, 85. https://doi.org/10.1007/s00410-016-1298-9.

Nachit, H., Ibhi, A., El Abia, H., and Ben Ohoud, M., 2005, Discrimination between primary magmatic biotites, reequilibrated biotites and neoformed biotites: Comptes Rendus Geoscience, v. 337, p. 1415-1420. https://doi.org/10.1016/j.crte.2005.09.002.

Nandedkar, R.H., Ulmer, P., and Müntener, O., 2016, Fractional crystallization of primitive, hydrous arc magmas: an experimental study at 0.7 GPa: Contributions to Mineralogy and Petrology, v. 167:1015. DOI 10.1007/s00410-014-1015-5.

Needy, S.K., Anderson, J.L., Wooden, J.L., Fleck, R.J., Barth, A.P., Paterson, S.R., Memeti, V., and Pignotta, G.S., 2009, Mesozoic magmatism in an upper- to middle-crustal section through the Cordilleran continental margin arc, eastern Transverse Ranges, California, *in* Miller, R.B., and Snoke, A.W., eds., Crustal cross sections from the western North American Cordillera and elsewhere: Implications for tectonic and petrologic processes: Geological Society of America Special Papers, v. 456, p. 187-218. https://doi.org/10.1130/2009.2456(07).

Neubauer, F., Heberer, B., Dunkl, I., Liu, X., Bernroider, M., and Dong, Y., 2018, The Oligocene Reifnitz tonalite (Austria) and its host rocks: implications for Cretaceous and Oligocene-Neogene tectonics of the south-eastern Eastern Alps: Geologica Carpathica, v. 69 (3), p. 237-253. https://doi.org/10.1515/geoca-2018-0014.

Oberli, F., Meier, M., Berger, A., Rosenberg, C.L., and Gieré, R., 2004, U-Th-Pb and $^{230}Th/^{238}U$ disequilibrium isotope systematics: Precise accessory mineral chronology and melt evolution tracing in the Alpine Bergell intrusion: Geochimica et Cosmochimica Acta, v. 68 (11), p. 2543-2560. https://doi.org/10.1016/j.gca.2003.10.017.

Pagliani Peyronel, G., 1959, Il granito porfirico della media Valle del Cervo (Biella): Rendiconti dell'Istituto Lombardo di Scienze e Lettere, v. 93, p. 379-398.

Pamić, J., and Palinkaš, L., 2000, Petrology and geochemistry of Paleogene tonalites from the easternmost parts of the Periadriatic Zone: Mineralogy and Petrology, v. 70, p. 121-141. https://doi.org/10.1007/s007100070017.

Parry W.T., and Downey L.M., 1982, Geochemistry of hydrothermal chlorite replacing igneous biotite: Clays Clay Minerals, v. 30 (2), p. 81-90. https://doi.org/10.1346/CCMN.1982.0300201.

Passchier, C.W., Urai, J.L., Van Loon, J., and Willimas, P.F., 1981, Structural geology of the Central Sesia-Lanzo Zone: Geologie en Mijnbouw, v. 60, p. 497-507.

Paterson, S.R., Fowler, T.K., Schmidt, K.L., Yoshinobu, A.S., Yuan, E.S., and Miller, R.B., 1998, Interpreting magmatic fabric patterns in plutons: Lithos, v. 44, p. 53-82. https://doi.org/10.1016/S0024-4937(98)00022-X.

Peccerillo, A., and Martinotti, G., 2006, The Western Mediterranean lamproitic magmatism: origin and geodynamic significance: Terra Nova, v. 18, p. 109-117. https://doi.org/10.1111/j.1365-3121.2006.00670.x.

Petford, N., 2003, Rheology of granitic magmas during ascent and emplacement: Annual Review of Earth and Planetary Sciences, v. 31, p. 399-427. doi: 10.1146/annurev.earth.31.100901.141352.

Petford, N., Cruden, A.R., McCaffrey, K.J.W., and Vigneresse, J.L., 2000, Granite magma formation, transport and emplacement in the Earth's crust: Nature, v. 408, p. 669-673. https://doi.org/10.1038/35047000.

Perchuk, L.L., Aranovich, L.Y., Podlesskii, K.K., Lavrent'eva, I.V., Gerasimov, V.Y., Fed'Kin, V.V., Kitsul, V.I., Karasakov, L.P., and Berdnikov, N.V., v. 1985, Precambrian granulites of the Aldan shield eastern Siberia, USSR: Journal of Metamorphic Geology, v. 3, p. 265-310.

Piwinskii, A.J., 1968, Experimental studies of igneous rock series central Sierra Nevada batholith, California: Journal of Geology, v. 76, p. 548-870. https://doi.org/10.1086/627359.

Pognante, U., Talarico, F., Rastelli, N., and Ferrati, N., 1987, High pressure metamorphism in the nappes of the Valle dell'Orco traverse (Western Alps Collisional Belt): Journal of Metamorphic Geology, v. 5, p. 397-414. https://doi.org/10.1111/j.1525-1314.1987.tb00392.x.

Powell, R., and Holland, T.J.B., 1994, Optimal geothermometry and geobarometry: American Mineralogist, v. 70, p. 120-133.

Pryer, L.L., and Robin, P.Y.F., 1995, Retrograde metamorphic reactions in deforming granites and the origin of flame perthite: Journal of Metamorphic Geology, v. 13, p. 645-658. https://doi.org/10.1111/j.1525-1314.1995.tb00249.x.

Putirka, K.D., 2016, Amphibole thermometers and barometers for igneous systems and some implications for eruption mechanisms of felsic magmas at arc volcanoes: American Mineralogist, v. 101, p. 841-858. https://doi.org/10.2138/am-2016-5506.

Rahn, M., Wang, H., and Dunkl, I., 2019, A natural long-term annealing experiment for the zircon fission track system in the Songpan-Garzê flysch, China: Terra Nova, v. 31, p. 295-305. DOI: 10.1111/ter.12399.

Regis, D., Rubatto, D., Darling, J., Cenki-Tok, B., Zucali, M., and Engi, M., 2014, Multiple metamorphic stages within an eclogite facies terrane (Sesia Zone, Western Alps) revealed by U/Th-Pb petrochronology: Journal of Petrology, v. 55 (7), p.1429-1456. https://doi.org/10.1093/petrology/egu029.

Roda, M., Spalla, M.I., and Marotta, A.M., 2012, Integration of natural data within a numerical model of ablative subduction: a possible interpretation for the Alpine dynamics of the Austroalpine crust: Journal of Metamorphic Geology, v. 30, p. 973-996, doi: 10.1111/jmg.12000.

Roda, M., De Salvo, F., Zucali, M., and Spalla, M.I., 2018, Structural and metamorphic evolution during tectonic mixing: is the Rocca Canavese Thrust Sheet (Italian Western Alps) a subduction-related mélange? Italian Journal of Geosciences, v. 137, p. 311-329, doi: 10.3301/IJG.2018.17.

Roda, M., Zucali, M., Regorda, A., and Spalla, M.I., 2020, Formation and evolution of a subduction-related mélange: The example of the Rocca Canavese Thrust Sheets (Western Alps): GSA Bulletin, v. 132, p. 884-896, doi: 10.1130/B35213.1.

Romer, R.L., Schärer, U., and Steck, A., 1996, Alpine and pre-Alpine magmatism in the root-zone of the Western Central Alps: Contributions to Mineralogy and Petrology, v. 123, p. 138-158. https://doi.org/10.1007/s004100050147.

Rosenberg, C.L., 2004, Shear zones and magma ascent: A model based on a review of the Tertiary magmatism in the Alps: Tectonics, v. 23, TC3002. https://doi.org/10.1029/2003TC001526.

Rosenberg, C.L., and Handy, M.R., 2005, Experimental deformation of partially melted granite revisited; implications for the continental crust: Journal of Metamorphic Geology, v. 23, p. 19-28. https://doi.org/10.1111/j.1525-1314.2005.00555.x.

Rossetti, P., Agangi, A., Castelli, D., Padoan, M., and Ruffini, R., 2007, The Oligocene Biella pluton (Italian Western Alps): New insight on the magmatic vs. hydrothermal activity in the Valsessera roof zone: Periodico di Mineralogia, v. 76, p. 223-240.

Rubatto, D., Regis, D., Hermann, J., Boston, K., Engi, M., Beltrando, M., and McAlpine, S.R.B., 2011, Yo-yo subduction recorded by accessory minerals in the Italian Western Alps: Nature Geoscience, v. 4, p. 338-342. https://doi.org/10.1038/ngeo1124.

Schaltegger, U., Nowak, A., Ulianov, A., Fisher, C.M., Gerdes, A., Spikings, R., Whitehouse, M.J., Bindeman, I., Hanchar, J.M., Duff, J., Vervoort, J.D., Sheldrake, T., Caricchi, L., Brack, P., and Müntener, O., 2019, Zircon petrochronology and $^{40}Ar/^{39}Ar$ thermochronology of the Adamello Intrusive Suite, N. Italy: Monitoring the growth and decay of an incrementally assembled magmatic system: Journal of Petrology, v. 60 (4), p. 701-722. https://doi.org/10.1093/petrology/egz010.

Scheuring, B., Ahrendt, H., Hunziker, J.C., and Zingg, A., 1973, Paleobotanical and geochronological evidence for the Alpine age of the metamorphism in the Sesia-Zone: Geologische Rundschau, v. 63, p. 305-326.

Schmid, S.M., Aebli, H.R., Heller, F., and Zingg, A., 1989, The role of the Periadriatic line in the tectonic evolution of the Alps, *in* Dietrich, D., and Coward, M.P., eds., Alpine tectonics: Geological Society London Special Publications, v. 45, p. 153-171.

Schmidt, M.W., 1992, Amphibole composition in tonalite as a function of pressure: an experimental calibration of the Al-in-hornblende barometer: Contributions to Mineralogy and Petrology, v. 110, p. 304-310. https://doi.org/10.1007/BF00310745.

Schmidt, M.W., 1993, Phase relations and compositions in tonalite as a function of pressure: an experimental study at 650°C: American Journal of Science, v. 293, p. 1011-1060. doi:10.2475/ajs.293.10.1011.

Smith, D.J., 2014, Clinopyroxene precursors to amphibole sponge in arc crust: Nature Communications, v. 5, 4329. doi: 10.1038/ncomms5329.

Spalla, M.I., Lardeaux, J.-M., Dal Piaz, G.V., Gosso, G., and Messiga, B., 1996, Tectonic significance of Alpine eclogites: Journal of Geodynamics, v. 21, p. 257-285. https://doi.org/10.1016/0264-3707(95)00033-X.

Spalla, M.I., and Zulbati, F., 2003, Structural and petrographic map of the southern Sesia-Lanzo zone (Monte Soglio - Rocca Canavese, western Alps, Italy): Memorie di Scienze Geologiche, Padova, v. 55, p. 119 -127.

Stern, C.R., Huang, W.L., and Wyllie, P.J., 1975, Basalt-andesite-rhyolite-H_2O: Crystallization intervals with excess H_2O and H_2O-undersaturated liquidus surfaces to 35 kilo bars, with implications for magma genesis: Earth and Planetary Science Letters, v. 28 (2), p. 189-196. https://doi.org/10.1016/0012-821X(75)90226-5.

Stipp, M., Fügenschuh, B., Gromet, L.P., Stünitz, H., and Schmid, S.M., 2004, Contemporaneous plutonism and strike-slip faulting along the easternmost segment of the Insubric line: The Tonale fault zone north of the Adamello pluton (Italian Alps): Tectonics, v. 23, TC3004. https://doi.org/10.1029/2003TC001515.

Sun, P., Niu, Y., Guo, P., Cui, H., Ye, L., and Liu, J., 2018, The evolution and ascent paths of mantle xenolith-bearing magma: Observations and insights from Cenozoic basalts in Southeast China: Lithos, v. 310–311, p. 171–181. doi:10.1016/j.lithos.2018.04.015.

Tagami, T., and Matsu'ura S., 2019, Thermal annealing characteristics of fission tracks in natural zircons of different ages. Terra Nova, v. 31, p. 257-262. DOI: 10.1111/ter.12394.

Thornton, J.M., Mariethoz, G., and Brunner, P., 2018, A 3D geological model of a structurally complex Alpine region as a basis for interdisciplinary research: Scientific Data, v. 5 (1), p. 1-20. https://doi.org/10.1038/sdata.2018.238.

Tornare, E., Pilet, S., and Bussy, F., 2016, Magma Differentiation in Vertical Conduits Revealed by the Complementary Study of Plutonic and Volcanic Rocks from

Fuerteventura (Canary Islands): Journal of Petrology, v. 57 (11&12), p. 2221–2250. doi: 10.1093/petrology/egx004.

Trajanova, M., Pécskay, Z., and Itaya, T., 2008, K-Ar geochronology and petrography of the Miocene Pohorje Mountains batholith (Slovenia): Geologica Carpathica, v. 59 (3), p. 247-260.

Vernon, R.H., 2000, Review of microstructural evidence of magmatic and solid-state flow: Visual Geosciences, v. 5, 1-23. https://doi.org/10.1007/s10069-000-0002-3.

Vernon, R.H., 2004, A practical guide to rock microstructure, Cambridge University Press. https://doi.org/10.1017/9781108654609.

Vielzeuf D., 1983, The spinel and quartz association in high grade xenoliths from Tallante (SE Spain) and their potential use in geothermobarometry and barometry: Contributions to Mineralogy and Petrology, v. 82, p. 301-311.

Vilà, M., Fernández, M., and Jiménez-Munt, I., 2010, Radiogenic heat production variability of some common lithological groups and its significance to lithospheric thermal modeling: Tectonophysics, v. 490, p. 152-164. doi:10.1016/j.tecto.2010.05.003.

Von Blanckenburg, F., Früh-Green, G., Diethelm, K., and Stille, P., 1992, Nd-, Sr-, O-isotopic and chemical evidence for a two-stage contamination history of mantle magma in the Central-Alpine Bergell intrusion: Contributions to Mineralogy and Petrology, v. 110, p. 33-45. https://doi.org/10.1007/BF00310880.

Von Blanckenburg, F., Kagami, H., Deutsch, A., Oberli, F., Meier, M., Wiedenbeck, M., Barth, S., and Fischer, H., 1998, The origin of Alpine plutons along the Periadriatic Lineament: Schweizerische Mineralogische und Petrographische Mitteilungen, v. 78, p. 55-65.

Williams, M.L., and Grambling, J.A., 1990, Manganese, ferric iron, and the equilibrium between garnet and biotite: American Mineralogist, v. 75, p. 886-908.

Wu, C.M. 2019, Original calibration of a garnet geobarometer in metapelite: Minerals, v. 9, 540. doi:10.3390/min9090540.

Wu, C.M., Zhang, J., and Ren, L.D., 2004, Empirical garnet–biotite–plagioclase–quartz (GBPQ) geobarometry in medium to high-grade metapelites: Journal of Petrology, v. 45 (9), p. 1907-1921. https://doi.org/10.1093/petrology/egh038.

Yavuz, F., and Yıldırım, D.K., 2018, A Windows program for calculation and classification of epidote-supergroup minerals: Periodico di Mineralogia, v. 87, p. 269-285.

Yoshinobu, A.S, Fowler, T.K.Jr., Paterson, S.R., Llambias, E., Tickyj, H., and Sato A.M., 2003, A view from the roof: magmatic stoping in the shallow crust, Chita pluton, Argentina: Journal of Structural Geology, v. 25, p. 1037-1048. https://doi.org/10.1016/S0191-8141(02)00149-9.

Zanoni, D., 2010, Structural and petrographic analysis at the north-eastern margin of the Oligocene Traversella pluton (Internal Western Alps, Italy): Italian Journal of Geosciences, v. 129, p. 51-68. https://doi.org/10.3301/IJG.2009.04.

Zanoni, D., 2016, Structure and petrography of the southwestern margin of the Biella pluton, Western Alps: Journal of Maps, v. 12 (3), p. 597-620. https://doi.org/10.1080/17445647.2015.1056259.

Zanoni, D., Bado, L., Spalla, M.I., Zucali, M., and Gosso, G., 2008, Structural analysis of the northeastern margin of the Tertiary intrusive stock of Biella (Western Alps, Italy): Italian Journal of Geosciences, v. 127, p. 125-140.

Zanoni, D., Spalla, M.I., and Gosso, G., 2010, Structure and PT estimates across late-collisional plutons: constraints on the exhumation of western Alpine continental HP units: International Geology Review, v. 52 (10), p. 1244-1267. https://doi.org/10.1080/00206814.2010.482357.

Zingg, A., and Hunziker, J.C., 1990, The age of movements along the Insubric Line West of Locarno (northern Italy and southern Switzerland): Eclogae Geologicae Helvetiae, v. 83 (3), p. 629-644.

Zingg, A., Hunziker, J.C., Frei, M., and Ahrendt, H., 1976, Age and degree of metamorphism of the Canavese Zone of the sedimentary cover of the Sesia Zone: Schweizerische Mineralogische und Petrographische Mitteilungen, v. 56, p. 361-375.

Zucali, M., Corti, L., Delleani, F., Zanoni, D., and Spalla, M.I., 2020, 3D reconstruction of fabric and metamorphic domains in a slice of continental crust involved in the Alpine subduction system: the example of Mt. Mucrone (Sesia-Lanzo Zone, Western Alps): International Journal of Earth Sciences, v. 109 (4), p. 1337-1354. https://doi.org/10.1007/s00531-019-01807-6.

Zucali, M., Spalla, M.I., and Gosso, G., 2002, Strain partitioning and fabric evolution as a correlation tool: The example of the Eclogitic Micaschists complex in the Sesia-Lanzo Zone (Monte Mucrone-Monte Mars, Western Alps, Italy): Schweizerische Mineralogische und Petrographische Mitteilungen, v. 82, p. 429-454.

Zuffetti, C., Comunian, A., Bersezio, R., and Renard, P., 2020, A new perspective to model subsurface stratigraphy in alluvial hydrogeological basins, introducing geological hierarchy and relative chronology: Computers & Geosciences, v. 140. https://doi.org/10.1016/j.cageo.2020.104506.

Figure captions

Figure 1. (a) Simplified tectonic sketch map of the Alps; the main Periadriatic plutons are represented: T = Traversella; B = Biella; M = Miagliano; Br = Bergell; A = Adamello; Rn = Rensen; Rs = Rieserferner; K = Karawanken; P = Pohorje; thin black lines represent country borders (codes from ISO = International Organization for Standardization) around the Alps; (b) geological sketch map of the Sesia-Lanzo Zone (modified after Compagnoni *et al.* 1977; Passchier *et al.* 1981; Spalla and Zulbati 2003; Zanoni *et al.* 2010; Zanoni 2016); DM = dominant metamorphism; HT = high temperature; HP = high pressure; LT-LP = low temperature – low pressure.

Figure 2. Sketch map of the Biella pluton (modified after De Capitani *et al.* 1979; Bigioggero *et al.* 1994; Zanoni *et al.* 2008; Zanoni 2016). 100 m-spaced contour elevation lines are from Piemonte regional administration cartographic facility. The trace of the cross sections in Figure 3 is indicated.

Figure 3. Cross-sections throughout the pluton margin and located in Figure 2. Structural data used to interpret the cross-sections and trajectories of planar structures are from Zanoni *et al.* (2008) and Zanoni (2016). Details on rock types in cross section A-A' and B-B' are in Zanoni *et al.* (2008), and C-C' and D-D' in Zanoni (2016), as well as details on mapped and interpreted country rock boundaries. Lower hemisphere equal areal pole-to-plane projections (plotted with Openstero, Grohmann *et al.*, 2011) for magmatic foliation are represented by red density plots and for contact surface of pluton and country rocks by black dots. Data are separated for the northwestern, southwestern, southeastern, and northeastern areas (n = number of data).

Figure 4. (a) Fault zone in Val Sessera across plutonic and country rocks mineralized with Fe-carbonate (reddish aloe) associated with tourmaline; (b) looking westward, M. Tovo with decameter-thick cataclastic band (red) across the pluton (green) and country rocks (pale blue); dashed lines indicate close-up ridgelines and solid lines indicate contact of plutonic and country rocks; (c) decimeter-sized country rock xenolith in monzonite between Oropa and Riabella; the longest side is parallel to the regional foliation still well visible in xenolith, which is penetrated by magmatic veins mostly along xenolith foliation.

Figure 5. QPF classification diagram that shows composition on the basis of mineral modal amount determined at the optical microscope, in comparison with data from Cesana *et al.* (1976).

Figure 6. Microstructure and microtexture in igneous rocks; (a) magmatic foliation marked by Kfs (K-feldspar) and Pl_1 (plagioclase 1), and Amp_1 (amphibole 1), sample 59A, crossed polars; (b) shape preferred orientation of Kfs (K-feldspar) and Pl_1 (plagioclase 1) defining magmatic foliation. Kfs (K-feldspar) shows Carlsbad twinning and growth zoning, and contains $Pl_{pre\text{-}1}$ (plagioclase pre-1), which shows irregular rims

overgrown by Pl_{1a} (plagioclase 1a; white rim). Pl_{pre-1} (plagioclase pre-1) is partially replaced by Ep (epidote) aggregate (high birefringence); sample 3130105; crossed polars; (c) myrmekites at the grain boundary of two Kfs (K-feldspar) crystals. Kfs (K-feldspar) contains flame perthites; sample BPA10; crossed polars; (d) Kfs (K-feldspar), Pl_1 (plagioclase 1), and minor Amp_1 (amphibole 1) marking the magmatic foliation; Amp_1 (amphibole 1) forms a single crystal that is both parallel to the magmatic foliation and interstitial between Kfs (K-feldspar) and Pl_1 (plagioclase 1); a side content of Al and Ti (apfu) are shows for three points (see next section for details): yellow = Amp_{1a} (amphibole 1a, core); red = Amp_{1b} (amphibole 1b, rim); pink = Amp_{1b} (amphibole 1b, interstitial); sample 3130105; crossed polars; (e) Cpx (clinopyroxene, grey) partially replaced by Amp_{1a} (amphibole 1a, yellow); magmatic foliation wraps Cpx (clinopyroxene); sample 59A; crossed polars; (f) Amp_{1b} (amphibole 1b) interstitial between euhedral Pl_1 (plagioclase 1) and Bt (biotite), and rounded Qz crystals; sample 59A; crossed polars; (g) magmatic foliation in mafic monzonite marked by shape preferred orientation of euhedral Bt (biotite); Amp_1 (amphibole 1) is mostly interstitial but elongate parallel to the foliation; sample BPA4; plane polarized light; (h) Kfs (K-feldspar) enclosing Pl_{pre-1} (plagioclase pre-1) with irregular rims overgrown by Pl_{1a} (plagioclase 1a); sample BPA4; crossed polars.

Figure 7. (a) BSE image of Amp_2 (amphibole 2, dark grey) patchy overgrowth on Amp_1 (amphibole 1, light grey), amphibole encloses euhedral Ap (apatite) and Mgt (magnetite); sample BPB1; (b) Pl (plagioclase) partially replaced by fine grained aggregates mostly of Ep (epidote); Bt (biotite) rimmed by Chl (chlorite) and Ep (epidote); sample BPB1, crossed polars.

Figure 8. (a) X_{Mg} vs. Si compositional diagram (Leake *et al.* 1997) and Ti vs. Al diagram for amphibole; (b) ternary diagram for feldspar.

Figure 9. Ternary compositional diagram for pyroxene. Grey field and open circles in the full diagram and close-up, respectively, represent the composition of clinopyroxene phenocrysts from shoshonitic andesite lavas (Callegari *et al.* 2004). Shoshonitic clinopyroxene formulae were calculated according to Morimoto (1988) to be compared and plotted with clinopyroxene from this work.

Figure 10. Binary classification diagram for titanite (Aleinikoff *et al.* 2002).

Figure 11. (a) Cooling path of the Biella pluton. Wet granite solidus (orange): dotted line (Holland and Powell 2001), dashed line (Stern *et al.* 1975). Wet granodiorite solidus (green solid line) (Piwinskii 1968). Wet tonalite solidus (blue): dotted line (Schmidt 1993), dashed line (Stern *et al.* 1975); pressure for myrmekite, perthite, and chlorite development are constrained from pressures estimated for Amp_2 in each sample; (b) Geological sketch of the Biella pluton with punctual distribution of temperatures and pressures estimated for igneous rocks and pressures estimated for contact metamorphism in country rocks (blue numbers in kbar); P-T values for magmatic rocks derive from the weighted average that includes all estimates for Amp_{1a} and Amp_{1b} in each sample and P values in host rocks derive from weighted average of all estimates for each sample; colours of P-T values for pluton plutonic rocks are the same as in Figures from 8 to 11a.

Figure 12. 3D geological model visualized through Paraview software. Volume: 110 km^3 divided into voxels with dimension of 50-50-15 m. The geological formations considered are EMC (Eclogitic Micaschists Complex, Sesia-Lanzo Zone) basement, monzonitic complex, syenitic-granitic complex, Southern Alps. The orientation of Periadriatic Line is from Schmid *et al.* (1989) and Handy *et al.* (2005).

Figure 13. 3D results of the Inverse distance weight interpolation starting from pressure point estimates (a: Amp_{1a}; b: Amp_{1b}) and from temperature point estimates (c: Amp_{1a}; d: Amp_{1b}). EMC (Eclogitic Micaschists Complex, Sesia-Lanzo Zone) basement = pale blue; Southern Alps = pale yellow; Syenitic-granitic complex = pink; Periadriatic Line = red.

Figure 14. Isobaric surfaces for Amp_{1b} in (a) 2-dimensions and in (b) 3-dimensions. The chosen isobaric surfaces are the classes' boundary from the IDW interpolations (Figure 11). The orientation data of all isobaric surfaces grouped in a stereonet with the mean orientation plane and the rotation axial pole. The enclosed table shows the surface orientation and post-intrusive rotation results. The syenitic-granitic complex, the monzonitic complex, the EMC (Eclogitic Micaschists Complex, Sesia-Lanzo Zone) basements, the Southern Alps, the Periadriatic Line, and the rock samples are shown.

Figure 15. Schematic representation of the magmatic and tectonic evolution of the andesite cover, Biella pluton, and country rocks (Cervo block) over Oligocene and Miocene. This interpretation is based on original data presented in this work and interpretations, data, and re-interpretation of data from the literature (Schmid *et al.* 1989; Zingg and Hunziker 1990; Biggiogero *et al.* 1994; Callegari *et al.* 2004; Zanoni *et al.* 2008, 2010; Berger *et al.* 2012a,b; Kapferer *et al.* 2011, 2012; Zanoni 2016). In any sketch, the present-day topographic profile of the Valle del Cervo axis is reported as a reference and the actual depths at which it is shown the pluton have to be referred to the altitude of palaeo-topography. (a) At about 32 Ma the Sesia-Lanzo Zone rocks were already exposed and fed the Rupelian basal conglomerate that was overlaid by high-K calc-alkaline andesitic lava flows from active volcanism; most likely the andesitic volcaniclastic cover was deposited also on the Ivrea Zone; (b) at about 31 Ma the high-K calc-alkaline volcanism was ongoing and the Biella monzonite emplaced and room

was facilitated by magmatic stopping in the roof and ductile deformation of the host rocks at the bottom; at this time the shoshonitic volcanism was fed by the monzonite reservoir itself and with the contribution of the ongoing high-K calc-alkaline volcanism the andesitic sequence possibly reached a thickness of 2.3 km; (c) at about 30 Ma the syenite intruded with subsequent differentiation of the pink and white granite; by this time possibly the volcanic activity was over; (d) between 30 and 26 Ma, the Cervo block rotated southeastward accompanied by a tectonic burial that took the bottom of the andesite sequence, approaching the Periadriatic Line, at a depth of 5 km; at the same time the Ivrea Zone could have been uplift with consequent complete erosion of the top cover; (e) between 26 and 18 Ma, the uplift of the Cervo block started with ongoing rotation and zircon fission tracks were recorded first in andesite and afterward in the Biella pluton; (f) between 18 and 12 Ma, the ongoing uplift and rotation of the Cervo block is responsible for apatite fission tracks in andesite and later in plutonic rocks; at the end of this time interval, possibly the rotation stopped; (g) present-day section of the Biella pluton and its country rocks along the Valle del Cervo axis; the reconstruction of the buried part of the pluton is facilitated by the 3D model, whereas the interpretation of the pluton boundaries at altitude higher than topography considers the geological boundaries on the slopes above the valley axis.

Figure 16. Inferred D (depth) – t (time) path of the Cervo block during Oligocene and Miocene. The D-t path is illustrated by means of three reference points, which were chosen at the base of the andesite cover, and at pluton roof and bottom. Symbols of the reference points are located in the sketches of Figure 15. Solid line = constrained path; dashed line = not constrained path. Depositional burial of andesite cover and pluton emplacement may be overlapped in time. The block uplift and rotation may keep going also after the Serravalian (i.e. after 12 Ma).

Table captions

Table 1. Summary of the textural relationships of minerals in monzonite that displays also the interpreted crystallization sequence and the late to post magmatic mineral growth.

Supplemental material

Supplemental File 1. Summary of chemical composition parameters of mineral generations in the different samples. Average and standard deviation, along with number of analyses are shown.

Supplemental File 2. Selected analyses for the subsequent mineral generations in different samples with full stoichiometric formulae.

Supplemental File 3. Summary of temperatures and pressures estimated for igneous rocks with average and standard deviation; n indicates the number of estimates.

Supplemental File 4. Summary of the pressure estimates (n = number of estimates) for the contact metamorphism in the country rocks, with mineral compositions and end-member activities. End-member activities are calculated with AX program. Cations are calculated on the following number of oxygen atoms: biotite (Bt) 22, plagioclase (Pl) 8, garnet (Gt) 12, cordierite (Crd) 18, spinel (Sp) 4. Abbreviations for end-members are from THERMOCALC list. AvPT = average PT calculation.

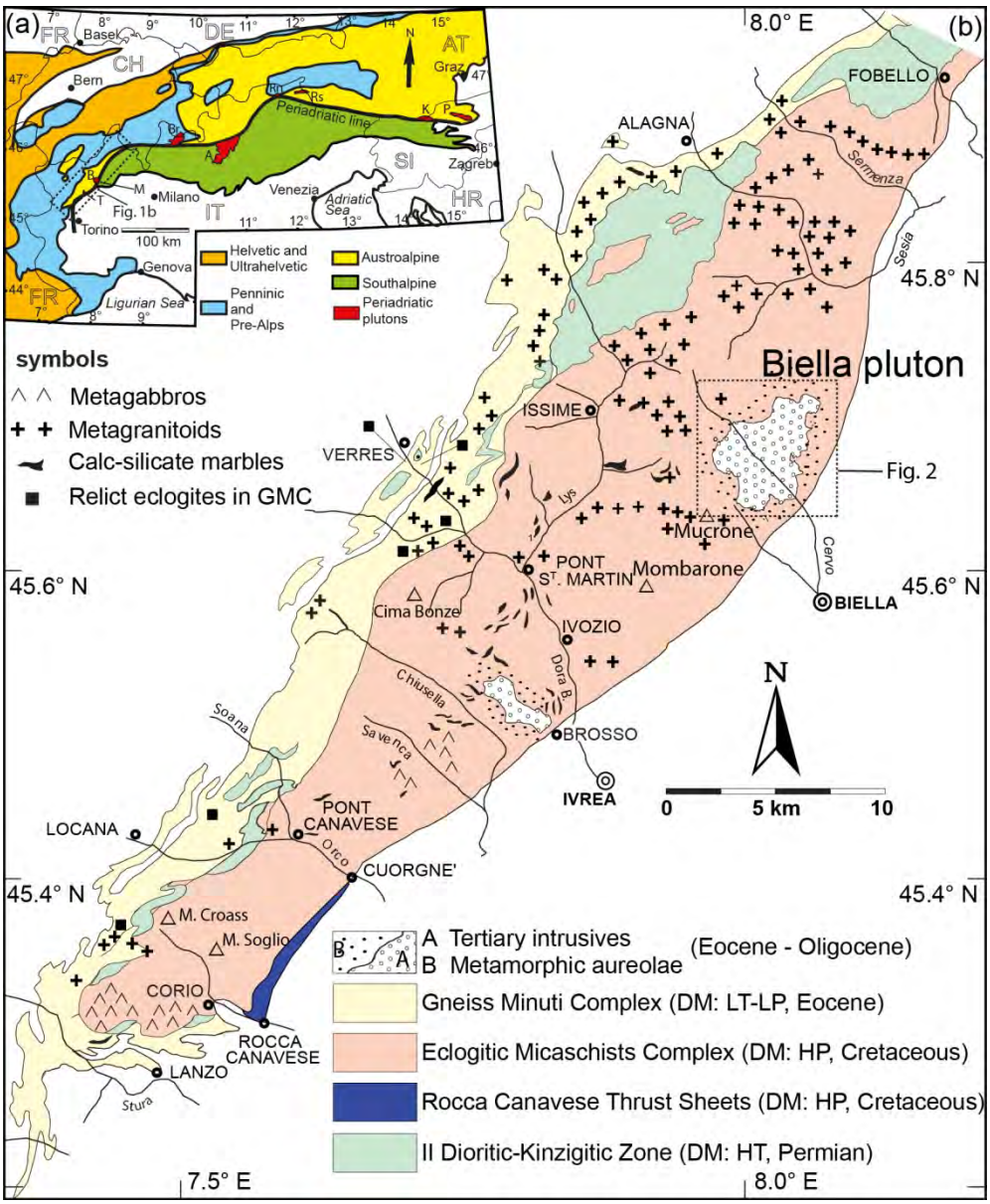

Figure 1. (a) Simplified tectonic sketch map of the Alps; the main Periadriatic plutons are represented: T = Traversella; B = Biella; M = Miagliano; Br = Bergell; A = Adamello; Rn = Rensen; Rs = Rieserferner; K = Karawanken; P = Pohorje; thin black lines represent country borders (codes from ISO = International Organization for Standardization) around the Alps; (b) geological sketch map of the Sesia-Lanzo Zone (modified after Compagnoni et al. 1977; Passchier et al. 1981; Spalla and Zulbati 2003; Zanoni et al. 2010; Zanoni 2016); DM = dominant metamorphism; HT = high temperature; HP = high pressure; LT-LP = low temperature – low pressure.

148x179mm (300 x 300 DPI)

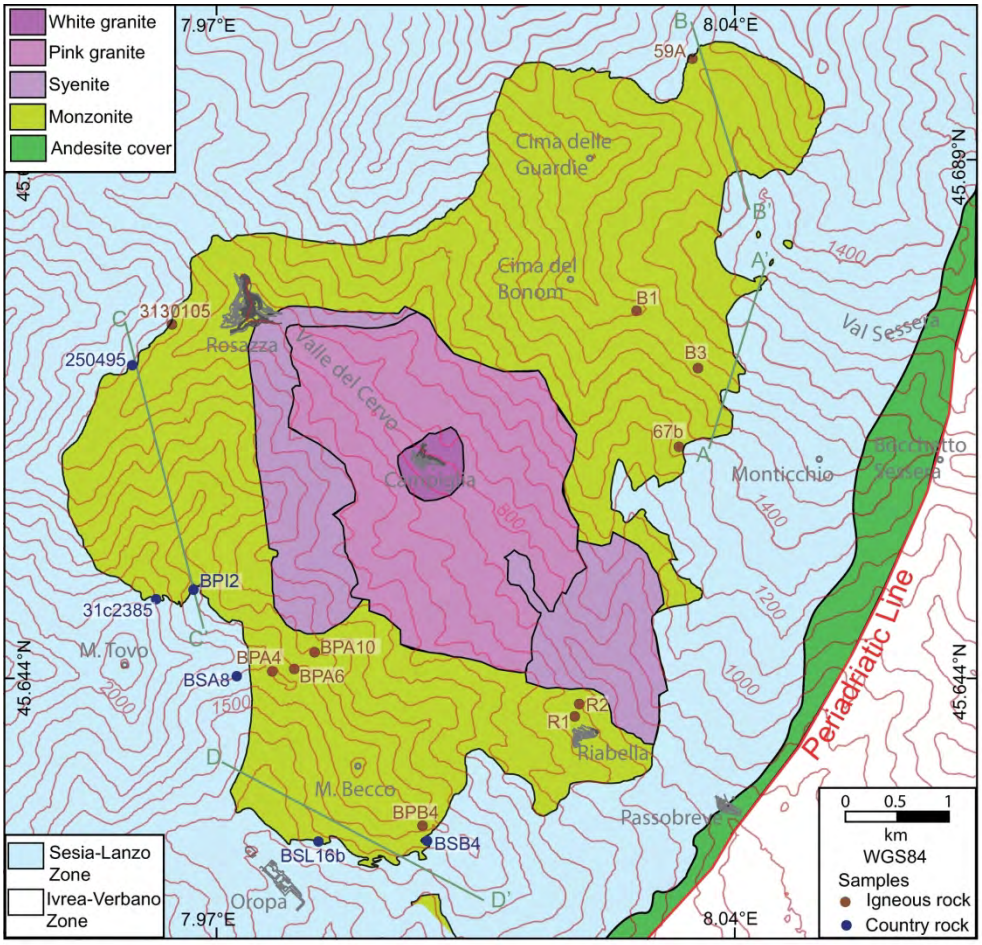

Figure 2. Sketch map of the Biella pluton (modified after De Capitani et al. 1979; Bigioggero et al. 1994; Zanoni et al. 2008; Zanoni 2016). 100 m-spaced contour elevation lines are from Piemonte regional administration cartographic facility. The trace of the cross sections in Figure 3 is indicated.

192x182mm (300 x 300 DPI)

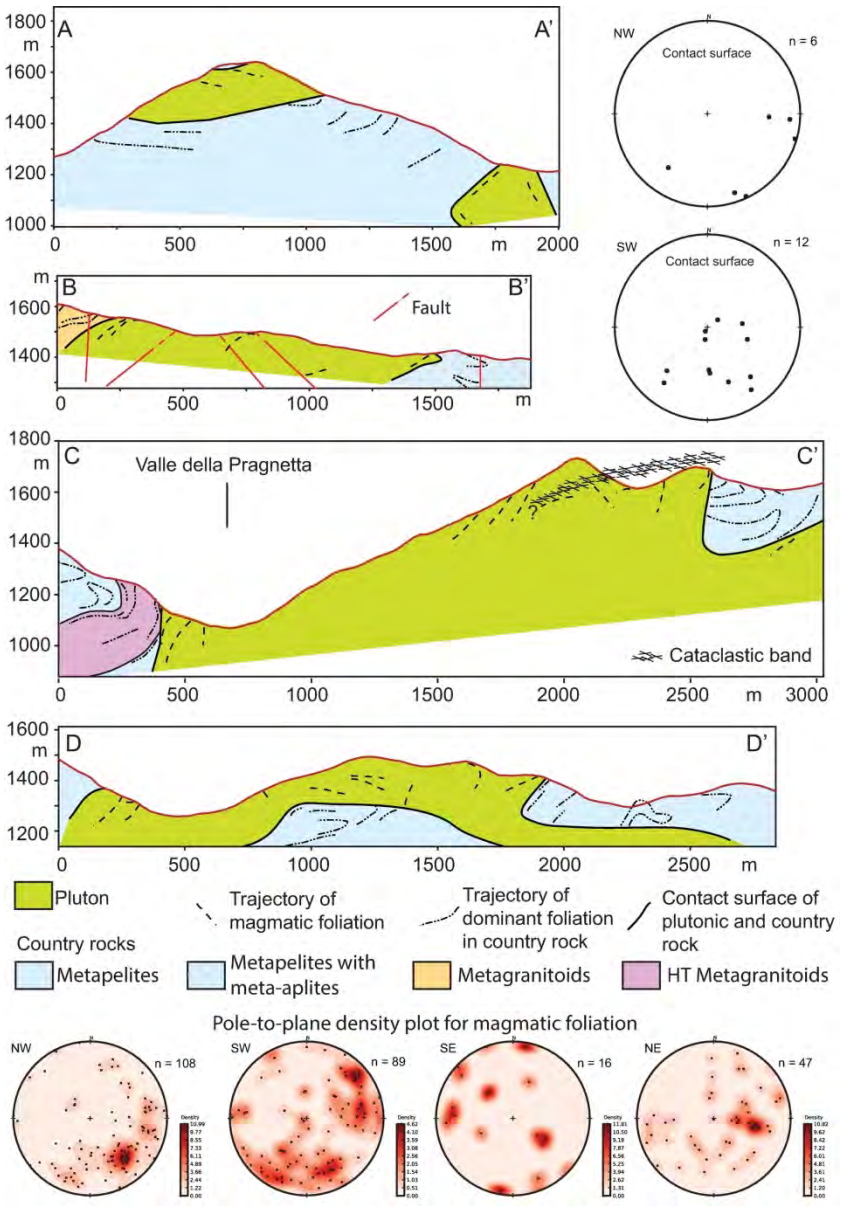

Figure 3. Cross-sections throughout the pluton margin and located in Figure 2. Structural data used to interpret the cross-sections and trajectories of planar structures are from Zanoni et al. (2008) and Zanoni (2016). Details on rock types in cross section A-A' and B-B' are in Zanoni et al. (2008), and C-C' and D-D' in Zanoni (2016), as well as details on mapped and interpreted country rock boundaries. Lower hemisphere equal areal pole-to-plane projections (plotted with Openstero, Grohmann et al., 2011) for magmatic foliation are represented by red density plots and for contact surface of pluton and country rocks by black dots. Data are separated for the northwestern, southwestern, southeastern, and northeastern areas (n = number of data).

168x241mm (300 x 300 DPI)

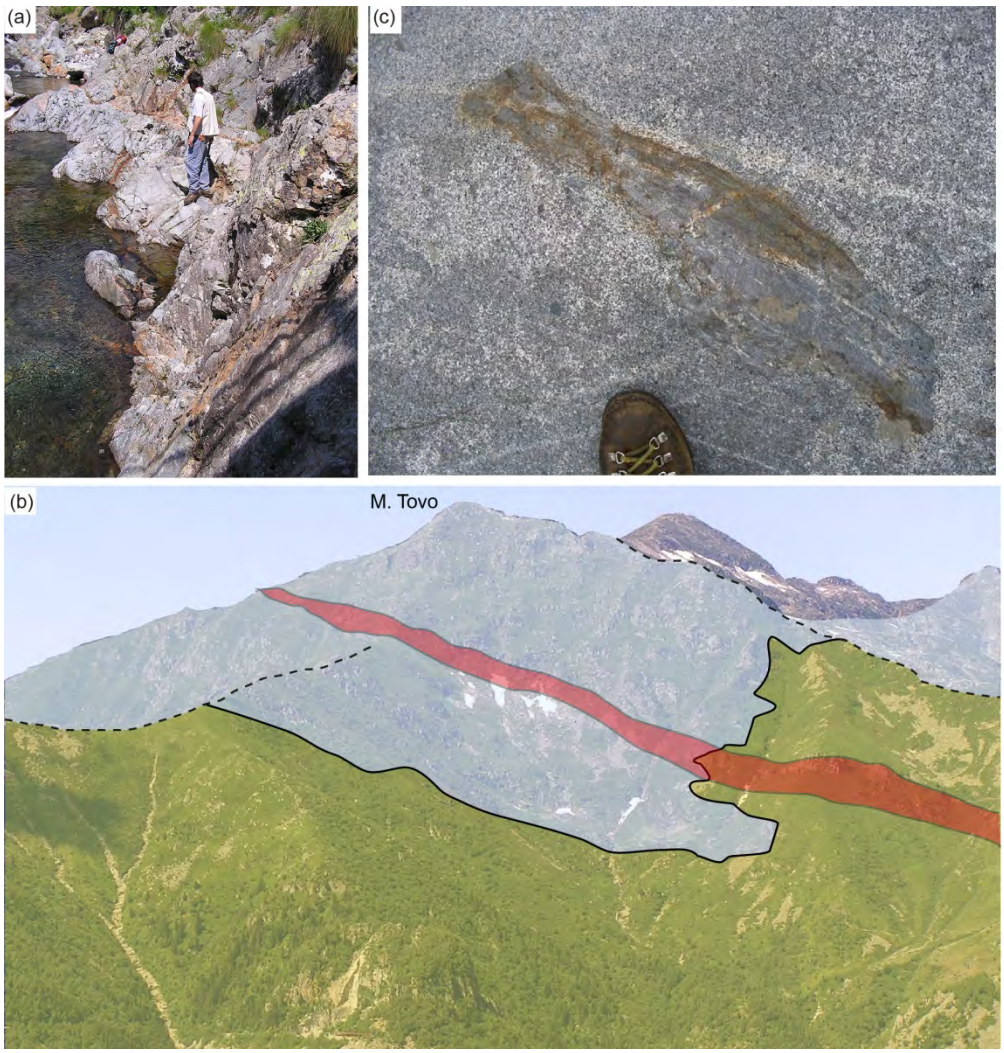

Figure 4. (a) Fault zone in Val Sessera across plutonic and country rocks mineralized with Fe-carbonate (reddish aloe) associated with tourmaline; (b) looking westward, M. Tovo with decameter-thick cataclastic band (red) across the pluton (green) and country rocks (pale blue); dashed lines indicate close-up ridgelines and solid lines indicate contact of plutonic and country rocks; (c) decimeter-sized country rock xenolith in monzonite between Oropa and Riabella; the longest side is parallel to the regional foliation still well visible in xenolith, which is penetrated by magmatic veins mostly along xenolith foliation.

180x187mm (300 x 300 DPI)

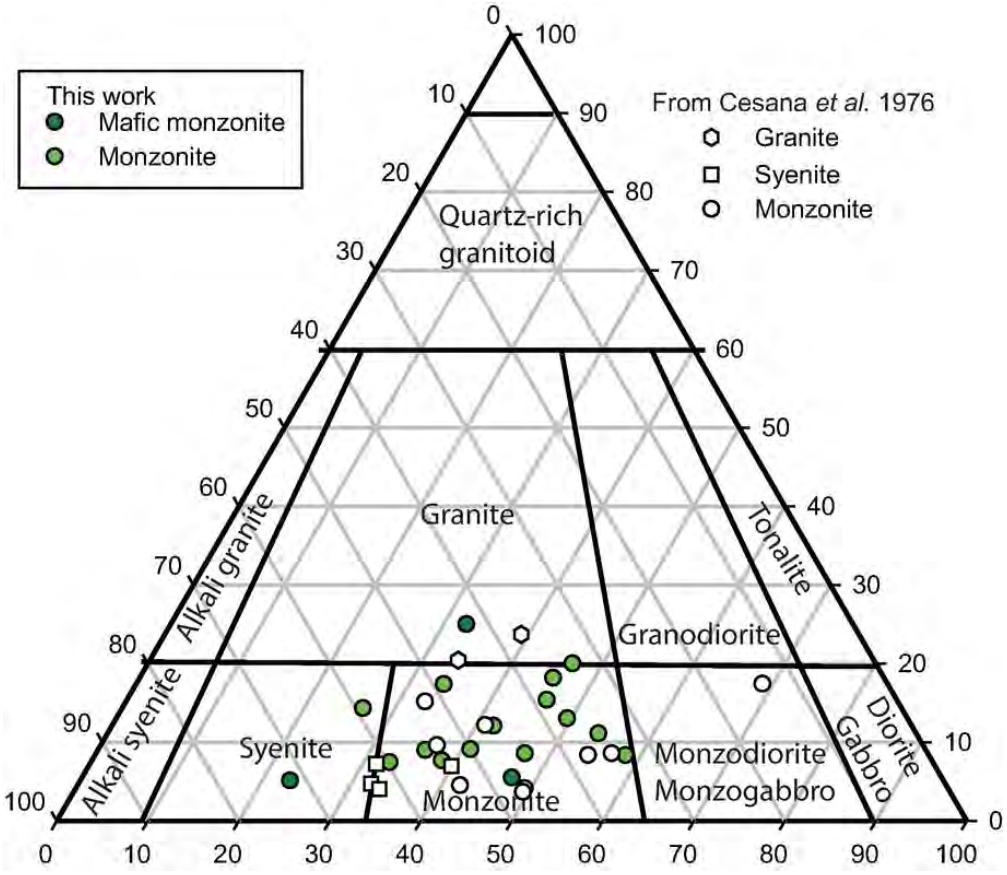

Figure 5. QPF classification diagram that shows composition on the basis of mineral modal amount determined at the optical microscope, in comparison with data from Cesana et al. (1976).

77x67mm (300 x 300 DPI)

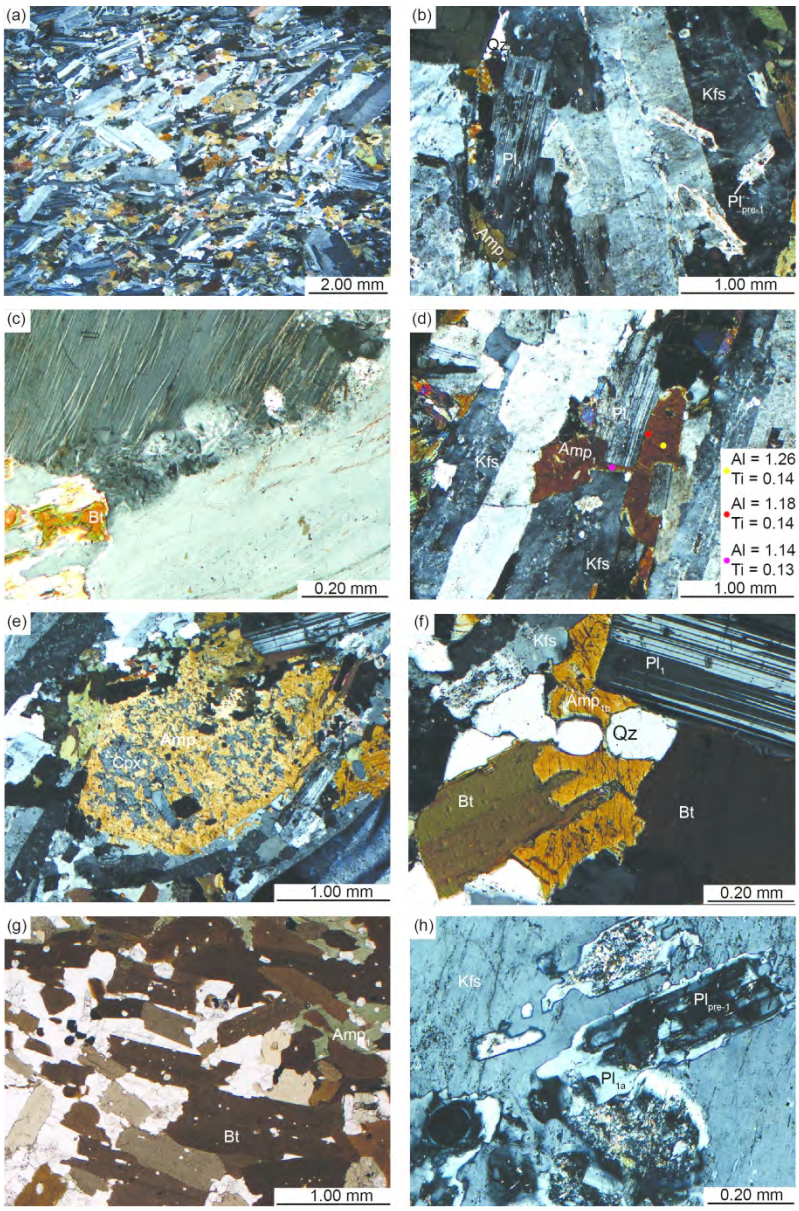

Figure 6. Microstructure and microtexture in igneous rocks; (a) magmatic foliation marked by Kfs (K-feldspar) and Pl1 (plagioclase 1), and Amp1 (amphibole 1), sample 59A, crossed polars; (b) shape preferred orientation of Kfs (K-feldspar) and Pl1 (plagioclase 1) defining magmatic foliation. Kfs (K-feldspar) shows Carlsbad twinning and growth zoning, and contains Plpre-1 (plagioclase pre-1), which shows irregular rims overgrown by Pl1a (plagioclase 1a; white rim). Plpre-1 (plagioclase pre-1) is partially replaced by Ep (epidote) aggregate (high birefringence); sample 3130105; crossed polars; (c) myrmekites at the grain boundary of two Kfs (K-feldspar) crystals. Kfs (K-feldspar) contains flame perthites; sample BPA10; crossed polars; (d) Kfs (K-feldspar), Pl1 (plagioclase 1), and minor Amp1 (amphibole 1) marking the magmatic foliation; Amp1 (amphibole 1) forms a single crystal that is both parallel to the magmatic foliation and interstitial between Kfs (K-feldspar) and Pl1 (plagioclase 1); a side content of Al and Ti (apfu) are shows for three points (see next section for details): yellow = Amp1a (amphibole 1a, core); red = Amp1b (amphibole 1b, rim); pink = Amp1b (amphibole 1b, interstitial); sample 3130105; crossed polars; (e) Cpx (clinopyroxene, grey) partially replaced by Amp1a (amphibole 1a, yellow); magmatic foliation wraps Cpx (clinopyroxene); sample 59A; crossed polars; (f) Amp1b (amphibole 1b) interstitial between euhedral Pl1

(plagioclase 1) and Bt (biotite), and rounded Qz crystals; sample 59A; crossed polars; (g) magmatic foliation in mafic monzonite marked by shape preferred orientation of euhedral Bt (biotite); Amp1 (amphibole 1) is mostly interstitial but elongate parallel to the foliation; sample BPA4; plane polarized light; (h) Kfs (K-feldspar) enclosing Plpre-1 (plagioclase pre-1) with irregular rims overgrown by Pl1a (plagioclase 1a); sample BPA4; crossed polars.

172x260mm (300 x 300 DPI)

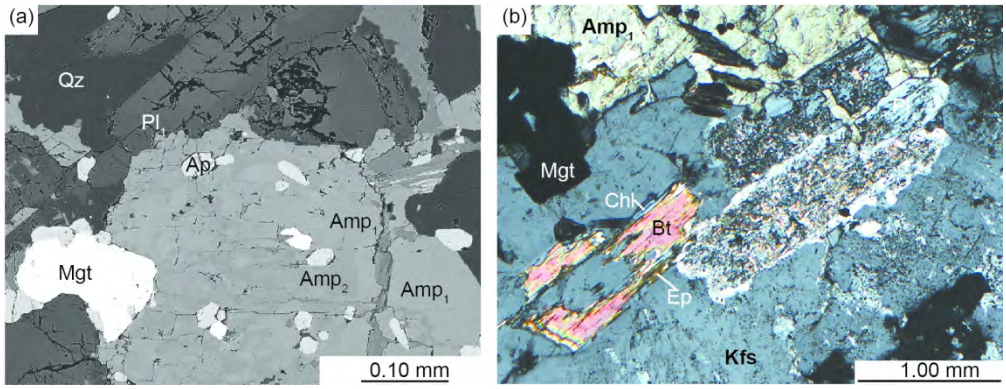

Figure 7. (a) BSE image of Amp2 (amphibole 2, dark grey) patchy overgrowth on Amp1 (amphibole 1, light grey), amphibole encloses euhedral Ap (apatite) and Mgt (magnetite); sample BPB1; (b) Pl (plagioclase) partially replaced by fine grained aggregates mostly of Ep (epidote); Bt (biotite) rimmed by Chl (chlorite) and Ep (epidote); sample BPB1, crossed polars.

171x65mm (300 x 300 DPI)

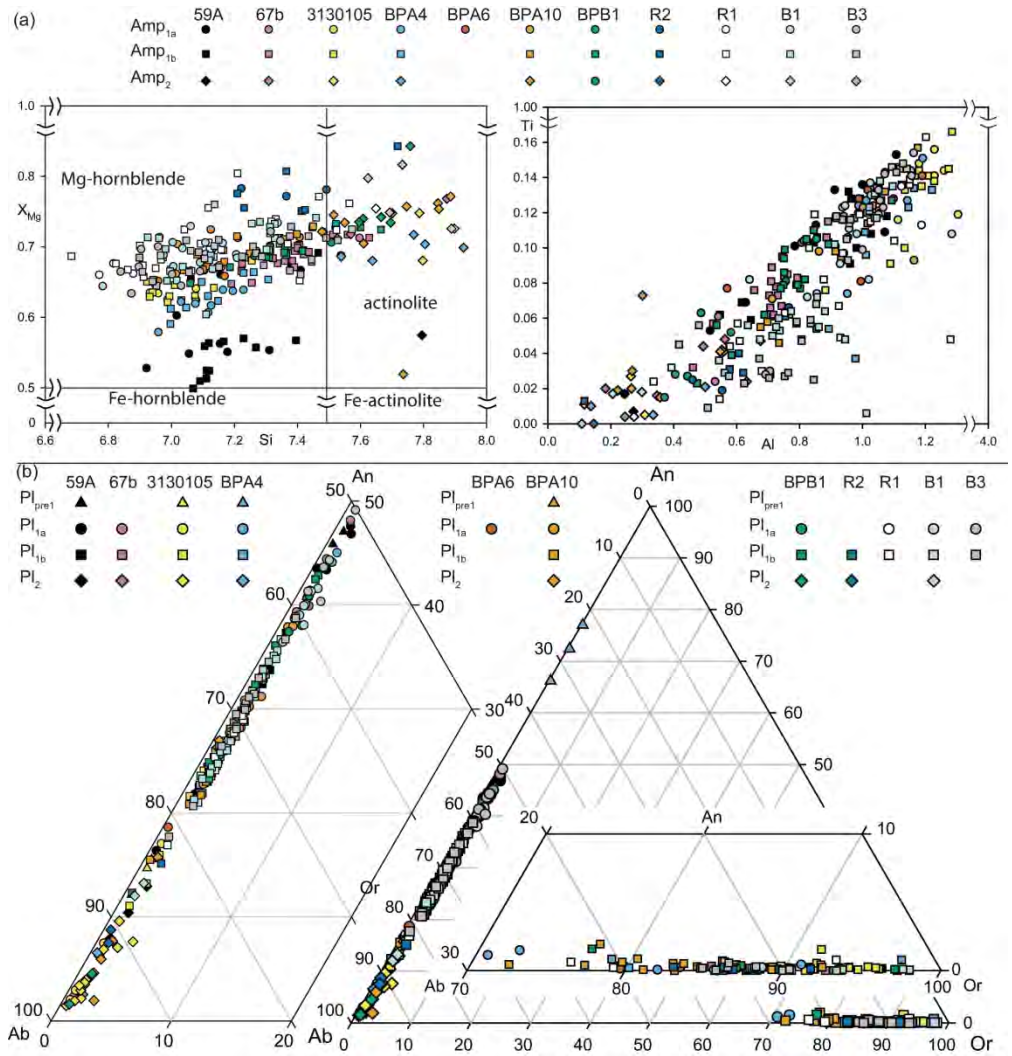

Figure 8. (a) XMg vs. Si compositional diagram (Leake et al. 1997) and Ti vs. Al diagram for amphibole; (b) ternary diagram for feldspar.

194x204mm (300 x 300 DPI)

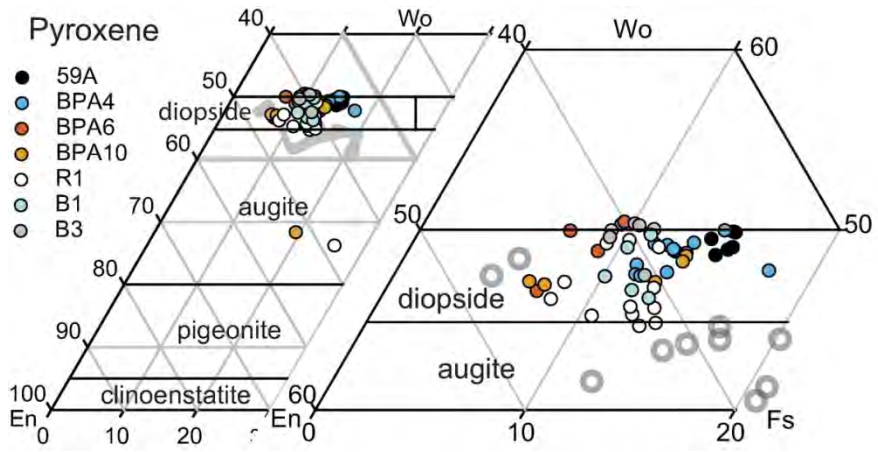

Figure 9. Ternary compositional diagram for pyroxene. Grey field and open circles in the full diagram and close-up, respectively, represent the composition of clinopyroxene phenocrysts from shoshonitic andesite lavas (Callegari et al. 2004). Shoshonitic clinopyroxene formulae were calculated according to Morimoto (1988) to be compared and plotted with clinopyroxene from this work.

115x51mm (300 x 300 DPI)

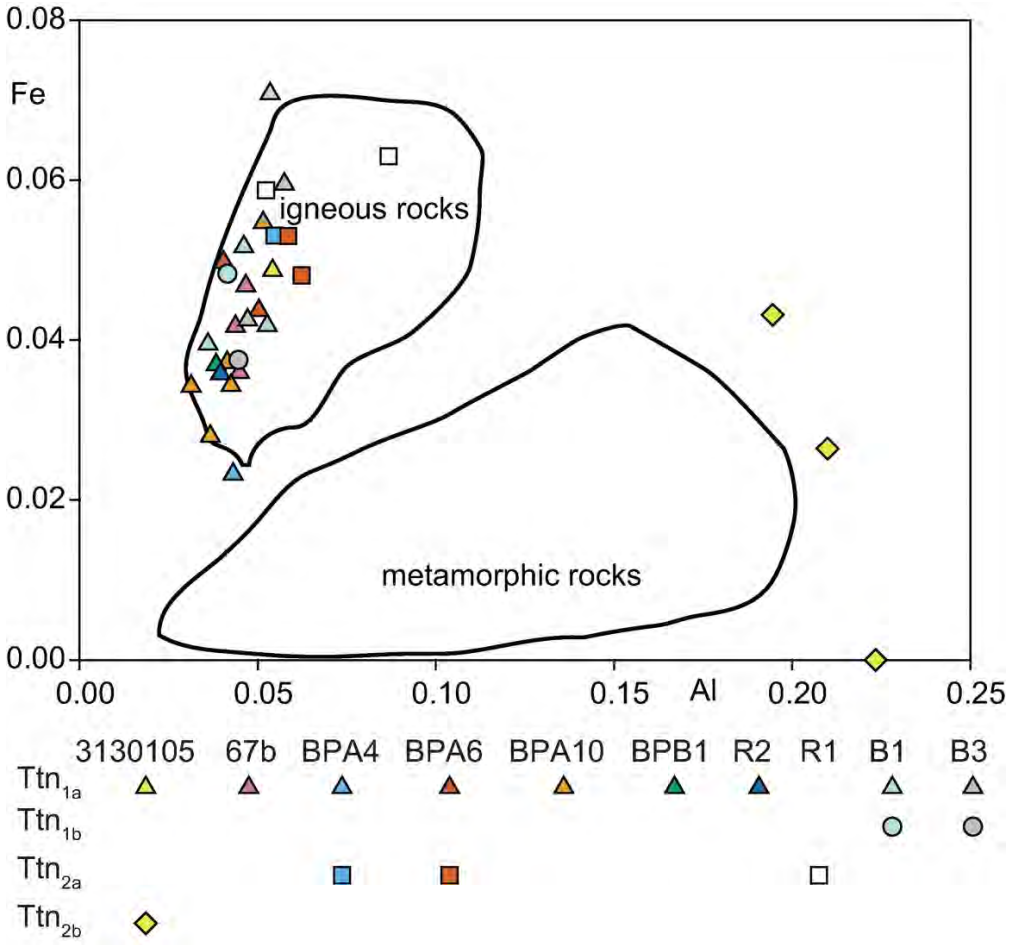

Figure 10. Binary classification diagram for titanite (Aleinikoff et al. 2002).

98x92mm (300 x 300 DPI)

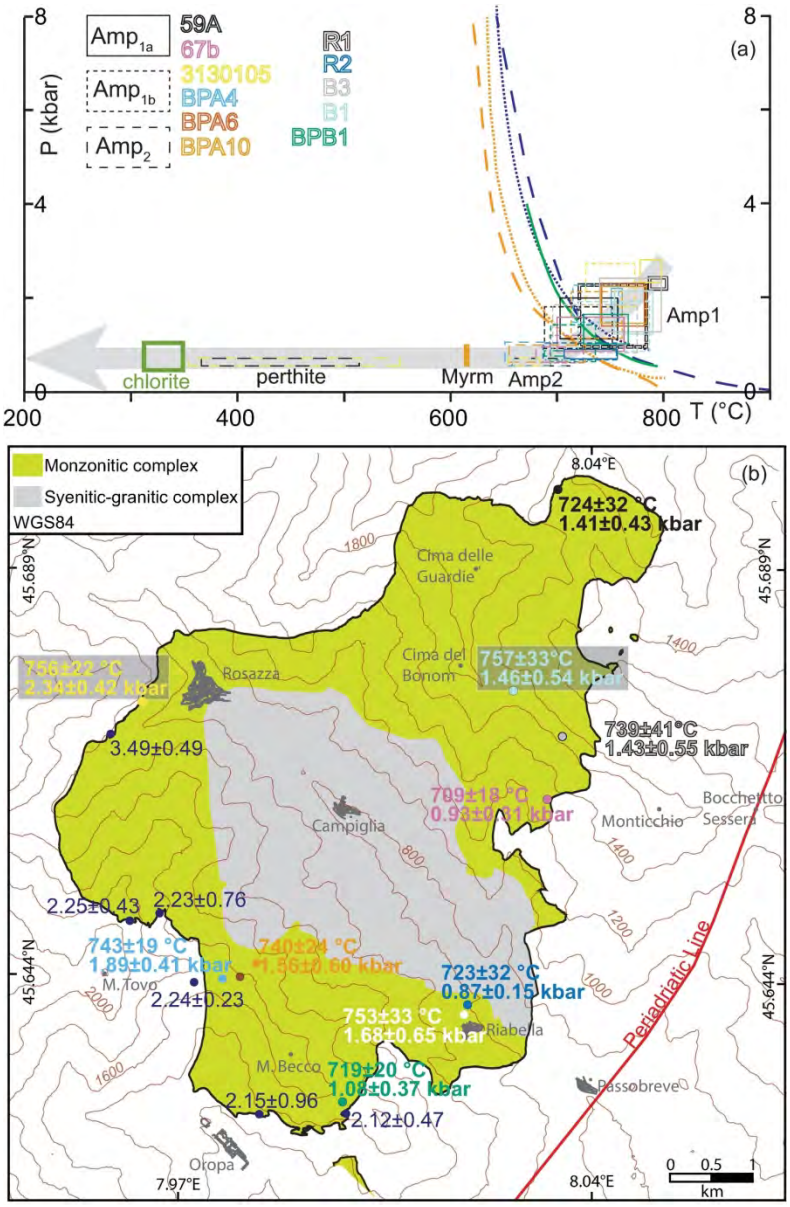

Figure 11. (a) Cooling path of the Biella pluton. Wet granite solidus (orange): dotted line (Holland and Powell 2001), dashed line (Stern et al. 1975). Wet granodiorite solidus (green solid line) (Piwinskii 1968). Wet tonalite solidus (blue): dotted line (Schmidt 1993), dashed line (Stern et al. 1975); pressure for myrmekite, perthite, and chlorite development are constrained from pressures estimated for Amp2 in each sample; (b) Geological sketch of the Biella pluton with punctual distribution of temperatures and pressures estimated for igneous rocks and pressures estimated for contact metamorphism in country rocks (blue numbers in kbar); P-T values for magmatic rocks derive from the weighted average that includes all estimates for Amp1a and Amp1b in each sample and P values in host rocks derive from weighted average of all estimates for each sample; colours of P-T values for pluton plutonic rocks are the same as in Figures from 8 to 11a.

131x201mm (300 x 300 DPI)

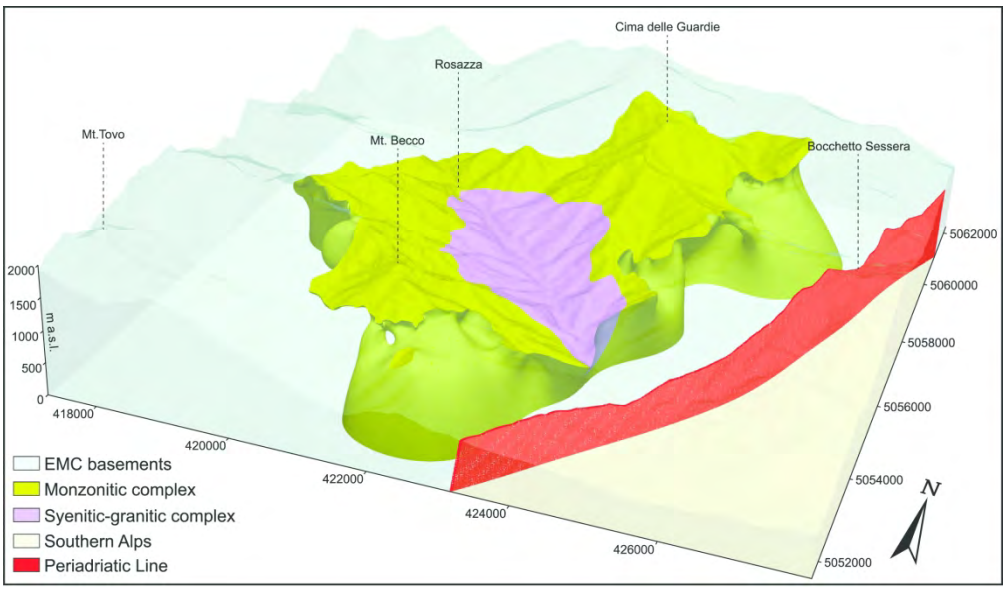

Figure 12. 3D geological model visualized through Paraview software. Volume: 110 km3 divided into voxels with dimension of 50-50-15 m. The geological formations considered are EMC (Eclogitic Micaschists Complex, Sesia-Lanzo Zone) basement, monzonitic complex, syenitic-granitic complex, Southern Alps. The orientation of Periadriatic Line is from Schmid et al. (1989) and Handy et al. (2005).

208x120mm (300 x 300 DPI)

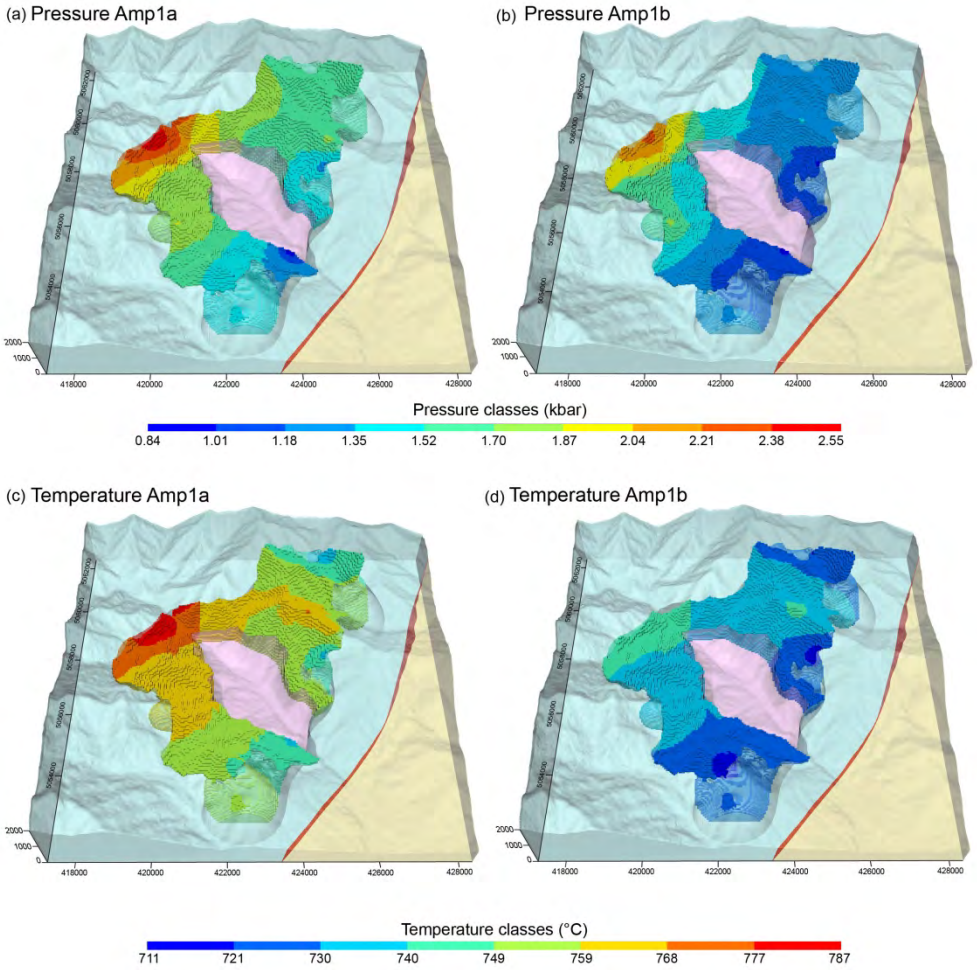

Figure 13. 3D results of the Inverse distance weight interpolation starting from pressure point estimates (a: Amp1a; b: Amp1b) and from temperature point estimates (c: Amp1a; d: Amp1b). EMC (Eclogitic Micaschists Complex, Sesia-Lanzo Zone) basement = pale blue; Southern Alps = pale yellow; Syenitic-granitic complex = pink; Periadriatic Line = red.

213x211mm (300 x 300 DPI)

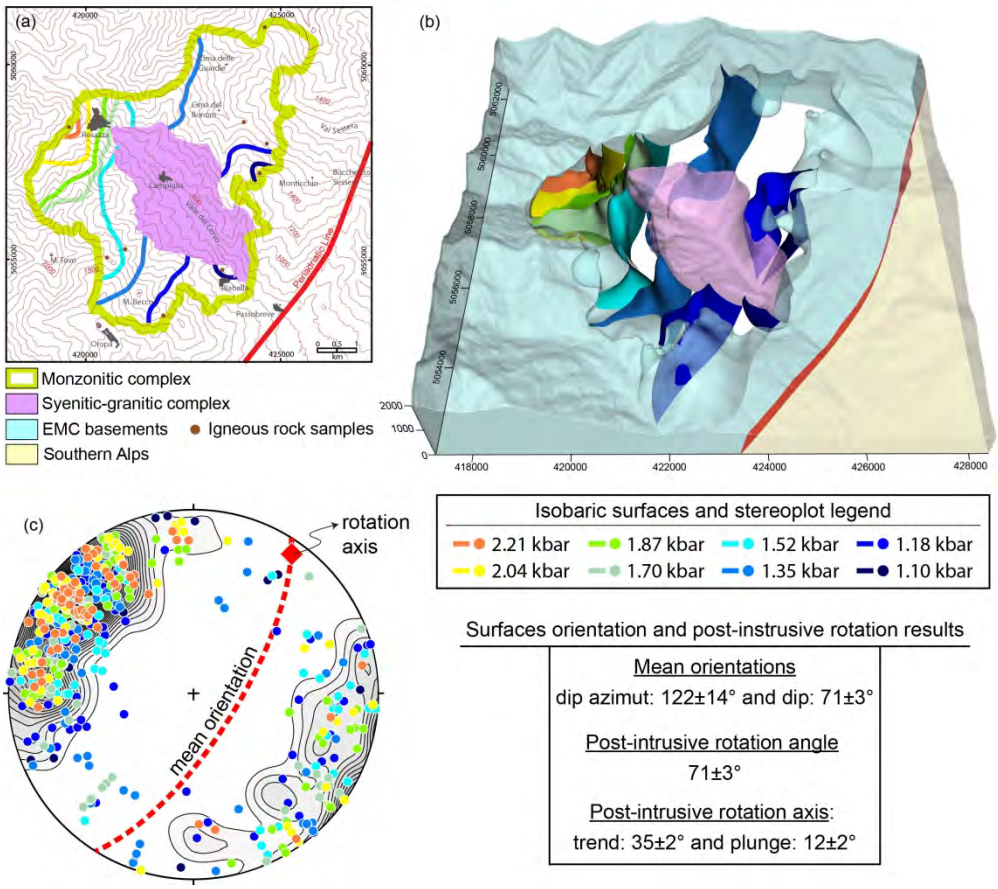

Figure 14. Isobaric surfaces for Amp1b in (a) 2-dimensions and in (b) 3-dimensions. The chosen isobaric surfaces are the classes' boundary from the IDW interpolations (Figure 11). The orientation data of all isobaric surfaces grouped in a stereonet with the mean orientation plane and the rotation axial pole. The enclosed table shows the surface orientation and post-intrusive rotation results. The syenitic-granitic complex, the monzonitic complex, the EMC (Eclogitic Micaschists Complex, Sesia-Lanzo Zone) basements, the Southern Alps, the Periadriatic Line, and the rock samples are shown.

207x183mm (300 x 300 DPI)

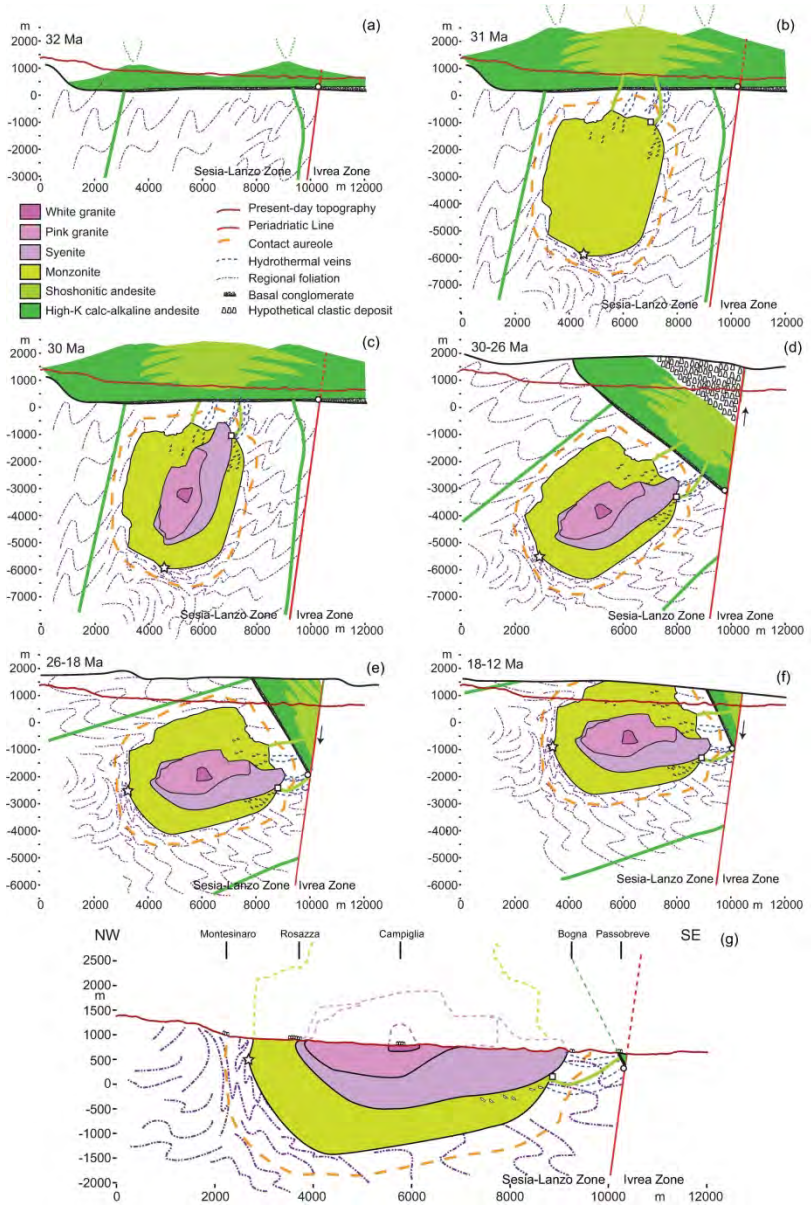

Figure 15. Schematic representation of the magmatic and tectonic evolution of the andesite cover, Biella pluton, and country rocks (Cervo block) over Oligocene and Miocene. This interpretation is based on original data presented in this work and interpretations, data, and re-interpretation of data from the literature (Schmid et al. 1989; Zingg and Hunziker 1990; Biggiogero et al. 1994; Callegari et al. 2004; Zanoni et al. 2008, 2010; Berger et al. 2012a,b; Kapferer et al. 2011, 2012; Zanoni 2016). In any sketch, the present-day topographic profile of the Valle del Cervo axis is reported as a reference and the actual depths at which it is shown the pluton have to be referred to the altitude of palaeo-topography. (a) At about 32 Ma the Sesia-Lanzo Zone rocks were already exposed and fed the Rupelian basal conglomerate that was overlaid by high-K calc-alkaline andesitic lava flows from active volcanism; most likely the andesitic volcaniclastic cover was deposited also on the Ivrea Zone; (b) at about 31 Ma the high-K calc-alkaline volcanism was ongoing and the Biella monzonite emplaced and room was facilitated by magmatic stopping in the roof and ductile deformation of the host rocks at the bottom; at this time the shoshonitic volcanism was fed by the monzonite reservoir itself and with the contribution of the ongoing high-K calc-alkaline volcanism the andesitic sequence possibly reached a thickness of 2.3 km; (c) at about 30 Ma the syenite intruded with

subsequent differentiation of the pink and white granite; by this time possibly the volcanic activity was over; (d) between 30 and 26 Ma, the Cervo block rotated southeastward accompanied by a tectonic burial that took the bottom of the andesite sequence, approaching the Periadriatic Line, at a depth of 5 km; at the same time the Ivrea Zone could have been uplift with consequent complete erosion of the top cover; (e) between 26 and 18 Ma, the uplift of the Cervo block started with ongoing rotation and zircon fission tracks were recorded first in andesite and afterward in the Biella pluton; (f) between 18 and 12 Ma, the ongoing uplift and rotation of the Cervo block is responsible for apatite fission tracks in andesite and later in plutonic rocks; at the end of this time interval, possibly the rotation stopped; (g) present-day section of the Biella pluton and its country rocks along the Valle del Cervo axis; the reconstruction of the buried part of the pluton is facilitated by the 3D model, whereas the interpretation of the pluton boundaries at altitude higher than topography considers the geological boundaries on the slopes above the valley axis.

190x282mm (300 x 300 DPI)

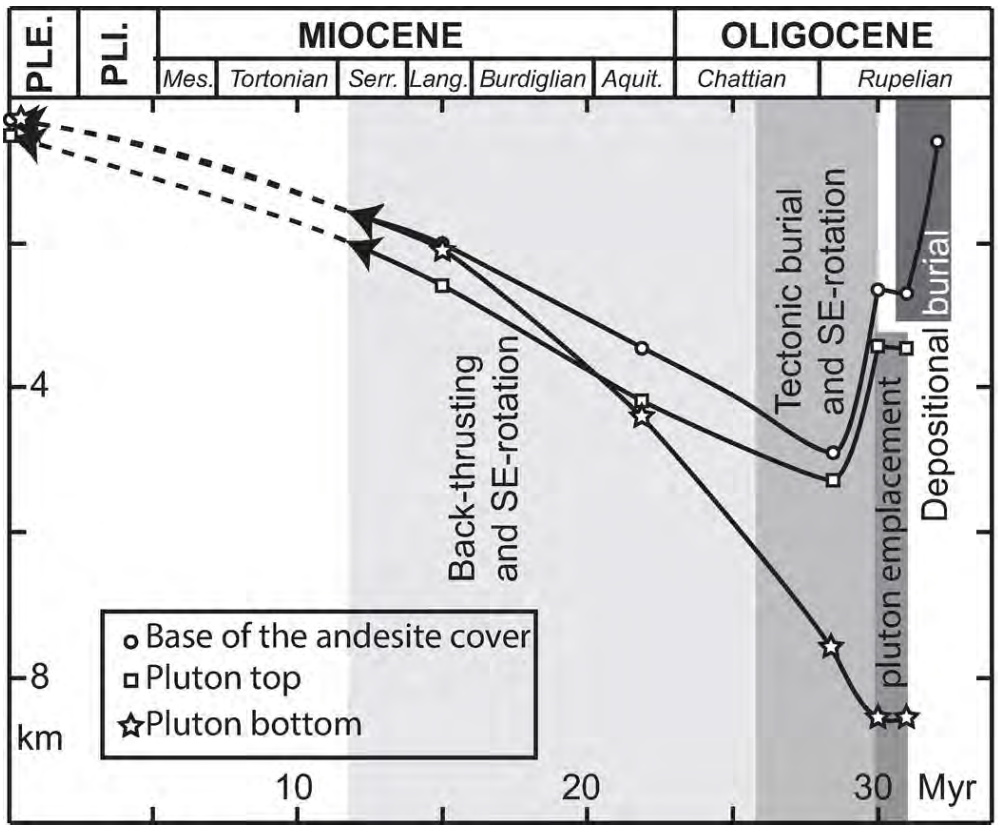

Figure 16. Inferred D (depth) – t (time) path of the Cervo block during Oligocene and Miocene. The D-t path is illustrated by means of three reference points, which were chosen at the base of the andesite cover, and at pluton roof and bottom. Symbols of the reference points are located in the sketches of Figure 15. Solid line = constrained path; dashed line = not constrained path. Depositional burial of andesite cover and pluton emplacement may be overlapped in time. The block uplift and rotation may keep going also after the Serravalian (i.e. after 12 Ma).

89x72mm (300 x 300 DPI)

Mineral	MAGMATIC			LATE to POST-MAGMATIC		
Pyroxene	Cpx: euhedral crystals					
Plagioclase	Pl_{pre1}: irregular grain boudaries; enclosed in Kfs	Pl_{1a}: inner part of crystals marking magmatic foliation or reaction rim of	Pl_{1b}: outer part of crystals marking magmatic foliation	Pl_{2a}: crystals in myrmekite	Pl_{2b}: perthitic exsolution	Pl_{2c}: rim of Pl_1, or in rare veins and interstitial spaces
Magnetite/Apatite	Euhedral to subhedral crystals in Amp_{1a} and Bt					
Amphibole		Amp_{1a}: inner part of crystals marking the magmatic foliation; rim of Cpx	Amp_{1b}: outer part of crystals marking the magmatic foliation; interstitial grains	Amp_2: rim of Amp_1		
K-feldspar	Kfs_{1a}: graphic texture in Pl_1 only in mafic monzonite	Kfs: crystals marking the magmatic foliation	Kfs1b: poikilitic crystals only in mafic monzonite			
Biotite		Anhedral to euhedral crystals marking the				
Titanite		Ttn_{1a}: euhedral crystals in poikilitic Amp_{1a}	Ttn_{1b}: interstitial grains	Ttn_{2a}: intergranular films	Ttn_{2b}: crystal that overgrew Bt, with Ep and Chl	
Quartz			interstitial crystals			

Sample	Generation	Al^{IV}	Al^{tot}	Ti	X_{Mg}	Ca
3130105	$Amp_{1a\ core}$	1.03±0.05	1.22±0.07	0.14±0.02	0.64±0.01	1.85±0.03
	Amp_{1b}	0.97±0.10	1.15±0.11	0.13±0.03	0.64±0.02	1.89±0.06
	Amp_{2}	0.17±0.06	0.23±0.1	0.01±0.01	0.72±0.03	1.93±0.06
59A	$Amp_{1a\ RR}$	0.78±0.25	0.83±0.24	0.10±0.04	0.63±0.06	1.87±0.07
	$Amp_{1a\ core}$	0.86±0.12	0.93±0.12	0.12±0.02	0.56±0.02	1.77±0.08
	Amp_{1b}	0.79±0.14	0.87±0.17	0.10±0.03	0.57±0.06	1.78±0.07
	Amp_{2}	0.21	0.27	0.01	0.57	1.89
BPA4	$Amp_{1a\ RR}$	0.85±0.04	1.00±0.01	0.12±0.00	0.62±0.03	1.85±0.03
	$Amp_{1a\ core}$	0.90±0.09	1.05±0.10	0.12±0.02	0.60±0.02	1.84±0.02
	Amp_{1b}	0.87±0.11	1.03±0.12	0.10±0.04	0.64±0.03	1.87±0.02
	Amp_{2}	0.26±0.15	0.37±0.2	0.01±0.01	0.70±0.01	1.91±0.02
BPA6	$Amp_{1a\ core}$	0.83±0.19	0.95±0.23	0.11±0.03	0.69±0.03	1.93±0.03
BPA10	$Amp_{1a\ RR}$	0.98	1.04	0.12	0.7	1.86
	$Amp_{1a\ core}$	0.81±0.18	0.94±0.20	0.10±0.04	0.69±0.02	1.87±0.04
	Amp_{1b}	0.78±0.15	0.91±0.18	0.10±0.04	0.70±003	1.87±0.04
	Amp_{2}	0.32±0.14	0.42±0.15	0.04±0.02	0.71±0.08	1.89±0.04
B1	$Amp_{1a\ RR}$	0.77±0.18	0.79±0.21	0.10±0.03	0.72±0.02	1.93±0.02
	$Amp_{1a\ core}$	0.95±0.12	1.00±0.12	0.11±0.02	0.69±0.02	1.87±0.05
	Amp_{1b}	0.85±0.15	0.88±0.16	0.08±0.04	0.70±0.03	1.90±0.04
	Amp_{2}	0.20±0.10	0.20±0.10	0.01±0.01	0.78±0.05	1.84±0.13
B3	$Amp_{1a\ core}$	0.97±0.17	1.01±0.17	0.11±0.05	0.68±0.03	1.90±0.02
	Amp_{1b}	077±0.20	0.83±0.21	0.07±0.05	0.69±0.02	1.90±0.03
	Amp_{2}	0.24	0.24	0.02	0.75	1.98
67b	$Amp_{1a\ core}$	0.63±0.22	0.71±0.21	0.07±0.04	0.71±0.02	1.87±0.02
	Amp_{1b}	0.62±0.10	0.73±0.11	0.08±0.02	0.69±0.02	1.86±0.02
	Amp_{2}	0.33±0.16	0.40±0.17	0.03±0.02	0.74±0.03	1.88±0.02
BPB1	$Amp_{1a\ core}$	0.73±0.14	0.81±0.13	0.09±0.02	0.70±0.01	1.86±0.02
	Amp_{1b}	0.64±0.15	0.76±0.14	0.08±0.03	0.70±0.02	1.87±0.02
	Amp_{2}	0.36±0.05	0.43±0.05	0.03±0.02	0.74±0.00	1.89±0.02
R1	$Amp_{1a\ RR}$	1.15±0.05	1.16±0.05	0.12±0.02	0.66±0.00	1.92±0.03
	$Amp_{1a\ core}$	1.13	1.13	0.15	0.68	1.92
	Amp_{1b}	0.83±0.25	0.87±0.26	0.08±0.04	0.71±0.04	1.88±0.06
	Amp_{2}	0.27	0.27	0.00	0.75	2.00
R2	Amp_{1a}	0.59±0.16	0.59±0.16	0.04±0.03	0.78±0.01	1.91±0.02
	Amp_{1b}	0.57±0.24	0.58±0.24	0.04±0.02	0.78±0.04	1.91±0.04
	Amp_{2}	0.15	0.15	0.00	0.84	1.79

Cations calculated according to Locock (2014) Tot analyses:

n = numbers of analyses

$Amp_{1a\ RR}$: amphibole at clinopyroxene reaction rim

$Amp_{1a\ core}$: core of amphibole marking the magamtic foliation

n
6
12
3
5
5
15
1
3
7
11
5
5
1
9
23
14
2
12
25
3
10
27
1
4
21
4
6
16
4
2
1
25
1
3
7
1
300

Sample	Pl_{pre-1}				Pl_{1a} on Sm				Kfs_{1a}		
	XAn	XOr	XAb	n	XAn	XOr	XAb	n	XAn	XOr	XAb
3130105	19±7	1±0	80±7	5	24±6	1±0	76±6	3			
59A	46±1	1±0	53±1	2	41±10	1±0	58±10	6			
BPA4	72±5	<0.5	28±5	3	37±8	1±0	62±8	7	1±1	80±7	19±7
BPA6											
BPA10	41±1	1±0	59±0	3	31±5	1±0	68±5	8			
B1					40±1	1±0	59±1	6			
B3					40±7	1±0	59±7	8			
67b					37±11	1±0	62±11	4			
BPB1					36±6	1±0	63±3	6			
R1					39±1	1±0	60±1	2			
R2											
tot analyses:				13				50			

XAn = Ca/(Ca+Na+K)
XOr = K/(Ca+Na+K)
XAb = Na/(Ca+Na+K)
Sm = Magmatic foliation
RR = reaction rim
Myrm = myrmekite
n = numbers of analyses
The composition of perthite refers to Na parts of the unmixed patches enclosed in K-feldspar.

	Pl_{1a} in RR				Pl_{1b}				Kfs				
n	XAn	XOr	XAb	n	XAn	XOr	XAb	n	XAn	XOr	XAb	n	XAn
	7±6	1±0	92±6	4	22±5	1±0	77±5	14	<0.5	92±3	7±3	19	
	16	1	83	1	31±8	1±0	68±8	11	<0.5	93±3	7±3	8	
7					25±4	1±0	73±4	10	<0.5	87±7	12±7	8	
					23.80	1.41	74.79	2	<0.5	81±3	18±3	2	
					25±3	1±0	74±3	16	<0.5	84±5	16±5	19	27±0
					29±6	1±0	70±6	20	<0.5	96±2	4±2	3	
					30±5	1±0	69±5	16	<0.5	88±3	12±2	10	
					28±3	1±0	71±3	14	<0.5	89±3	11±3	8	
					29±6	1±0	70±6	18	<0.5	87±4	13±4	10	
					27±3	1±0	72±3	14	<0.5	85±7	15±7	5	
					19±9	1±1	80±9	3	<0.5	87±4	12±4	4	
7				5				138				96	

Pl_{2a} (Myrm)			Pl_{2b} (Perthite)				Pl_{2c}				
XOr	XAb	n	XAn	XOr	XAb	n	XAn	XOr	XAb	n	
			4±2	1±1	94±3	12	6±4	1±0	93±5	2	
			7±3	1±0	91±3	3	13	1	86	1	
							7	1	93	1	
1±0	73±0	2	6	1	93	1	8±7	2±1	90±6	3	
							13±1	1±0	86±1	2	
							2±0	1±0	97±1	2	
							3±2	1±0	96±2	2	
							8±1	1±0	91±1	2	
		2				16				15	**327**

Sample	Si	Al^{VI}	Ca	X_{Mg}	n
59A	1.99±0.01	0	0.97±0.01	0.73±0.02	7
BPA4	1.98±0.03	0.02±0.01	0.95±0.02	0.76±0.04	13
BPA6	1.96±0.01	0	0.91±0.02	0.86±0.03	4
BPA10	1.98±0.03	0.00-0.08	0.85±0.17	0.80±0.07	6
R1	1.93±0.02	0.00-0.08	0.89±0.12	0.79±0.05	14
B1	1.96±0.01	0	0.95±0.03	0.80±0.02	7
B3	1.95±0.01	0	0.97±0.03	0.81±0.02	4

Cations calculated on the basis of 6 oxygen atoms
n = numbers of analyses

tot analyses: 55

Sample	Ti	Al^{IV}	X_{Mg}	n
59A	0.51±0.02	2.36±0.03	0.41±0.01	6
67b	0.43±0.07	2.30±0.02	0.53±0.01	3
3130105	0.46±0.03	2.32±0.05	0.55±0.00	7
BPA4	0.49±0.04	2.42±0.06	0.52±0.02	9
BPA6	0.35±0.00	2.28±0.01	0.60±0.00	2
BPA10	0.43±0.11	2.30±0.07	0.59±0.03	16
BPB1	0.48±0.04	2.34±0.06	0.53±0.01	6
R1	0.43±0.07	2.43±0.04	0.56±0.01	10
B1	0.41±0.07	2.36±0.05	0.56±0.02	12
B3	0.44±0.08	2.41±0.05	0.53±0.01	14

Cations calculated on the basis of 22 oxygen atoms
n = numbers of analyses

tot analyses: 85

Sample		Ti	Al	Fe^{2+}	n
67b	Ttn1a	0.93±0.00	0.05±0.00	0.04±0.01	3
3130105	Ttn1a	0.9	0.05	0.05	1
	Ttn2b	0.78±0.01	0.21±0.01	0.02±0.02	3
BPA4	Ttn1a	0.93	0.04	0.02	1
	Ttn2a	0.89	0.05	0.05	1
BPA6	Ttn1a	0.94±0.00	0.05±0.00	0.05±0.00	2
	Ttn2a	0.92±0.00	0.06±0.00	0.05±0.00	2
BPA10	Ttn1a	0.93±0.01	0.04±0.01	0.04±0.01	5
BPB1	Ttn1a	0.94	0.04	0.04	1
B1	Ttn1a	0.93±0.01	0.05±0.01	0.05±0.01	4
	Ttn1b	0.93	0.04	0.05	1
B3	Ttn1a	0.92±0.01	0.05±0.01	0.05±0.02	2
	Ttn1b	0.93	0.04	0.04	1
R1	Ttn2a	0.93±0.01	0.07±0.02	0.06±0.00	2
R2	Ttn1a	0.95	0.04	0.04	1

Cations calculated on the basis of 5 oxygen atoms
n = numbers of analyses

tot analyses: 30

Sample	Al^{VI}	Fe^{3+}	Fe^{2+}	Ca	n
59A (allanite)	1.54±0.03	0.92±0.02	0.64±0.03	1.32±0.00	2
59A	1.87	1.11	0.02	1.99	1
3130105	2.36±0.15	0.47±0.32	0.00-0.44	1.92±0.04	3
BPA4	2.23±0.52	0.00-0.73	0.00-0.67	1.93±0.15	6
BPA6	2.14±0.15	0.82±0.16	0.00	1.92±0.05	6
BPA10	2.04±0.42	0.88±0.40	0.00-0.15	1.93±0.02	3
BPB1	2.38	0.61	0.00	1.90	1
R2	2.26	0.73	0.05	1.89	1

Cations calculated according to Yavuz and Yıldırım (2018)
n = numbers of analyses

tot analyses: 23

Sample	X_{Mg}	Al^{IV}	Al^{VI}	n
59A	0.48±0.01	1.03±0.16	1.13±0.01	2
67b	0.59	0.93	1.28	1
3130105	0.59±0.02	1.07±0.14	1.30±0.05	7
BPA4	0.60±0.01	0.96±0.18	1.18±0.06	2
BPA6	0.51±013	1.16±0.10	1.24±0.03	2
BPA10	0.60±0.05	0.97±0.20	1.11±0.07	6
BPB1	0.59	1.03	1.13	1
B1	0.39	1.32	1.44	1
B3	0.50±0.01	0.54±0.01	2.65±0.03	2

Cations calculated according to Buourdelle et al. (2013)
n = numbers of analyses

tot analyses: 24

Total number of analyses	
Amphibole	300
Feldspar	327
Clinopyroxene	55
Biotite	85
Titanite	30
Epidote	23
Chlorite	24
Total	**844**

	Sample 59A				Sample 67b		
Generation	Amp 1a RR	Amp 1a core	Amp 1b	Amp 2	Amp 1a	Amp 1b	Amp 2
identifier/label	59A-C4-73	59A-C2-30	59A-C1-4	59A-C2-28	67b-C2-30	67b-C1-5	67b-C2-32
SiO2	47.90	47.29	48.04	53.12	49.05	50.26	55.55
TiO2	1.19	1.37	0.89	0.06	0.97	0.80	0.19
Al2O3	5.18	6.33	5.58	1.57	5.55	4.12	1.10
Cr2O3	0.02	0.05	0.06	0.12	0.03	0.00	0.00
MnO	0.48	0.45	0.36	0.34	0.41	0.41	0.51
FeO	12.43	14.69	15.62	16.70	12.33	11.40	9.50
Fe2O3	1.97	1.56	2.64	0.98	1.92	1.88	0.50
NiO	0.00	0.00	0.00	0.00	0.00	0.00	0.00
MgO	13.58	12.49	11.42	12.65	14.11	14.82	17.68
CaO	11.54	11.34	11.18	12.03	11.95	11.85	12.44
Na2O	1.24	1.46	1.17	0.31	1.18	0.90	0.27
K2O	0.55	0.78	0.53	0.11	0.58	0.42	0.09
Total	96.07	97.80	97.51	97.99	98.08	96.86	97.82
T (ideally 8 apfu)							
Si	7.16	7.02	7.17	7.80	7.16	7.37	7.87
Al	0.84	0.98	0.83	0.21	0.84	0.64	0.13
Ti	0.00	0.00	0.00	0.00	0.00	0.00	0.00
Fe3+	0.00	0.00	0.00	0.00	0.00	0.00	0.00
T subtotal	8.00	8.00	8.00	8.00	8.00	8.00	8.00
C (ideally 5 apfu)							
Ti	0.13	0.15	0.10	0.01	0.11	0.09	0.02
Al	0.07	0.13	0.15	0.07	0.11	0.08	0.06
Cr	0.00	0.01	0.01	0.01	0.00	0.00	0.00
Fe3+	0.22	0.17	0.30	0.11	0.21	0.21	0.05
Ni	0.00	0.00	0.00	0.00	0.00	0.00	0.00
Mn2+	0.00	0.00	0.00	0.00	0.00	0.00	0.01
Fe2+	1.55	1.78	1.91	2.04	1.50	1.39	1.13
Mg	3.03	2.76	2.54	2.77	3.07	3.24	3.74
C subtotal	5.00	5.00	5.00	5.00	5.00	5.00	5.00
B (ideally 2 apfu)							
Mn2+	0.06	0.06	0.05	0.04	0.05	0.05	0.05
Fe2+	0.00	0.04	0.04	0.01	0.01	0.01	0.00
Ca	1.85	1.80	1.79	1.89	1.87	1.86	1.89
Na	0.09	0.10	0.13	0.05	0.07	0.08	0.06
B subtotal	2.00	2.00	2.00	2.00	2.00	2.00	2.00
A (from 0 to 1 apfu							
Na	0.27	0.32	0.21	0.04	0.26	0.18	0.02
K	0.11	0.15	0.10	0.02	0.11	0.08	0.02
A subtotal	0.38	0.47	0.31	0.06	0.37	0.25	0.03
Sum T,C,B,A	15.38	15.47	15.31	15.06	15.37	15.25	15.04

Formula according to Locock (2014)
Amp 1a RR: amphibole on clinopyroxene reaction rim
Amp 1a core: core of amphibole on magmatic foliation

Sample 3130105			Sample BPA4			
Amp 1a	Amp 1b	Amp 2	Amp 1a RR	Amp 1a core	Amp 1b	Amp 2
3130105-c2-45	3130105-c2-40	3130105-c3-56	BPA4-c1-33	BPA4-c4-89	BPA4-c1-31	BPA4-c1-35
46.60	48.30	54.24	48.21	47.93	49.90	52.48
1.26	0.90	0.25	1.14	1.08	0.49	0.19
7.01	6.51	1.56	5.81	5.77	4.95	2.91
0.00	0.01	0.05	0.19	0.01	0.06	0.01
0.40	0.46	0.34	0.33	0.41	0.35	0.31
13.46	12.80	10.06	14.04	14.33	12.99	12.47
1.37	1.94	0.99	1.81	2.21	1.79	0.61
0.03	0.03	0.05	0.01	0.00	0.00	0.04
13.06	12.87	16.75	12.67	12.40	13.76	14.89
11.72	11.38	12.30	11.46	11.42	11.99	12.36
1.41	1.17	0.45	1.45	1.29	0.94	0.66
0.80	0.63	0.13	0.52	0.65	0.44	0.19
97.12	96.99	97.17	97.63	97.50	97.65	97.13
6.94	7.14	7.79	7.13	7.12	7.31	7.64
1.07	0.87	0.21	0.87	0.88	0.69	0.36
0.00	0.00	0.00	0.00	0.00	0.00	0.00
0.00	0.00	0.00	0.00	0.00	0.00	0.00
8.00	8.00	8.00	8.00	8.00	8.00	8.00
0.14	0.10	0.03	0.13	0.12	0.05	0.02
0.16	0.27	0.05	0.14	0.13	0.16	0.14
0.00	0.00	0.01	0.02	0.00	0.01	0.00
0.15	0.22	0.11	0.20	0.25	0.20	0.07
0.00	0.00	0.01	0.00	0.00	0.00	0.01
0.00	0.00	0.01	0.00	0.00	0.00	0.02
1.64	1.58	1.21	1.72	1.76	1.58	1.52
2.90	2.83	3.59	2.79	2.75	3.00	3.23
5.00	5.00	5.00	5.00	5.00	5.00	5.00
0.05	0.06	0.03	0.04	0.05	0.04	0.02
0.03	0.00	0.00	0.02	0.02	0.01	0.00
1.87	1.80	1.89	1.82	1.82	1.88	1.93
0.05	0.14	0.08	0.13	0.11	0.06	0.05
2.00	2.00	2.00	2.00	2.00	2.00	2.00
0.36	0.20	0.05	0.29	0.26	0.20	0.13
0.15	0.12	0.03	0.10	0.12	0.08	0.04
0.51	0.32	0.07	0.39	0.38	0.29	0.17
15.51	15.32	15.07	15.39	15.38	15.29	15.17

Sample BPA6	Sample BPA10				Sample BPB1	
Amp 1a	Amp 1a RR	Amp 1a core	Amp 1b	Amp 2	Amp 1a	Amp 1b
bpa6p80	BPA10-c1-19	BPA10-c2-36	BPA10-c1-12	BPA10-c1-5	BPB1-C1-9	BPB1-C1-12
48.84	47.93	48.63	50.50	55.93	48.98	51.69
0.74	1.12	1.11	0.59	0.18	0.94	0.35
5.79	6.00	5.78	4.44	1.34	4.89	3.40
0.00	0.00	0.05	0.00	0.00	0.00	0.00
0.29	0.43	0.51	0.43	0.50	0.39	0.43
10.14	10.81	12.02	10.93	9.36	11.62	10.28
2.75	3.33	1.50	1.83	0.28	1.63	1.60
0.00	0.00	0.02	0.01	0.08	0.00	0.00
14.97	14.39	13.92	15.23	17.70	14.28	15.79
12.37	11.85	11.68	12.12	12.31	11.72	12.09
0.87	1.19	1.30	0.94	0.37	1.06	0.70
0.63	0.65	0.67	0.44	0.11	0.50	0.28
97.39	97.71	97.20	97.47	98.15	96.00	96.62
7.13	7.02	7.15	7.34	7.89	7.26	7.52
0.88	0.98	0.85	0.66	0.11	0.74	0.48
0.00	0.00	0.00	0.00	0.00	0.00	0.00
0.00	0.00	0.00	0.00	0.00	0.00	0.00
8.00	8.00	8.00	8.00	8.00	8.00	8.00
0.08	0.12	0.12	0.06	0.02	0.11	0.04
0.12	0.06	0.16	0.10	0.11	0.12	0.11
0.00	0.00	0.01	0.00	0.00	0.00	0.00
0.30	0.37	0.17	0.20	0.03	0.18	0.18
0.00	0.00	0.00	0.00	0.01	0.00	0.00
0.01	0.00	0.02	0.00	0.01	0.00	0.00
1.24	1.31	1.48	1.33	1.10	1.44	1.25
3.26	3.14	3.05	3.30	3.72	3.16	3.43
5.00	5.00	5.00	5.00	5.00	5.00	5.00
0.03	0.05	0.05	0.05	0.05	0.05	0.05
0.00	0.01	0.00	0.00	0.00	0.00	0.00
1.93	1.86	1.84	1.89	1.86	1.86	1.89
0.04	0.08	0.11	0.06	0.09	0.09	0.07
2.00	2.00	2.00	2.00	2.00	2.00	2.00
0.21	0.26	0.26	0.21	0.01	0.22	0.13
0.12	0.12	0.13	0.08	0.02	0.10	0.05
0.33	0.39	0.39	0.29	0.03	0.31	0.18
15.33	15.39	15.39	15.29	15.03	15.31	15.19

	Sampole R2			Sample R1				
Amp 2	Amp 1a	Amp 1b	Amp 2	Amp 1a RR	Amp 1a core	Amp 1b	Amp 2	Amp 1a RR
BPB1-C1-10	R2.5-C1-7	R2.5-C1-4	R2.5-C3-12	R1-C3-79	R1-C2-43	R1-C1-1	R1-C1-17	B1-C2-47
52.54	50.24	49.77	54.67	46.38	46.09	48.65	52.81	48.74
0.13	0.61	0.53	0.00	1.21	1.30	0.45	0.04	1.12
2.16	4.52	4.61	0.87	6.43	6.50	5.39	1.60	5.45
0.00	0.01	0.00	0.01	0.03	0.03	0.02	0.07	0.08
0.50	0.36	0.42	0.66	0.49	0.43	0.39	0.58	0.42
10.00	8.12	9.16	6.39	12.10	11.60	11.23	9.49	11.11
1.73	4.15	3.37	3.07	3.64	4.07	3.42	2.94	1.83
0.00	0.00	0.00	0.00	0.00	0.00	0.00	0.00	0.00
16.14	16.44	15.84	19.24	13.29	13.60	14.41	16.33	14.96
12.31	12.33	12.27	11.80	11.93	12.12	12.13	12.86	12.28
0.48	0.90	1.01	0.47	1.47	1.55	1.23	0.31	1.34
0.11	0.37	0.40	0.05	0.67	0.68	0.56	0.04	0.53
96.12	98.05	97.37	97.25	97.64	97.97	97.87	97.07	97.86
7.67	7.22	7.23	7.76	6.88	6.82	7.12	7.65	7.11
0.33	0.77	0.77	0.15	1.12	1.13	0.88	0.27	0.89
0.00	0.01	0.00	0.00	0.00	0.05	0.00	0.00	0.00
0.00	0.00	0.00	0.10	0.00	0.00	0.00	0.07	0.00
8.00	8.00	8.00	8.00	8.00	8.00	8.00	8.00	8.00
0.02	0.05	0.06	0.00	0.14	0.09	0.05	0.00	0.12
0.04	0.00	0.02	0.00	0.00	0.00	0.05	0.00	0.05
0.00	0.00	0.00	0.00	0.00	0.00	0.00	0.01	0.01
0.19	0.45	0.37	0.23	0.41	0.45	0.38	0.25	0.20
0.00	0.00	0.00	0.00	0.00	0.00	0.00	0.00	0.00
0.03	0.00	0.01	0.00	0.01	0.02	0.00	0.07	0.01
1.22	0.97	1.11	0.70	1.50	1.43	1.37	1.15	1.36
3.51	3.52	3.43	4.07	2.94	3.00	3.14	3.53	3.25
5.00	5.00	5.00	5.00	5.00	5.00	5.00	5.00	5.00
0.04	0.04	0.04	0.08	0.05	0.04	0.05	0.00	0.04
0.00	0.00	0.00	0.06	0.00	0.00	0.00	0.00	0.00
1.92	1.90	1.91	1.79	1.90	1.92	1.90	2.00	1.92
0.04	0.05	0.05	0.07	0.06	0.04	0.05	0.00	0.04
2.00	2.00	2.00	2.00	2.00	2.00	2.00	2.00	2.00
0.10	0.20	0.24	0.07	0.37	0.40	0.30	0.09	0.34
0.02	0.07	0.07	0.01	0.13	0.13	0.11	0.01	0.10
0.12	0.26	0.31	0.07	0.49	0.53	0.40	0.09	0.43
15.12	15.26	15.31	15.07	15.50	15.53	15.40	15.09	15.43

Sample B1			Sample B3		
Amp 1a core	Amp 1b	Amp 2	Amp 1a	Amp 1b	Amp 2
B1-C1-32	B1-C1-1	B1-C2-38	B3-C1-8	B3-C1-3	B3-C3-77
47.51	47.57	53.60	47.46	48.58	53.28
1.07	1.07	0.17	1.22	0.85	0.15
6.05	6.02	1.79	6.13	5.58	1.43
0.01	0.00	0.02	0.00	0.03	0.00
0.46	0.38	0.59	0.52	0.45	0.41
11.86	11.44	8.12	10.95	10.53	9.87
3.21	3.54	3.61	4.69	4.66	2.41
0.00	0.00	0.00	0.00	0.00	0.00
13.65	14.15	17.94	14.11	14.41	16.51
11.93	12.06	11.50	12.05	12.10	12.77
1.24	1.41	0.55	1.33	1.00	0.28
0.60	0.64	0.14	0.64	0.54	0.12
97.59	98.28	98.03	99.09	98.73	97.24
7.01	6.97	7.62	6.90	7.05	7.69
0.99	1.03	0.30	1.05	0.95	0.24
0.00	0.00	0.02	0.05	0.00	0.02
0.00	0.00	0.06	0.00	0.00	0.05
8.00	8.00	8.00	8.00	8.00	8.00
0.12	0.12	0.00	0.09	0.09	0.00
0.06	0.01	0.00	0.00	0.00	0.00
0.00	0.00	0.00	0.00	0.00	0.00
0.36	0.39	0.33	0.51	0.51	0.22
0.00	0.00	0.00	0.00	0.00	0.00
0.00	0.00	0.00	0.01	0.00	0.04
1.46	1.40	0.87	1.33	1.28	1.19
3.00	3.09	3.80	3.06	3.12	3.55
5.00	5.00	5.00	5.00	5.00	5.00
0.05	0.05	0.07	0.06	0.06	0.01
0.00	0.00	0.10	0.00	0.00	0.00
1.89	1.89	1.75	1.88	1.88	1.98
0.06	0.06	0.08	0.07	0.06	0.01
2.00	2.00	2.00	2.00	2.00	2.00
0.29	0.34	0.08	0.31	0.22	0.07
0.11	0.12	0.03	0.12	0.10	0.02
0.41	0.46	0.10	0.43	0.32	0.09
15.41	15.46	15.10	15.43	15.32	15.09

	Sample 59A					
Sample	59A-C1-11	59A-C2-22	59A-C1-7	59A-C3-52	59A-C4-66	59A-C4-59
Generation	Pl pre-1	Pl 1a	Kfs	Pl 1b	Pl 2c in fracture	Pl 2b exolution
SiO2	56.52	56.85	64.60	56.63	64.83	66.41
TiO2	0.03	0.00	0.00	0.05	0.00	0.01
Al2O3	27.34	26.75	18.33	24.86	20.03	19.27
Cr2O3	0.00	0.00	0.06	0.00	0.05	0.02
FeO	0.19	0.15	0.13	0.27	0.04	0.09
MnO	0.01	0.02	0.00	0.00	0.00	0.02
MgO	0.03	0.00	0.00	0.00	0.00	0.00
CaO	9.49	8.88	0.00	8.80	2.63	1.58
Na2O	5.81	6.26	0.70	6.01	9.61	10.01
K2O	0.14	0.15	15.75	0.15	0.26	0.16
NiO	0.00	0.00	0.00	0.00	0.00	0.00
Sum	99.55	99.06	99.57	96.77	97.46	97.59
Ox number	8.00	8.00	8.00	8.00	8.00	8.00
Si	2.55	2.57	3.00	2.62	2.92	2.98
Ti	0.00	0.00	0.00	0.00	0.00	0.00
Al	1.45	1.43	1.00	1.36	1.06	1.02
Cr	0.00	0.00	0.00	0.00	0.00	0.00
Fe2	0.01	0.01	0.01	0.01	0.00	0.00
Mn	0.00	0.00	0.00	0.00	0.00	0.00
Mg	0.00	0.00	0.00	0.00	0.00	0.00
Ca	0.46	0.43	0.00	0.44	0.13	0.08
Na	0.51	0.55	0.06	0.54	0.84	0.87
K	0.01	0.01	0.93	0.01	0.01	0.01
Ni	0.00	0.00	0.00	0.00	0.00	0.00
cationSUM	4.98	4.99	5.00	4.97	4.97	4.95
XAn	47.05	43.56	0.00	44.33	12.94	7.94
XOr	0.81	0.86	93.67	0.88	1.50	0.98
XAb	52.13	55.57	6.33	54.79	85.56	91.07

Sample 67b						Sample 3
67b-C1-3	67b-C2-29	67b-C1-15	67b-C5-65	3130105-c2-4	3130105-c1-7	3130105-c2-41
Pl 1a	Kfs	Pl 1b	Pl 2 rim	Pl pre-1	Pl 1a RR	Pl 1a
57.91	64.42	60.88	68.41	62.19	67.47	61.53
0.02	0.05	0.01	0.00	0.00	0.02	0.00
24.83	18.23	23.17	18.96	23.41	21.19	23.89
0.00	0.12	0.00	0.03	0.01	0.02	0.06
0.16	0.12	0.34	0.07	0.15	0.07	0.27
0.03	0.00	0.00	0.04	0.01	0.00	0.01
0.00	0.00	0.00	0.00	0.00	0.00	0.02
8.33	0.01	5.84	0.50	5.11	1.63	5.63
7.01	1.51	8.12	11.44	8.71	11.08	8.35
0.13	14.62	0.19	0.12	0.18	0.12	0.22
0.00	0.00	0.00	0.00	0.03	0.03	0.02
98.43	99.08	98.55	99.57	99.80	101.63	100.00
8.00	8.00	8.00	8.00	8.00	8.00	8.00
2.64	2.99	2.75	3.00	2.76	2.92	2.74
0.00	0.00	0.00	0.00	0.00	0.00	0.00
1.33	1.00	1.23	0.98	1.23	1.08	1.25
0.00	0.00	0.00	0.00	0.00	0.00	0.00
0.01	0.00	0.01	0.00	0.01	0.00	0.01
0.00	0.00	0.00	0.00	0.00	0.00	0.00
0.00	0.00	0.00	0.00	0.00	0.00	0.00
0.41	0.00	0.28	0.02	0.24	0.08	0.27
0.62	0.14	0.71	0.97	0.75	0.93	0.72
0.01	0.87	0.01	0.01	0.01	0.01	0.01
0.00	0.00	0.00	0.00	0.00	0.00	0.00
5.01	5.01	5.00	4.99	5.00	5.01	5.00
39.34	0.05	28.13	2.34	24.23	7.47	26.81
0.75	86.39	1.09	0.68	1.02	0.66	1.25
59.91	13.56	70.78	96.99	74.75	91.88	71.95

3130105						
3130105-c1-2	3130105-c1-17	3130105-c2-48	BPA4-c3-74	BPA4-c5-95	Sample BPA4 BPA4-c1-10	BPA4-c1-6
Pl 1b	Kfs	Pl 2 exolution	Pl pre-1	Kfs1a	Pl 1a	Pl 1b
61.79	64.75	68.55	48.24	62.42	56.78	59.93
0.01	0.05	0.00	0.03	0.05	0.00	0.01
23.52	18.50	20.00	31.84	18.33	26.58	24.80
0.01	0.01	0.00	0.00	0.00	0.00	0.00
0.26	0.19	0.07	0.19	0.12	0.08	0.17
0.07	0.00	0.00	0.00	0.00	0.02	0.01
0.00	0.00	0.00	0.00	0.01	0.01	0.01
5.28	0.05	0.80	15.26	0.01	9.00	6.83
8.55	0.62	11.40	2.49	1.77	6.14	7.62
0.25	15.55	0.17	0.04	12.31	0.12	0.15
0.00	0.01	0.02	0.00	0.00	0.02	0.01
99.74	99.73	101.01	98.09	95.02	98.75	99.54
8.00	8.00	8.00	8.00	8.00	8.00	8.00
2.75	2.99	2.97	2.25	2.99	2.58	2.68
0.00	0.00	0.00	0.00	0.00	0.00	0.00
1.23	1.01	1.02	1.75	1.03	1.42	1.31
0.00	0.00	0.00	0.00	0.00	0.00	0.00
0.01	0.01	0.00	0.01	0.00	0.00	0.01
0.00	0.00	0.00	0.00	0.00	0.00	0.00
0.00	0.00	0.00	0.00	0.00	0.00	0.00
0.25	0.00	0.04	0.76	0.00	0.44	0.33
0.74	0.06	0.96	0.22	0.16	0.54	0.66
0.01	0.92	0.01	0.00	0.75	0.01	0.01
0.00	0.00	0.00	0.00	0.00	0.00	0.00
5.01	4.99	5.00	4.99	4.95	4.99	5.00
25.08	0.25	3.70	77.02	0.06	44.44	32.84
1.41	94.05	0.94	0.24	82.02	0.70	0.86
73.50	5.70	95.37	22.74	17.92	54.86	66.30

	Sample BPA10					
BPA4-c2-39	BPA10-c2-29	BPA10-c1-14	BPA10-c2-22	BPA10-c1-7	BPA10-c1-10	BPA10-c1-9
Pl 2c vein	Pl pre-1	Pl 1a	Pl 1a RR	Pl 1b	Kfs	Pl 2a Myrm
66.94	57.93	59.51	60.16	62.27	64.12	61.61
0.00	0.01	0.00	0.00	0.01	0.07	0.00
20.67	26.43	25.51	24.46	23.83	18.47	24.06
0.00	0.03	0.00	0.00	0.00	0.00	0.06
0.03	0.11	0.14	0.27	0.18	0.20	0.09
0.02	0.00	0.00	0.00	0.01	0.00	0.00
0.02	0.01	0.01	0.01	0.00	0.03	0.00
1.38	8.52	7.10	6.47	5.51	0.10	5.49
10.81	6.74	7.63	8.09	8.60	1.72	8.41
0.10	0.15	0.17	0.25	0.12	13.61	0.12
0.00	0.00	0.00	0.00	0.05	0.00	0.00
99.97	99.93	100.07	99.71	100.58	98.32	99.84
8.00	8.00	8.00	8.00	8.00	8.00	8.00
2.93	2.60	2.65	2.69	2.75	2.99	2.74
0.00	0.00	0.00	0.00	0.00	0.00	0.00
1.07	1.40	1.34	1.29	1.24	1.01	1.26
0.00	0.00	0.00	0.00	0.00	0.00	0.00
0.00	0.00	0.01	0.01	0.01	0.01	0.00
0.00	0.00	0.00	0.00	0.00	0.00	0.00
0.00	0.00	0.00	0.00	0.00	0.00	0.00
0.06	0.41	0.34	0.31	0.26	0.00	0.26
0.92	0.59	0.66	0.70	0.74	0.16	0.72
0.01	0.01	0.01	0.01	0.01	0.81	0.01
0.00	0.00	0.00	0.00	0.00	0.00	0.00
4.99	5.00	5.01	5.02	5.00	4.98	5.00
6.55	40.77	33.63	30.22	25.97	0.51	26.33
0.57	0.86	0.96	1.39	0.67	83.46	0.68
92.88	58.37	65.41	68.39	73.36	16.03	72.99

	Sample BPB1				Sample R2	
BPA10-c2-24	BPB1-C5-47	BPB1-C1-1	BPB1-C2-15	BPB1-C4-40	R2.5-C1-8	R2.5-C2-3
Pl 2b exolution	Pl 1a	Kfs	Pl 1b	Pl 2c interstitia	Pl 1b	Pl 2
67.24	58.69	62.48	61.14	67.43	58.59	64.93
0.04	0.05	0.00	0.00	0.00	0.02	0.00
20.40	24.42	17.94	22.59	19.14	24.31	21.28
0.00	0.04	0.00	0.01	0.02	0.01	0.02
0.04	0.24	0.00	0.22	0.04	0.25	0.10
0.05	0.01	0.01	0.00	0.02	0.00	0.02
0.00	0.02	0.00	0.03	0.01	0.02	0.02
1.29	7.74	0.02	5.37	0.33	6.14	1.95
11.14	6.76	0.31	8.16	11.18	8.19	11.16
0.22	0.32	16.01	0.21	0.13	0.31	0.11
0.00	0.00	0.00	0.00	0.00	0.00	0.00
100.42	98.29	96.77	97.72	98.29	97.84	99.59
8.00	8.00	8.00	8.00	8.00	8.00	8.00
2.94	2.67	2.99	2.78	3.00	2.68	2.88
0.00	0.00	0.00	0.00	0.00	0.00	0.00
1.05	1.31	1.01	1.21	1.00	1.31	1.11
0.00	0.00	0.00	0.00	0.00	0.00	0.00
0.00	0.01	0.00	0.01	0.00	0.01	0.00
0.00	0.00	0.00	0.00	0.00	0.00	0.00
0.00	0.00	0.00	0.00	0.00	0.00	0.00
0.06	0.38	0.00	0.26	0.02	0.30	0.09
0.94	0.60	0.03	0.72	0.96	0.73	0.96
0.01	0.02	0.98	0.01	0.01	0.02	0.01
0.00	0.00	0.00	0.00	0.00	0.00	0.00
5.01	4.98	5.01	4.99	4.99	5.04	5.05
5.94	38.03	0.08	26.33	1.61	28.79	8.75
1.21	1.86	97.03	1.25	0.72	1.71	0.61
92.85	60.11	2.89	72.42	97.67	69.50	90.63

	Sample R1			Sample B1		
R2.5-C4-21	R1-C1-27	R1-C3-80	R1-C2-46	B1-C1-16	B1-C1-13	B1-C2-48
Kfs	Pl 1a	Pl 1b	Kfs	Pl 1a	Pl 1b	Kfs
62.04	55.47	57.61	60.09	56.42	57.98	62.88
0.00	0.06	0.01	0.08	0.05	0.00	0.04
18.86	27.59	23.20	19.24	26.79	26.24	18.67
0.00	0.02	0.01	0.00	0.00	0.00	0.00
0.21	0.17	0.30	0.27	0.24	0.44	0.45
0.00	0.06	0.03	0.00	0.01	0.00	0.00
0.00	0.00	0.07	0.01	0.02	0.00	0.03
0.03	8.80	5.06	0.05	8.41	7.64	0.01
1.27	7.14	7.75	1.20	7.20	7.51	0.66
14.33	0.21	0.18	14.21	0.16	0.18	15.17
0.00	0.00	0.00	0.00	0.00	0.00	0.00
96.74	99.52	94.22	95.15	99.29	100.00	97.91
8.00	8.00	8.00	8.00	8.00	8.00	8.00
2.95	2.51	2.72	2.92	2.56	2.60	2.97
0.00	0.00	0.00	0.00	0.00	0.00	0.00
1.06	1.47	1.29	1.10	1.43	1.39	1.04
0.00	0.00	0.00	0.00	0.00	0.00	0.00
0.01	0.01	0.01	0.01	0.01	0.02	0.02
0.00	0.00	0.00	0.00	0.00	0.00	0.00
0.00	0.00	0.00	0.00	0.00	0.00	0.00
0.00	0.43	0.26	0.00	0.41	0.37	0.00
0.12	0.63	0.71	0.11	0.63	0.65	0.06
0.87	0.01	0.01	0.88	0.01	0.01	0.91
0.00	0.00	0.00	0.00	0.00	0.00	0.00
5.01	5.07	5.00	5.03	5.05	5.04	5.00
11.83	40.05	26.23	11.33	38.88	35.62	6.21
88.01	1.14	1.09	88.39	0.88	1.02	93.72
0.16	58.81	72.69	0.29	60.24	63.36	0.07

	Sample B3		
B1-C1-28	B3-C1-20	B3-C1-6	B3-C3-80
Pl 2	Pl 1a	Pl 1b	Kfs
64.54	56.34	62.66	62.83
0.03	0.00	0.00	0.06
21.67	27.05	22.59	18.76
0.02	0.01	0.03	0.05
0.04	0.14	0.13	0.15
0.00	0.03	0.00	0.00
0.02	0.01	0.00	0.00
2.63	9.35	4.44	0.00
10.53	6.57	9.24	1.55
0.18	0.16	0.27	14.19
0.00	0.00	0.00	0.00
99.65	99.66	99.35	97.60
8.00	8.00	8.00	8.00
2.86	2.54	2.80	2.96
0.00	0.00	0.00	0.00
1.13	1.44	1.19	1.04
0.00	0.00	0.00	0.00
0.00	0.01	0.00	0.01
0.00	0.00	0.00	0.00
0.00	0.00	0.00	0.00
0.12	0.45	0.21	0.00
0.90	0.58	0.80	0.14
0.01	0.01	0.02	0.85
0.00	0.00	0.00	0.00
5.03	5.03	5.02	5.01
12.01	43.64	20.67	14.23
0.95	0.87	1.48	85.74
87.03	55.49	77.85	0.02

Sample	59A-C3-47	BPA4-c1-3	BPA6 p88	BPA10-c1-1	R1-C2-49	B1-C2-61	B3-C2-47
an.	Cpx	Cpx	Cpx	Cpx	Cpx	Cpx	Cpx
K2O	0.03	0.01	0.01	0.03	0.02	0.01	0.00
CaO	23.72	23.18	22.77	22.56	22.12	24.61	23.49
TiO2	0.07	0.12	0.16	0.16	0.12	0.08	0.02
Cr2O3	0.07	0.07	0.00	0.03	0.00	0.00	0.00
MnO	0.45	0.39	0.69	0.63	0.49	0.65	0.71
FeOt	9.23	7.75	8.16	8.27	10.30	7.91	9.17
NiO	0.00	0.00		0.00			
Na2O	0.17	0.43	0.96	0.46	0.34	0.34	0.39
SiO2	52.85	53.41	53.28	52.64	51.25	53.79	52.91
Al2O3	0.23	0.98	0.51	0.98	0.71	0.35	0.49
MgO	12.79	13.63	13.95	13.64	13.61	13.62	13.60
TOTAL	99.61	99.97	100.48	99.41	98.96	101.36	100.78
formula: 4 cations, 6 oxygens							
Si	1.99	1.99	1.96	1.97	1.94	1.98	1.96
Al.IV	0.01	0.01	0.02	0.03	0.03	0.02	0.02
Al.VI	0.00	0.03	0.00	0.01	0.00	0.00	0.00
Ti	0.00	0.00	0.00	0.00	0.00	0.00	0.00
Cr	0.00	0.00	0.00	0.00	0.00	0.00	0.00
Fe3+	0.02	0.01	0.11	0.04	0.12	0.05	0.08
Fe2+	0.28	0.24	0.14	0.22	0.21	0.19	0.20
Mg	0.72	0.76	0.77	0.76	0.77	0.75	0.75
Ni	0.00	0.00	0.00	0.00	0.00	0.00	0.00
Mn	0.01	0.01	0.02	0.02	0.02	0.02	0.02
Ca	0.96	0.92	0.90	0.91	0.90	0.97	0.93
Na	0.01	0.03	0.07	0.03	0.03	0.02	0.03
K	0.00	0.00	0.00	0.00	0.00	0.00	0.00
∑cats	4.00	4.00	4.00	4.00	4.00	4.00	4.00
FeO	8.74	7.58	4.65	7.01	6.66	6.30	6.43
Fe2O3	0.54	0.19	3.90	1.41	4.05	1.79	3.04
newTotal	99.67	99.99	100.87	99.55	99.36	101.54	101.09

Sample	59A-C4-68	67b-C2-33	3130105-c3-5!	BPA4-c2-53	BPA6 p93	BPA10-c2-26
Mineral	Bt	Bt	Bt	Bt	Bt	Bt
SiO2	36.16	37.80	37.67	36.82	37.28	38.02
TiO2	4.46	3.42	3.84	3.76	3.04	3.30
Al2O3	12.23	12.92	13.39	13.60	12.80	13.69
Cr2O3	0.02	0.00	0.00	0.09	0.00	0.05
FeO	23.79	19.18	18.37	19.11	16.29	16.94
MnO	0.23	0.26	0.36	0.26	0.27	0.38
MgO	8.97	12.83	12.59	11.77	13.90	13.59
CaO	0.01	0.04	0.04	0.23	0.04	0.07
Na2O	0.10	0.10	0.15	0.12	0.71	0.16
K2O	9.51	9.74	9.53	9.28	9.64	9.56
NiO	0.00	0.00	0.03	0.00	0.00	0.07
Sum	95.47	96.29	95.97	95.04	93.97	95.83
Ox number	22.00	22.00	22.00	22.00	22.00	22.00
Si	5.67	5.72	5.70	5.65	5.73	5.71
Ti	0.53	0.39	0.44	0.43	0.35	0.37
Al	2.26	2.31	2.39	2.46	2.32	2.42
Cr	0.00	0.00	0.00	0.01	0.00	0.01
Fe2	3.12	2.43	2.32	2.45	2.09	2.13
Mn	0.03	0.03	0.05	0.03	0.04	0.05
Mg	2.10	2.90	2.84	2.69	3.18	3.04
Ca	0.00	0.01	0.01	0.04	0.01	0.01
Na	0.03	0.03	0.04	0.04	0.21	0.05
K	1.90	1.88	1.84	1.82	1.89	1.83
Ni	0.00	0.00	0.00	0.00	0.00	0.01
cationSUM	15.64	15.69	15.62	15.61	15.81	15.64

BPB1-C5-50
Bt
36.90
4.27
13.04
0.08
19.06
0.26
12.09
0.03
0.12
9.59
0.00
95.44
22.00
5.64
0.49
2.35
0.01
2.44
0.03
2.76
0.01
0.04
1.87
0.00
15.64

	Sample 67b	sample 3130105		Sample BPA4		Sample BPA6	
Sample	67b-C2-16	3130105-c2-30	3130105-c4-74	BPA4-c2-50	BPA4-c3-82	BPA6 p77	BPA6 p92
Generation	Ttn1a	Ttn2b	Ttn1a	Ttn2a	Ttn1a	Ttn2a	Ttn1a
SiO2	30.21	31.16	30.86	31.01	30.62	29.31	29.13
TiO2	36.86	31.62	35.97	35.62	36.74	35.89	36.10
Al2O3	1.14	4.96	1.38	1.39	1.09	1.55	1.24
Cr2O3	0.00	0.05	0.10	0.08	0.02	0.00	0.00
FeO	1.28	1.55	1.75	1.90	0.83	1.68	1.52
MnO	0.11	0.04	0.07	0.05	0.06	0.00	0.00
MgO	0.01	0.14	0.00	0.02	0.00	0.01	0.05
CaO	28.02	27.90	28.12	27.92	27.76	27.65	26.97
Na2O	0.00	0.00	0.04	0.00	0.00	0.36	0.27
K2O	0.00	0.08	0.03	0.00	0.01	0.00	0.00
NiO	0.00	0.04	0.05	0.03	0.05	0.00	0.00
Sum	97.63	97.54	98.37	98.02	97.18	96.45	95.28
Ox number	5.00	5.00	5.00	5.00	5.00	5.00	5.00
Si	1.01	1.04	1.03	1.04	1.03	1.00	1.00
Ti	0.93	0.79	0.90	0.89	0.93	0.92	0.93
Al	0.04	0.19	0.05	0.05	0.04	0.06	0.05
Cr	0.00	0.00	0.00	0.00	0.00	0.00	0.00
Fe2	0.04	0.04	0.05	0.05	0.02	0.05	0.04
Mn	0.00	0.00	0.00	0.00	0.00	0.00	0.00
Mg	0.00	0.01	0.00	0.00	0.00	0.00	0.00
Ca	1.01	0.99	1.00	1.00	1.00	1.01	0.99
Na	0.00	0.00	0.00	0.00	0.00	0.02	0.02
K	0.00	0.00	0.00	0.00	0.00	0.00	0.00
Ni	0.00	0.00	0.00	0.00	0.00	0.00	0.00
cationSUM	3.03	3.08	3.04	3.04	3.02	3.06	3.05

Sample BPA10	SampleBPB1	Sample R1	Sample B1		Sample B3		Sample R2
BPA10-c3-77	BPB1-C3-29	R1-C2-55	B1-C3-84	B1-C4-95	B3-C4-56	B3-C3-93	R2.5-C1-10
Ttn1a	Ttn1a	Ttn2a	Ttn1b	Ttn1a	Ttn1b	Ttn1a	Ttn1a
30.61	29.80	28.88	30.14	30.18	30.37	28.96	29.59
37.05	36.82	36.00	36.88	36.68	37.14	34.36	38.06
0.93	0.96	1.29	1.05	1.17	1.14	1.39	1.01
0.00	0.00	0.00	0.00	0.00	0.00	0.00	0.00
1.00	1.30	2.04	1.72	1.85	1.35	2.03	1.29
0.10	0.05	0.07	0.09	0.13	0.07	0.13	0.09
0.01	0.00	0.03	0.00	0.02	0.01	0.02	0.02
27.70	27.27	27.26	27.86	28.23	28.67	26.72	29.01
0.03	0.02	0.00	0.00	0.00	0.00	0.00	0.04
0.00	0.00	0.05	0.00	0.00	0.02	0.01	0.00
0.00	0.00	0.00	0.00	0.00	0.00	0.00	0.00
97.43	96.22	95.62	97.74	98.26	98.77	93.62	99.11
5.00	5.00	5.00	5.00	5.00	5.00	5.00	5.00
1.03	1.01	0.99	1.01	1.01	1.01	1.02	0.98
0.93	0.94	0.93	0.93	0.92	0.93	0.91	0.95
0.04	0.04	0.05	0.04	0.05	0.04	0.06	0.04
0.00	0.00	0.00	0.00	0.00	0.00	0.00	0.00
0.03	0.04	0.06	0.05	0.05	0.04	0.06	0.04
0.00	0.00	0.00	0.00	0.00	0.00	0.00	0.00
0.00	0.00	0.00	0.00	0.00	0.00	0.00	0.00
0.99	0.99	1.01	1.00	1.01	1.02	1.00	1.03
0.00	0.00	0.00	0.00	0.00	0.00	0.00	0.00
0.00	0.00	0.00	0.00	0.00	0.00	0.00	0.00
0.00	0.00	0.00	0.00	0.00	0.00	0.00	0.00
3.02	3.03	3.05	3.04	3.05	3.04	3.05	3.05

	Sample 59A		Sample 67b	Sample 3130105	Sample BPA4	Sample BPA10	Sample BPA6
Sample No	59A-C4-56	59A-C4-62	67b-C3-40	3130105p120	BPA4-c4-86	BPA10-c2-46	bpa6p55
SiO2	28.84	36.30	38.61	35.27	35.27	37.21	36.09
TiO2	1.85	0.12	0.00	0.03	0.03	0.49	0.00
Al2O3	11.36	19.23	31.44	15.19	15.19	19.57	24.45
Cr2O3	0.00	0.00	0.00	0.00	0.00	0.03	0.00
FeO	16.54	16.38	3.36	12.11	20.72	16.19	10.35
MgO	0.88	0.01	0.03	0.02	0.01	0.02	0.03
MnO	0.29	0.00	0.20	0.09	0.01	0.07	0.55
CaO	10.89	22.41	24.28	23.39	22.08	21.79	22.24
Na2O	0.04	0.00	0.00	0.25	0.04	0.04	0.46
K2O	0.01	0.02	0.03	0.02	0.01	0.00	0.03
Total wt%	70.69	94.46	97.94	97.85	93.36	95.41	94.20
Si	3.26	3.00	2.95	2.94	2.99	3.05	2.92
Ti	0.16	0.01	0.00	0.01	0.00	0.03	0.00
Al	1.51	1.87	2.83	2.24	1.52	1.89	2.33
Cr	0.00	0.00	0.00	0.00	0.00	0.00	0.00
Fe3+	0.91	1.11	0.22	0.79	1.47	0.96	0.70
Fe2+	0.66	0.02	0.00	0.00	0.00	0.15	0.00
Mg	0.15	0.00	0.00	0.00	0.00	0.00	0.00
Mn	0.03	0.00	0.01	0.01	0.00	0.01	0.04
Ca	1.32	1.99	1.99	1.96	2.01	1.91	1.93
Na	0.01	0.00	0.00	0.04	0.01	0.01	0.07
K	0.00	0.00	0.00	0.00	0.00	0.00	0.00
Total apfu	8.00	8.00	8.00	8.00	8.00	8.00	8.00
Si	3.26	3.00	2.95	2.94	2.99	3.05	2.92
Al(IV)	0.00	0.00	0.05	0.06	0.01	0.00	0.08
Total T-site	3.26	3.00	3.00	3.00	3.00	3.05	3.00
Ti	0.16	0.01	0.00	0.01	0.00	0.03	0.00
Al(VI)	1.51	1.87	2.78	2.19	1.51	1.89	2.25
Cr	0.00	0.00	0.00	0.00	0.00	0.00	0.00
V	0.00	0.00	0.00	0.00	0.00	0.00	0.00
Fe3+	0.91	1.11	0.22	0.79	1.47	0.96	0.70
Fe2+	0.28	0.01	0.00	0.00	0.00	0.12	0.00
Mg	0.15	0.00	0.00	0.00	0.00	0.00	0.00
Mn2+	0.00	0.00	0.00	0.01	0.00	0.00	0.04
Total M-site	3.00	3.00	3.00	3.00	2.99	3.00	3.00
Mn2+	0.03	0.00	0.01	0.00	0.00	0.01	0.00
Fe2+	0.38	0.01	0.00	0.00	0.00	0.03	0.00
Ca	1.32	1.99	1.99	1.96	2.01	1.91	1.93
Na	0.01	0.00	0.00	0.01	0.02	0.01	0.07
K	0.00	0.00	0.00	0.00	0.01	0.00	0.00
Total A-site	1.74	2.00	2.00	2.00	2.04	1.95	2.00

Formula according to Yavuz and Yıldırım (2018)

Sample BPB1 BPB1-C1-3	Sample R2 R2.5-C2-1
36.79	36.98
0.15	0.07
25.24	23.80
0.00	0.00
9.50	11.62
0.02	0.04
0.81	0.62
21.88	21.84
0.01	0.01
0.15	0.02
94.56	94.99
2.97	2.99
0.01	0.00
2.40	2.27
0.00	0.00
0.64	0.74
0.00	0.05
0.00	0.01
0.06	0.04
1.90	1.89
0.00	0.00
0.02	0.00
8.00	8.00
2.97	2.99
0.03	0.01
3.00	3.00
0.01	0.00
2.38	2.26
0.00	0.00
0.00	0.00
0.61	0.73
0.00	0.00
0.00	0.01
0.00	0.00
3.00	3.00
0.06	0.04
0.00	0.05
1.90	1.89
0.00	0.00
0.02	0.00
1.97	1.99

	Sample 3130105				Sample BPA4	
Site	after Pl1a	after Bt	after Bt	after Bt	after Bt	after Bt
Sample	3130105-c2-19	3130105-c2-29	3130105-c3-57	3130105-c4-72	BPA4-c1-17	BPA4-c3-69
SiO2	27.10	27.90	28.85	27.74	30.69	28.04
TiO2	0.01	0.10	0.11	0.15	0.04	0.05
Al2O3	20.83	20.03	19.67	19.36	16.24	18.90
FeO	21.88	22.91	20.66	22.73	21.83	20.93
MnO	0.43	0.42	0.37	0.39	0.19	0.35
MgO	17.20	16.89	16.74	16.87	17.94	18.33
CaO	0.07	0.13	0.19	0.10	0.40	0.11
Na2O	0.05	0.03	0.01	0.05	0.01	0.02
K2O	0.03	0.07	0.16	0.05	0.22	0.07
Cr2O3	0.00	0.00	0.00	0.00	0.00	0.00
Sum	87.60	88.48	86.76	87.44	87.56	86.80
Si	2.80	2.87	2.98	2.89	3.16	2.91
Ti	0.00	0.01	0.01	0.01	0.00	0.00
Al	2.54	2.43	2.40	2.37	1.97	2.31
Fe2+	1.89	1.97	1.78	1.98	1.88	1.82
Mn	0.04	0.04	0.03	0.03	0.02	0.03
Mg	2.65	2.59	2.58	2.62	2.76	2.84
Ca	0.01	0.01	0.02	0.01	0.04	0.01
Na	0.01	0.01	0.00	0.01	0.00	0.00
K	0.00	0.01	0.02	0.01	0.03	0.01
Cr	0.00	0.00	0.00	0.00	0.00	0.00

Formula according to Bourdelle et al. (2013)

	Sample BPA10		Sample BPB1	
after Bt	after Bt	interstitial c/oTtn	after Amp1	interstitial c/o kfs
BPA10-c1-3	BPA10-c2-32	BPA10-c3-80	BPB1-C5-75	B1-C1-21
28.87	28.41	27.47	28.50	24.92
0.11	0.00	0.19	0.01	0.05
17.75	18.44	19.13	17.58	21.87
22.46	24.16	24.89	22.49	29.86
0.36	0.53	0.65	0.39	1.26
18.36	17.24	16.19	18.06	10.50
0.12	0.03	0.15	0.05	0.05
0.08	0.01	0.08	0.02	0.00
0.08	0.02	0.04	0.00	0.02
0.00	0.00	0.00	0.00	0.03
88.19	88.84	88.79	87.10	88.55
2.97	2.93	2.85	2.97	2.68
0.01	0.00	0.01	0.00	0.00
2.15	2.24	2.34	2.16	2.77
1.93	2.08	2.16	1.96	2.68
0.03	0.05	0.06	0.03	0.11
2.82	2.65	2.51	2.81	1.68
0.01	0.00	0.02	0.01	0.01
0.02	0.00	0.02	0.00	0.00
0.01	0.00	0.01	0.00	0.00
0.00	0.00	0.00	0.00	0.00

sample	temperature (°C)			pressure (kbar)				
	Putirka 2016 Si, Ti, Fe, Na content in Amp	**Holland and Blundy** Na Si-Ca Al exchange of Pl and Amp	**Benisek *et al.* 2004** two-feldspar ternary mixing	**Molina *et al*. 2015** Al/Si partitioning in Pl and Amp	**Mutch *et al*. 2016** Al in Amp	**Anderson and Smith** Al in Amp, T-dependent	**Schimidt 1992** Al in Amp	**Erdmann *et al*. 2019** Al_2O_3 in Ttn
3130105								
Amp_{1a}/Ttn_{1a}	788±10 (n=6)			1.76±0.13 (n=2)	2.39±0.18 (n=6)		2.79±0.31 (n=6)	1.99 (n=1)
Amp_{1b}	775±18 (n=12)	718±29 (n=13)		1.31±0.89 (n=7)	2.21±0.28 (n=12)	2.11±0.60 (n=12)	2.47±0.53 (n=12)	
Amp_2	669±15 (n=3)				0.63±0.07 (n=3)			
Perthite			453±99					
59A								
Amp_{1a}	730±27 (n=10)				1.59±0.37 (n=10)		1.53±0.52 (n=8)	
Amp_{1b}	715±24 (n=16)	729±45 (n=10)			1.58±0.34 (n=16)	1.05±0.35 (n=7)	1.37±0.66 (n=13)	
Perthite			440±74					
BPA4								
Amp_{1a}/Ttn_{1a}	762±11 (n=10)			078±0.73 (n=3)	1.92±0.20 (n=10)		1.92±0.39 (n=10)	1.70 (n=1)
Amp_{1b}/Fsp	758±17 (n=13)	692±31 (n=6)	745±33 (n=2)	1.34±0.91 (n=3)	1.91±0.27 (n=13)	1.78±0.42 (n=6)	1.91±0.55 (n=10)	
Amp_2	673±22 (n=5)				0.79±0.22 (n=5)			
BPA6								
Amp_{1a}/Ttn_{1a}	762±20 (n=5)				1.75±0.46 (n=5)		1.97±0.45 (n=4)	1.72±0.18 (n=2)
BPA10								
Amp_{1a}/Ttn_{1a}	763±22 (n=10)				1.74±0.39 (n=10)		1.71±0.68 (n=9)	1.65±0.20 (n=5)
Amp_{1b}/Fsp	758±22 (n=23)	701±27 (n=10)	659±11 (n=3)		1.66±0.38 (n=23)	1.52±0.67 (n=11)	1.33±0.85 (n=23)	
Amp_2	691±36 (n=14)				0.83±0.18 (n=14)			
Myrmekite			615±2 (n=2)					
Perthite			508 (n=1)					
B1								
Amp_{1a}/Ttn_{1a}	772±18 (n=14)				1.77±0.32 (n=14)		1.59±0.68 (n=14)	1.77±0.19 (n=4)
Amp_{1b}/Ttn_{1b}	756±25 (n=25)	747±52 (n=9)			1.60±0.33 (n=25)	1.21±0.59 (n=9)	1.27±0.71 (n=25)	1.66 (n=1)
Amp_2	685±27 (n=3)				0.62±0.07 (n=3)			
B3								
Amp_{1a}/Ttn_{1a}	769±29 (n=10)				1.88±0.40 (n=10)		1.80±0.82 (n=10)	1.90±0.15 (n=2)
Amp_{1b}/Ttn_{1b}	741±32 (n=28)	725±55 (n=12)			1.52±0.39 (n=28)	1.10±0.48 (n=13)	1.32±0.69 (n=22)	1.75 (n=1)
67b								
Amp_{1a}/Ttn_{1a}	731±31 (n=4)				1.27±0.37 (n=4)		1.19±0.35 (n=3)	1.74±0.02 (n=3)
Amp_{1b}/Fsp	729±13 (n=22)	671±22 (n=11)	668±39 (n=2)		1.29±0.20 (n=22)	0.57±0.38 (n=9)	0.63±0.36 (n=19)	

Amp_2	694±14 (n=4)		0.81±0.18 (n=4)			
BPB1						
Amp_{1a}/Ttn_{1a}	746±21 (n=5)		1.46±0.25 (n=5)		1.16±0.41 (n=5)	1.56 (n=1)
Amp_{1b}/Fsp	735±18 (n=17)	685±26 (n=12)	1.34±0.27 (n=17)	0.79±0.47 (n=9)	0.83±0.48 (n=13)	
Amp_2	697±9 (n=4)		0.82±0.06 (n=4)			
R1						
Amp_{1a}	795±8 (n=3)		2.19±0.09 (n=3)		2.46±0.16 (n=3)	
Amp_{1b}/Fsp	760±33 (n=25)	740±29 (n=9)	1.58±0.52 (n=25)	1.61±0.70 (n=9)	1.71±0.76 (n=18)	
R2						
Amp_{1a}/Ttn_{1a}	732±25 (n=3)		1.06±0.25 (n=3)		0.65 (n=1)	1.61 (n=1)
Amp_{1b}	731±27 (n=7)	701±50 (n=3)	1.00±0.33 (n=7)	< 0.84 (n=1)	0.68±0.11 (n=2)	

n = number of estimates

Amp = amphibole, Pl = plagioclase, Chl = chlorite, Ttn = titanite. Amp_2 pressures and temperatures were estimated only by using Mutch et al. (2016) and Putirka (2016) calibrations as those are suitable also for low pressure and temperature.

Pressure (kbar) estimated for contact metamorphism in country rocks

Sample	Hoish 1990	Wu *et al.* 2004	Wu 2019	Vilzeuf 1983	AvPT
250495	3.27±0.54 (n=15)	2.91±0.45 (n=14)	4.25±0.49 (n=14)		
31c2385				2.25±0.43 (n=5)	
BPI2	2.01±1.02 (n=10)	1.44±0.34 (n=10)	2.53±0.59 (n=11)		2.95±1.18 (n= 10)
BSA8				2.24±0.23 (n=6)	
BSL16b				2.13±0.43 (n=8)	2.20±2.08 (n=7)
BSB4				2.12±0.47 (n=5)	

Composition for garnet, biotite, plagioclase, quartz barometer

	Fe (Bt)	Mg (Bt)	Al^{VI} (Bt)	Ti (Bt)	Ca (Pl)
250495	3.04±0.14	1.87±0.14	0.62±0.06	0.26±0.07	0.54±0.09
BPI2	3.46±0.92	2.22±1.03	0.89±0.29	0.18±0.12	0.44±0.03
	Na (Pl)	Fe (Gt)	Mg (Gt)	Ca (Gt)	Mn (Gt)
250495	0.47±0.10	2.29±0.02	0.24±0.02	0.17±.002	0.33±0.03
BPI2	0.55±0.03	2.26±0.05	0.28±0.07	0.10±0.01	0.33±0.12

Composition for spinel, cordierite, quartz barometer

	X_{Mg} (Crd)	Al (Sp)	X_{Mg} (Sp)
31c2385	0.45±0.01	1.96±0.05	0.07±0.00
BSA8	0.43±0.03	1.95±0.01	0.06±0.01
BSL16b	0.57±0.03	1.96±0.01	0.11±0.02
BSB4	0.57±0.01	1.92±0.04	0.12±0.01

End-member activity used for AvPT calculation

	phl	ann	east	crd	fcrd
BPI2	0.02±0.00	0.08±0.02	0.03±0.01	0.31±0.03	0.21±0.03
	an	alm	q	H_2O	
	0.60±0.09	0.44±0.03	1	1	
	phl	ann	east	en	fs
BSL16b	0.06±0.01	0.06±0.00	0.03±0.01	0.17±0.00	0.31±0.01
	mgts	crd	fcrd	san	sp
	0.01±0.00	0.36±0.01	0.19±0.00	0.85±0.01	0.12±0.01
	herc	mt	ab	q	H_2O
	0.88±0.01	0.03±0.00	0.75±0.10	1	1

n = number of estimates

End-member activities are calculated with AX program. Cations are calculated on the following number of oxygen atoms: biotite (Bt) 22, plagioclase (Pl) 8, garnet (Gt) 12, cordierite (Crd) 18, spinel (Sp) 4. Abbreviations for end-members are from THERMOCALC list. AvPT = average PT calculation.